WT-1671

OPERATION ARGUS

CALIBRATION OF EXPLORER IV PROTOTYPE

Issuance Date: October 21, 1963

DEFENSE ATOMIC SUPPORT AGENCY
WASHINGTON, D.C.

Inquiries relative to this report may be made to

Chief, Defense Atomic Support Agency
Washington 25, D. C.

DO NOT RETURN THIS DOCUMENT

WT-1671

THE ARGUS EXPERIMENT

CALIBRATION OF EXPLORER IV PROTOTYPE

E.O. Baicy, Project Officer
Juergen Bock
T.R. Jeter

Ballistic Research Laboratories
Aberdeen Proving Ground, Maryland

ABSTRACT

Detailed calibration curves were determined for a prototype Explorer IV radiation-measuring satellite in accordance with a prior mathematical analysis. This analysis had demonstrated the necessity for calibration of the complete package in a well-prescribed manner if the maximum amount of information was to be obtained from the transmitted data. Previous data analysis had been limited to consideration of average count rates because of limited information about the angular response of the detectors.

Since it was of primary interest to obtain mirror point distributions of the trapped electrons in the earth's magnetic field, emphasis was placed on the determination of the directional characteristics of the detectors. The package was calibrated with gamma rays, X-rays, and electrons over both azimuthal and inclination angles.

CONTENTS

FIGURES

CHAPTER 1

INTRODUCTION

Data taken by the Explorer IV-ϵ radiation-measuring satellite from 26 July 1958 until 3 September 1958 is still the most comprehensive and consistent body of data available on the trapping of natural radiation in the earth's magnetic field and the only information available on the trapping of artificially injected radiation—the Argus shell.

1.1 PURPOSE OF CALIBRATION

Although much information has been published on the results of the Explorer IV-ϵ measurements, this information has been based on the average count rates of the detectors with little directional sensitivity, i.e., the two Geiger-Muller (GM) counters. This data was adequate to determine the existence, location, and average flux in the Argus shell; however, much more important information such as mirror point distributions, loss mechanisms, and injection mechanism could be extracted from the count rate data if a systematic data reduction were made for all the detectors simultaneously including those with directional dependence. For this purpose, more detailed calibration data was needed for the package, particularly the angular response characteristics of the detectors, together with detailed information on the orientation of the package with the earth's magnetic field. Dr. Charles Lundquist's group at Marshall Flight Propulsion Laboratories obtained some orientation data from a few good records taken at Huntsville, using the signal strength pattern from the satellite transmitter (References 1 and 2). Orientation data could also be obtained from the count rate patterns of the directional detectors, once the angular response characteristics of these detectors were determined. Various procedures that might be used for a consistent analysis of all the data to extract the maximum information were examined by the Nuclear Physics Branch of the Ballistic Research Laboratories (BRL) under ABMA Contract ID 9064-00-60. This work defined the requirements for calibration of the complete satellite package as a unit and the additional requirements for orientation information. Following the recommendation of the Third Argus Working Group to obtain more information on the package, the Defense Atomic Support Agency (DASA) accepted a proposal by the Nuclear Physics Branch of BRL to perform a more detailed calibration of an Explorer IV-ϵ prototype that was in the possession of Professor James A. Van Allen and coworkers at the State University of Iowa.

1.2 DUPLICATION OF FLIGHT PACKAGE BY PROTOTYPE

Because the flight package and prototype had been originally calibrated by Van Allen and his associates, it was decided to put the prototype through the identical calibration used on the flight package prior to bringing it to BRL for a more detailed calibration.

The prototype was of identical construction to that of the flight package. It had four detectors located as shown in Figure 1.1 with characteristics as shown in Figure 1.2, with the exception of Detector A which had additional foils over the scintillation crystal to raise the threshold energy. The extra foils were removed from Detector A during the recalibration. A small Tl^{204} source was placed within a few thousandths of an inch of the foils covering the plastic scintillator on Detector A, and the discriminator was adjusted to count only 16 percent of the total count from the source by adjusting the gain of the linear amplifier preceding the discriminator. The point was graphically determined as shown in Figure 1.3.

The dc detector, Detector B (Figure 1.2), was calibrated by connecting an electrometer directly to the photomultiplier output and measuring the current for a given source strength. The output was within 5 percent of that of the flight package. The GM tubes were matched pairs of Anton 302 tubes, the same as used in the flight package. These were checked for proper operating conditions, using a Co^{60} source.

This preliminary check to insure that the prototype matched the flight package was performed by BRL personnel under the supervision of Van Allen's associates, prior to bringing the prototype to BRL for a more extensive calibration.

1.3 OPTIMUM PROCEDURE FOR CALIBRATION

Previous theoretical analysis (Reference 3) had delineated the optimum method for calibration of a radiation-measuring satellite. This analysis indicated that the entire satellite package should be irradiated with a homogeneous flux of parallel radiation of well-defined energies under various angular orientations (inclination and azimuth). It could be shown that it is not desirable to reproduce the cylindrical isotropy of the actual radiation field. Practical considerations forced only one compromise on the optimum, which was serious only in the sense that it required the taking of considerably more data than would have otherwise been required. Because it was practically impossible to produce parallel beams of radiation of sufficiently large dimensions to cover the entire package simultaneously, advantage was taken of the linearity of the Boltzmann transport equation (Reference 3) to justify the use of a relatively thin but wide beam of parallel radiation, together with a scanning motion to simulate a parallel homogeneous radiation field. This differential method complicated the data taking by introducing another parameter into the orientation device; however, this method is readily adjusted to the experimental conditions.

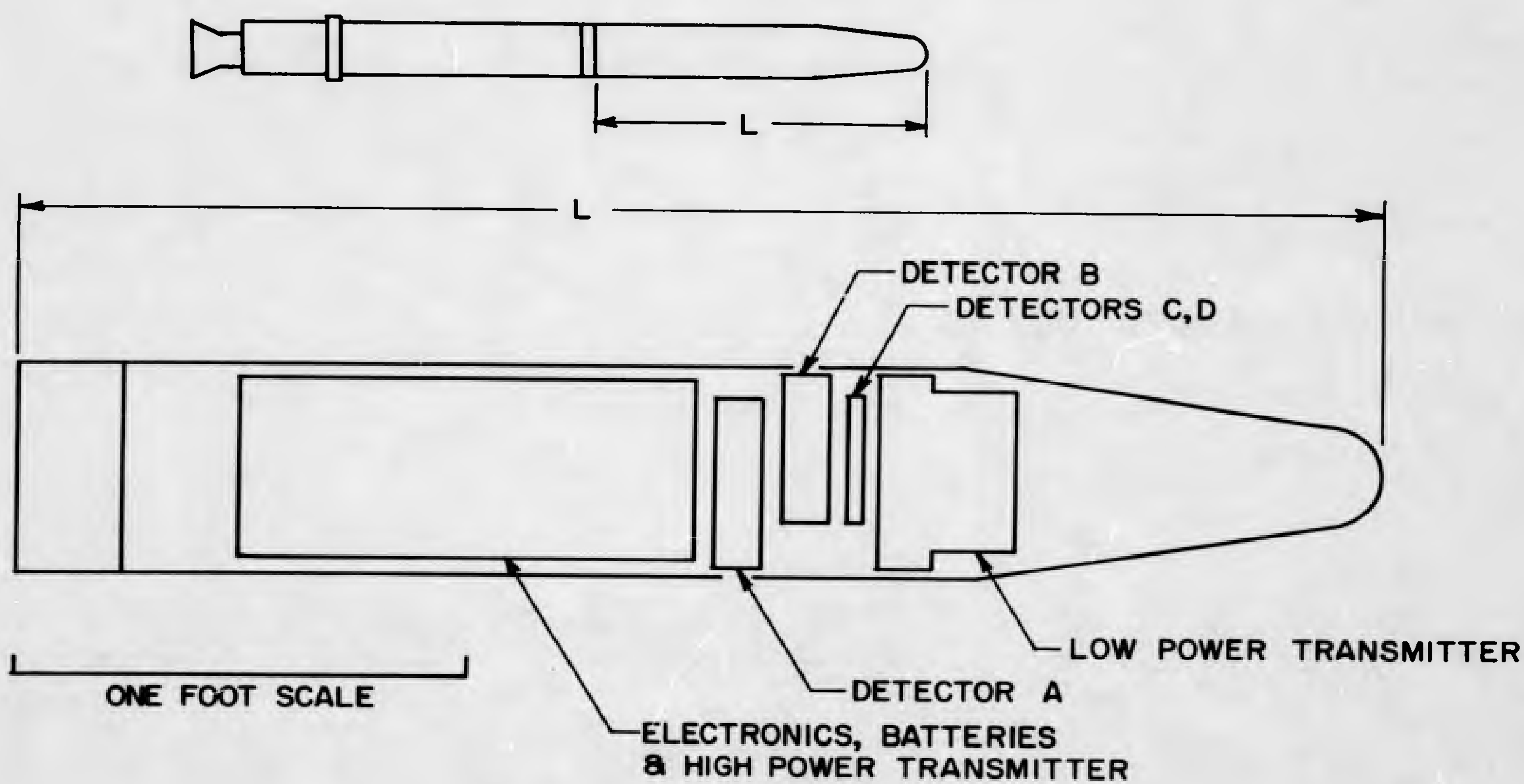

Figure 1.1 Payload configuration.

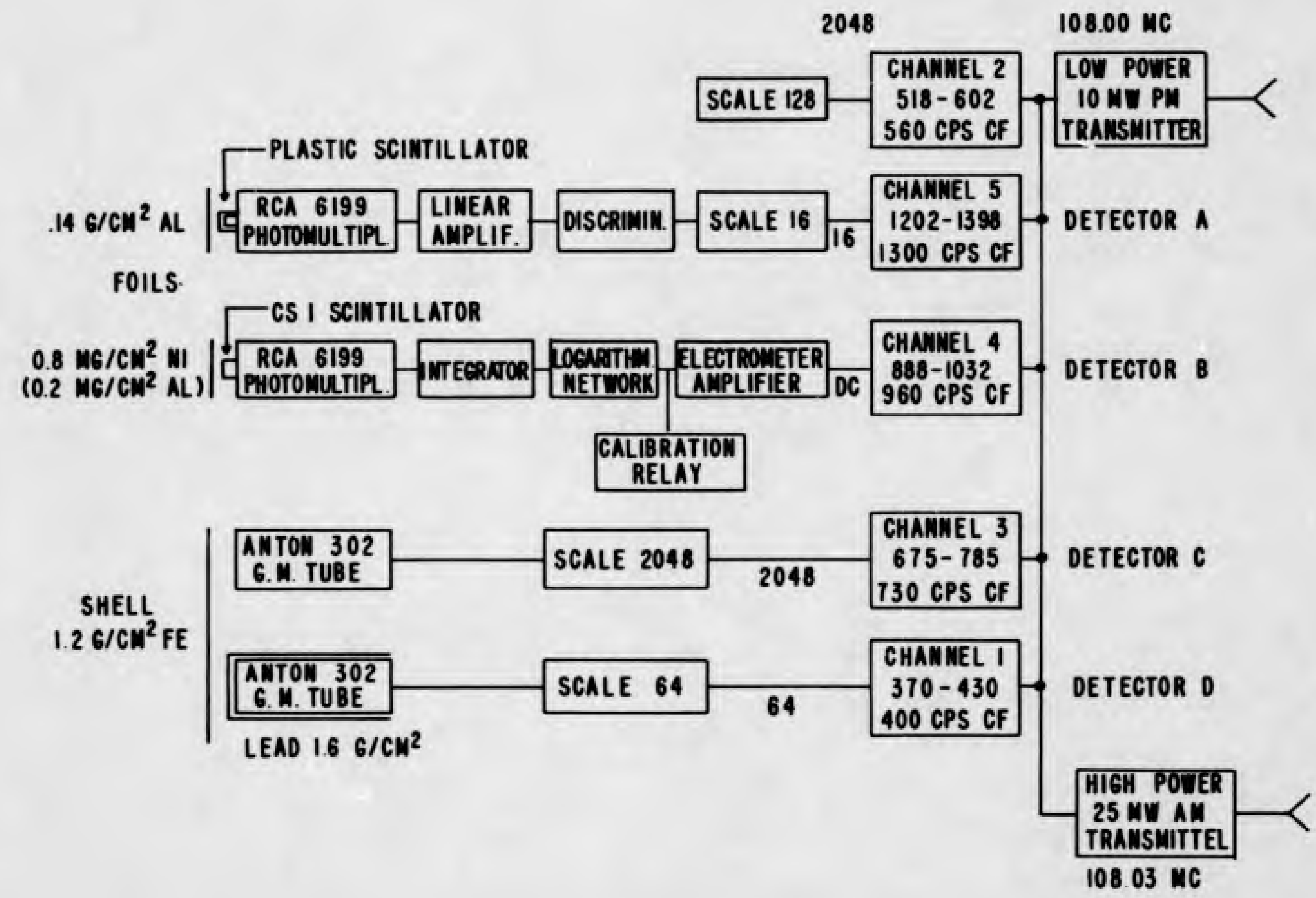

Figure 1.2 Block diagram of payload.

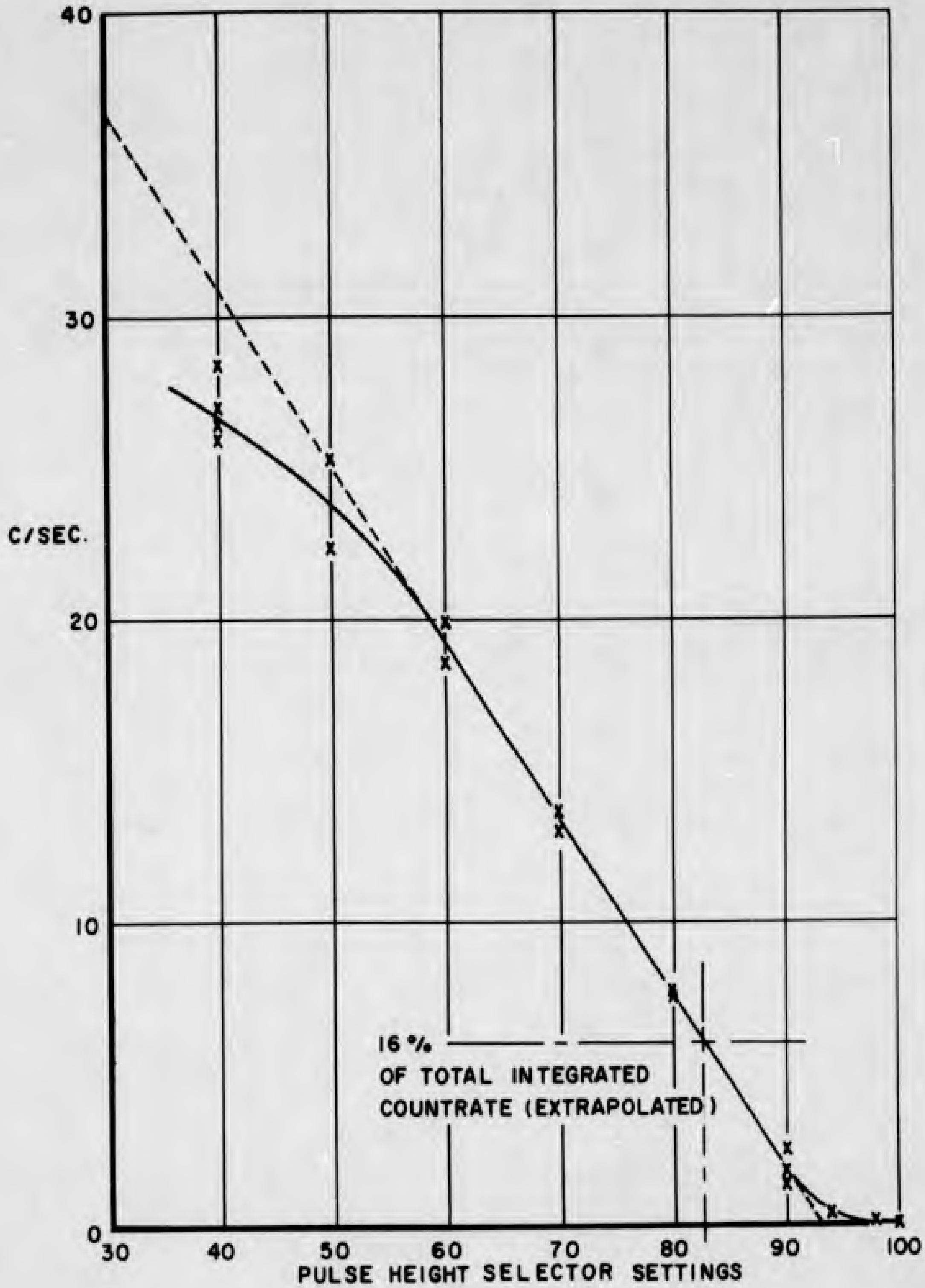

Figure 1.3 Integrated Tl^{204} spectrum for Discriminator A adjustment.

CHAPTER 2

EXPERIMENTAL PROCEDURES AND EQUIPMENT

Because proper calibration required a predetermined programing of the satellite orientation and motion, it was desirable to automate the entire process to complete the project in a reasonable time. Remote-controlled programing and data recording were especially necessary for use in the high-altitude facility during the beta calibration.

2.1 ORIENTATION DEVICE

For all calibrations, the orientation device shown schematically in Figure 2.1 and pictorally in Figure 2.2 was used. The three motions, scan (up and down), inclination θ ($-90°$ to $+90°$), and spin ($0°$ to $360°$ clockwise) were controlled by selsyn motors. All positional data was recorded simultaneously with the count rate data and a time reference in a digital form. All power and control lines terminated at a centralized panel where the motion could be programed and controlled remotely.

2.2 DATA RECORDING

The five channels of the Explorer package were tapped at their scaler outputs, and an external battery pack was used to supply the required power. The channel count rate data was fed into separate driving amplifiers of a six-track recorder. Time markers and position information were fed to the sixth channel. This served as an additional check on the programed motion.

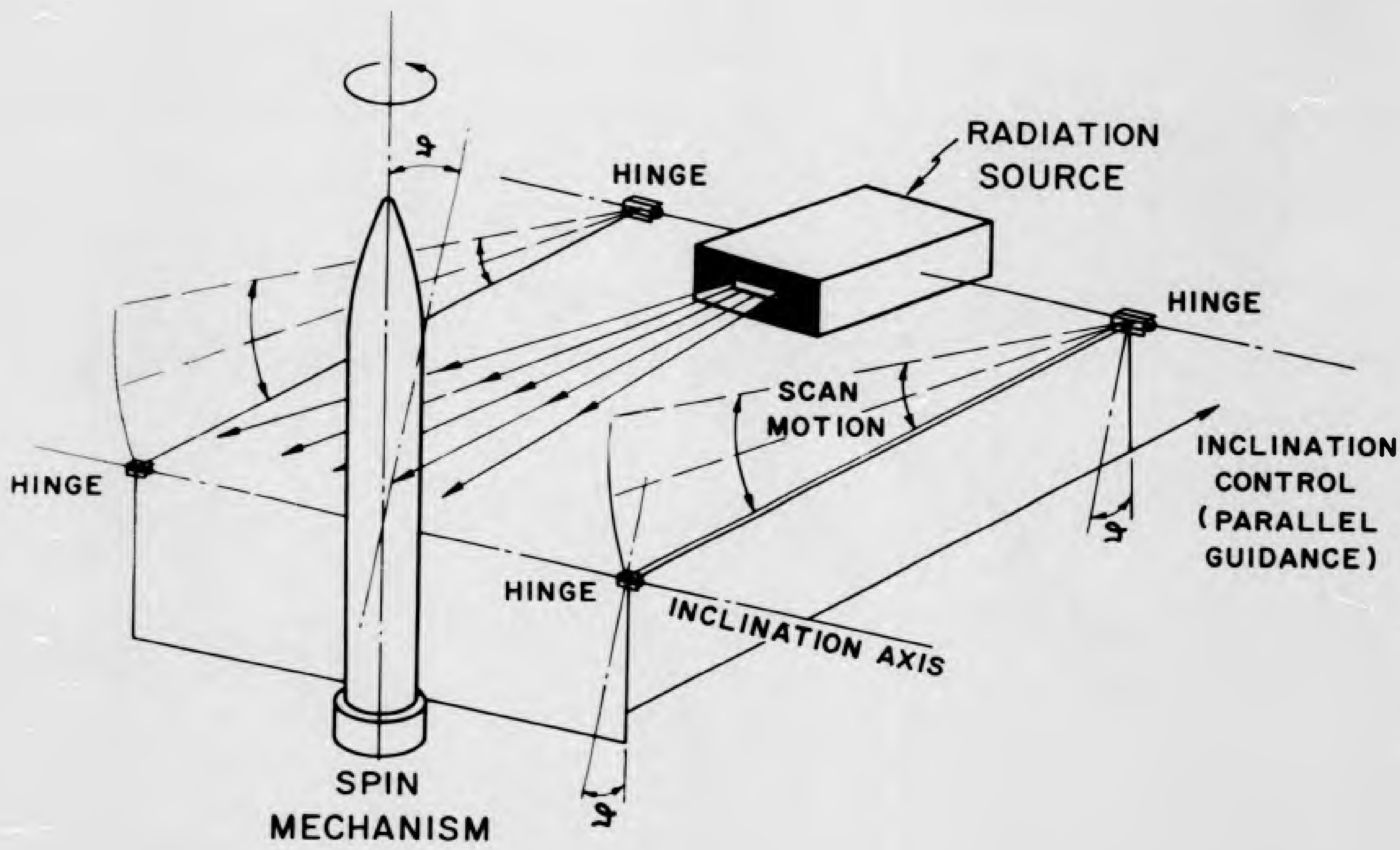

Figure 2.1 Calibration setup geometry.

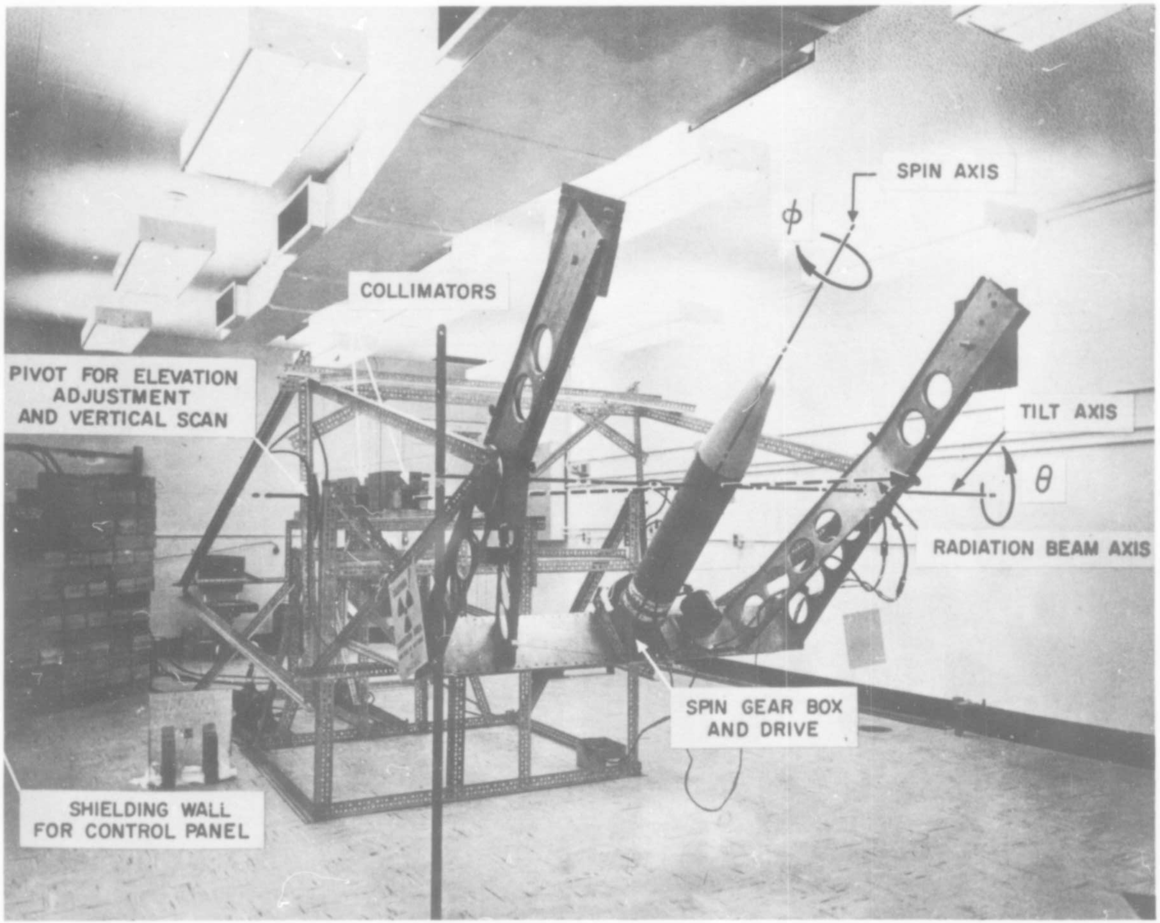

Figure 2.2 Photograph of calibration setup. (BRL photo)

CHAPTER 3

ELECTRONIC CHARACTERISTIC OF DETECTOR SYSTEMS

3.1 DISCRIMINATOR THRESHOLD

Detector A, the plastic scintillator with photomultiplier, has a pulse height discriminator in the circuit (Figure 1.2). This discriminator sets an energy threshold below which the pulses will not be counted. It was desirable to determine not only the effective value of this threshold but also the sharpness of the threshold curve. For this purpose, a precision mercury pulse generator was used to inject pulses of variable height into the circuit. The zero, 50 percent, and 100 percent output points of the discriminator were measured with respect to the input pulse amplitude. The threshold thus determined was 17.4 mv for zero output, 17.6 mv for 50 percent out put, and 17.9 mv for 100 percent output. Thus, the step width from 0 to 100 percent output was only 0.5 mv (Figure 3.1). Assuming that 17.6 mv correspond to 700-kev electron energy, a 0.5-mv discriminator width corresponds to 20 kev. This is the electronic discriminator step width of the linear amplifier discriminator combination, and it means that there must be a sharp cutoff at this energy. The method used to determine the absolute value of this cutoff in terms of beta energy is described under beta calibrations. As seen from Figure 1.2, there were no discriminators in the geiger tube circuits as is customary.

3.2 DEAD TIME

The dead times for the circuits were measured electronically by means of a square-wave generator and a pulse-forming network to provide pulses of the same rise and decay time as those measured from the photomultiplier of Detector A. In Detector A, the pulses were injected into the input of the linear amplifier (Figure 1.2). The output of the first scaler (scale of 16) was monitored as the frequency of the square-wave generator was increased until the count rate became inconsistent with the input pulse rate. Under this condition, the time interval between input pulses was taken as the dead time. This dead time was 112 μsec; this is characteristic of the scaler only, because the linear amplifier, discriminator, and the driver-limiter have a combined dead time of only 20 μsec. The dead time of the geiger tubes was not appreciably affected by the associated electronics as was verified by the two-source method for measuring dead time. The output of the geiger tubes and associated circuitry began to saturate at approximately 2000 counts/sec for photonic radiation as shown in Figure 3.2.

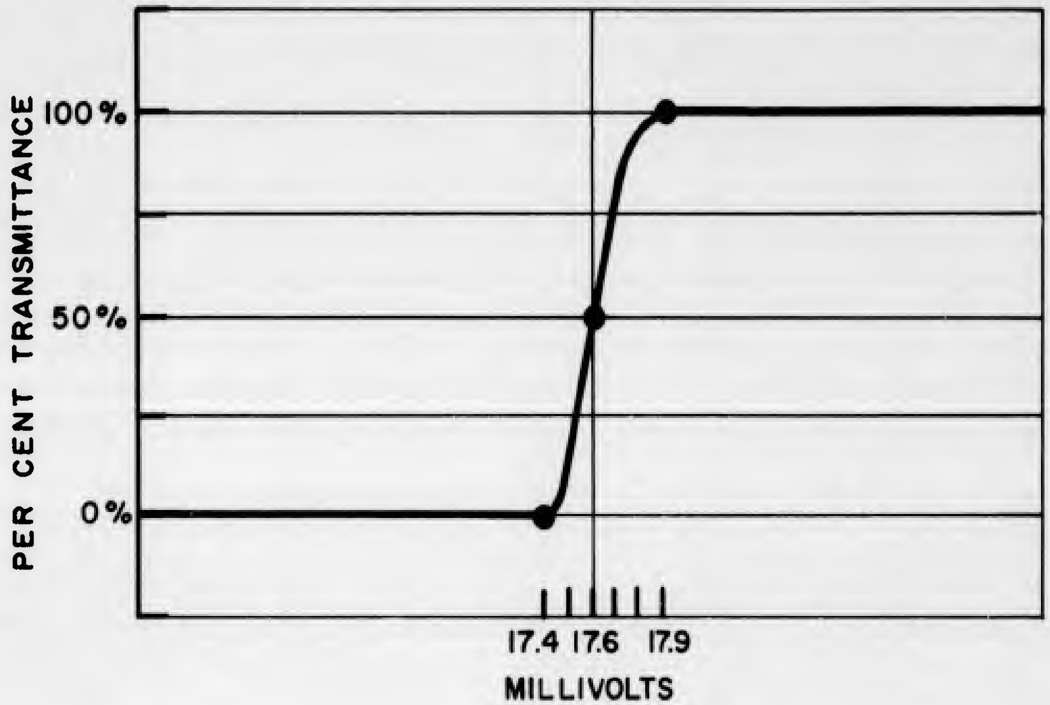

Figure 3.1 Discriminator threshold function as determined electronically.

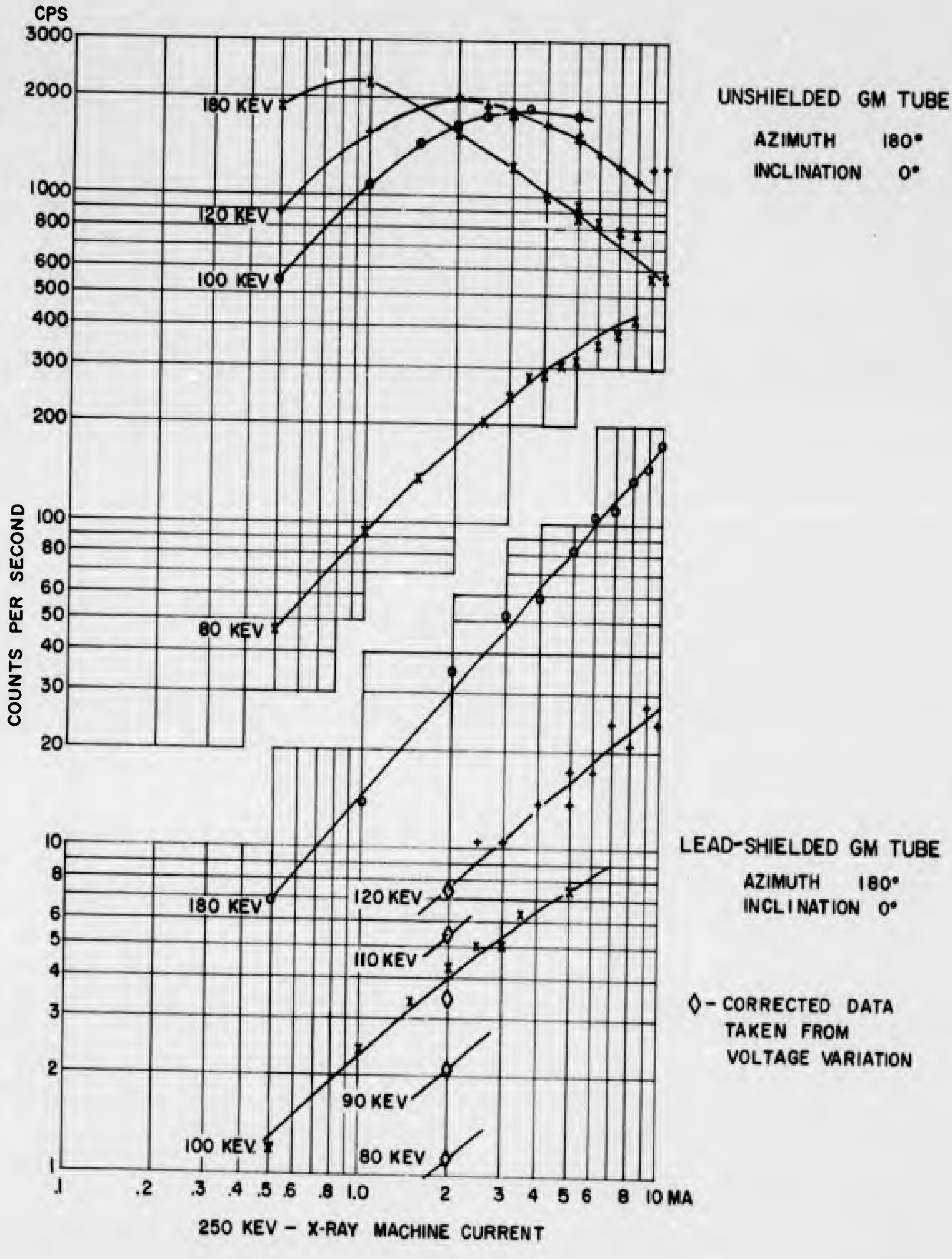

Figure 3.2 GM tube response curves.

CHAPTER 4

GAMMA RAY CALIBRATIONS

The satellite package was mounted on the orientation device as shown in Figure 2.2. The spin axis was taken as the polar axis, and the inclination angle was measured from the vertical. Thus, for inclination of 0°, the longitudinal axis of the package was vertical, and the radiation plane was perpendicular to the satellite axis. Zero degrees azimuth corresponded to the position where the opening for the integrating Detector B was facing the radiation source. Thus, at an azimuthal angle of 180°, the plastic scintillation detector was facing the radiation source.

4.1 SOURCE CHARACTERISTICS

Two sources were used, Cs^{137} and Co^{60}. The former has an energy peak at 0.66 Mev; the latter has two energy peaks, one at 1.17 and one at 1.33 Mev. The sources were located at the end of the orientation frame 4.435 meters from the satellite package in a lead container.

4.2 GEOMETRY OF INCIDENT RADIATION FIELD

The sources were collimated by a lead brick shield. The collimator array was first adjusted using an incandescent lamp substituted for the radioactive source. After this initial adjustment, the radiation field was measured and found to be as anticipated, i.e., a 1-ft^2 beam at the package with less than 2° divergence. Radiation scattering in air and in the collimators was found to be negligible.

4.3 GAMMA RESPONSE OF DETECTOR A

The plastic scintillator with photomultiplier (Detector A) gave no response for the Cs^{137} source, indicating that the discriminator threshold was higher than 0.66 Mev for photons. Detector A gave angular response curves for the Co^{60} source (Figure 4.1). The scanning motion at various azimuthal and inclination angles showed that, for this very penetrating radiation, there was no multiple scattering into the detector from other parts of the package, since the count rate went to zero when the detector moved out of the beam.

4.4 GAMMA RESPONSE OF DETECTORS C AND D

Detectors C and D are identical Anton 302 GM tubes except for shielding. Both are shielded by the outer shell of the satellite with a stopping power of 1.2 gm/cm^2 of stainless steel and an aluminum mounting shell. Detector D was additionally shielded by a lead sheath having a 1.6 gm/cm^2 stopping power. Both detectors gave good directional response to both gamma sources. Count rates of Detectors C and D were recorded for fixed azimuth and inclination settings. The primary recordings were made by varying the azimuth at fixed inclinations of −60°, −30°, 0°, +30°, and +60° as shown in Figures 4.2 through 4.5; however, for cross checks the inclination angle was varied at fixed azimuthal settings of 0°, 90°, 180°, and 270° as shown in Figures 4.6 and 4.7.

4.5 GAMMA CALIBRATION RESULTS

The Detector A discriminator threshold fell between 0.66 and 1.17 Mev; therefore, it did not give angular response characteristics for Cs^{137}. The gamma radiation was so penetrating that small shielding effects did not register, as illustrated by the minimum in the count rate curve for Detector A (Figure 4.1, 0° inclination) when the crystal was facing the radiation source, despite the fact that the crystal faces an opening in the satellite shell. This result, though not at first apparent, is expected when the diameter of the plastic scintillator is much greater than the thickness. Thus, the greater depth parallel to the face of the crystal dominates the effect of the greater presented area perpendicular to the crystal face, and the opening in the shell.

The GM tubes are much more efficient for photonic radiation than Detector A, and their angular response curves can be interpreted as a superposition of shielding and presented area effects. The latter shows a typical minimum when the long axis of the GM tubes is pointed toward the radiation source. Heavy shielding effects are strikingly demonstrated in Figure 4.4, whenever Detector C is in the shadow of the lead-shielded GM tube D or in the shadow of the mercury batteries located on the deck above the detector region of the satellite. This shadowing effect will be observed only when the radiation beam enters at a small angle with respect to the satellite axis. Finally, negligible scattering was observed for the gamma radiation as was evidenced by the count rates' falling to zero when the detector section of the satellite was moved out of the radiation beam.

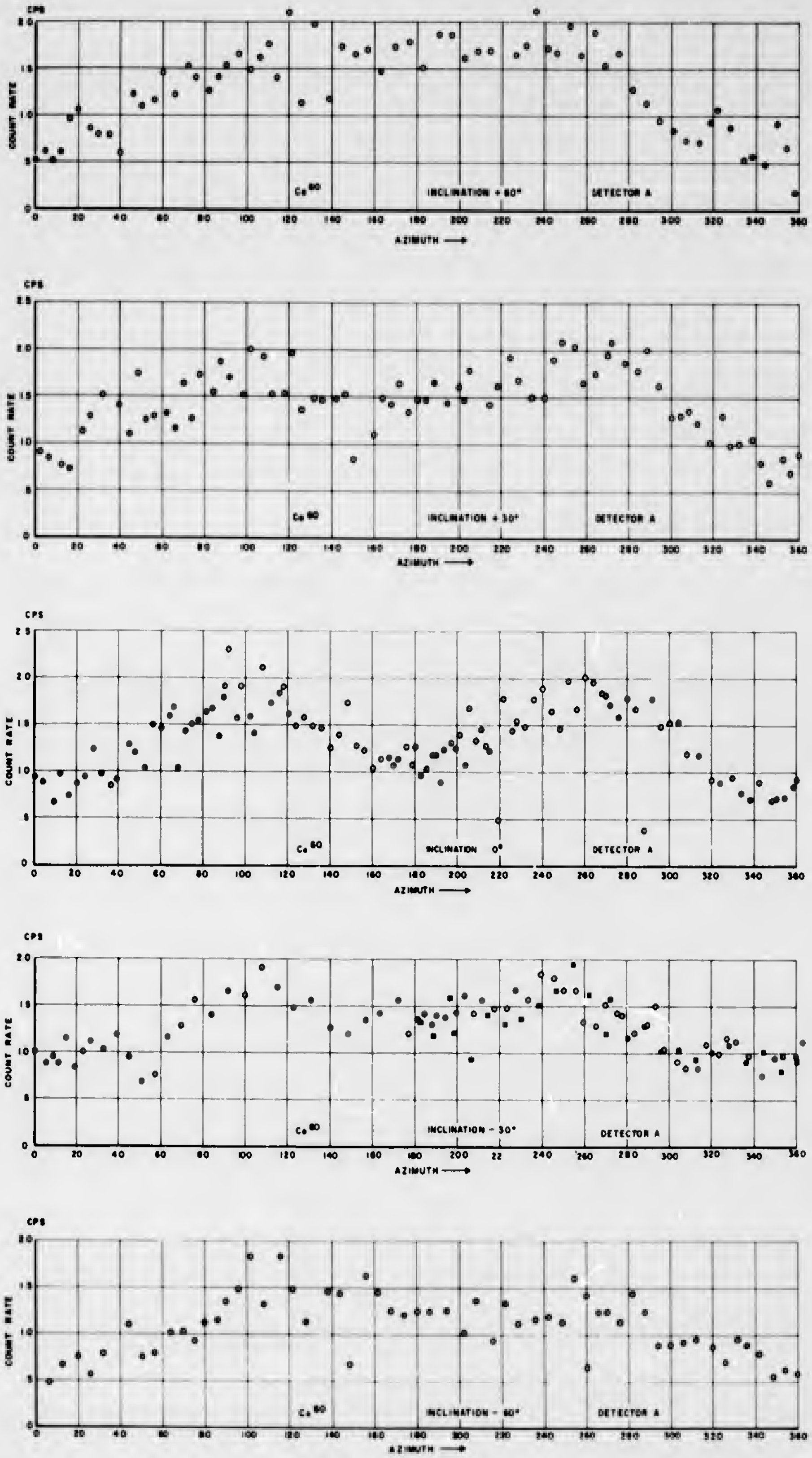

Figure 4.1 Response, Detector A, 1.17- and 1.33-Mev gammas.

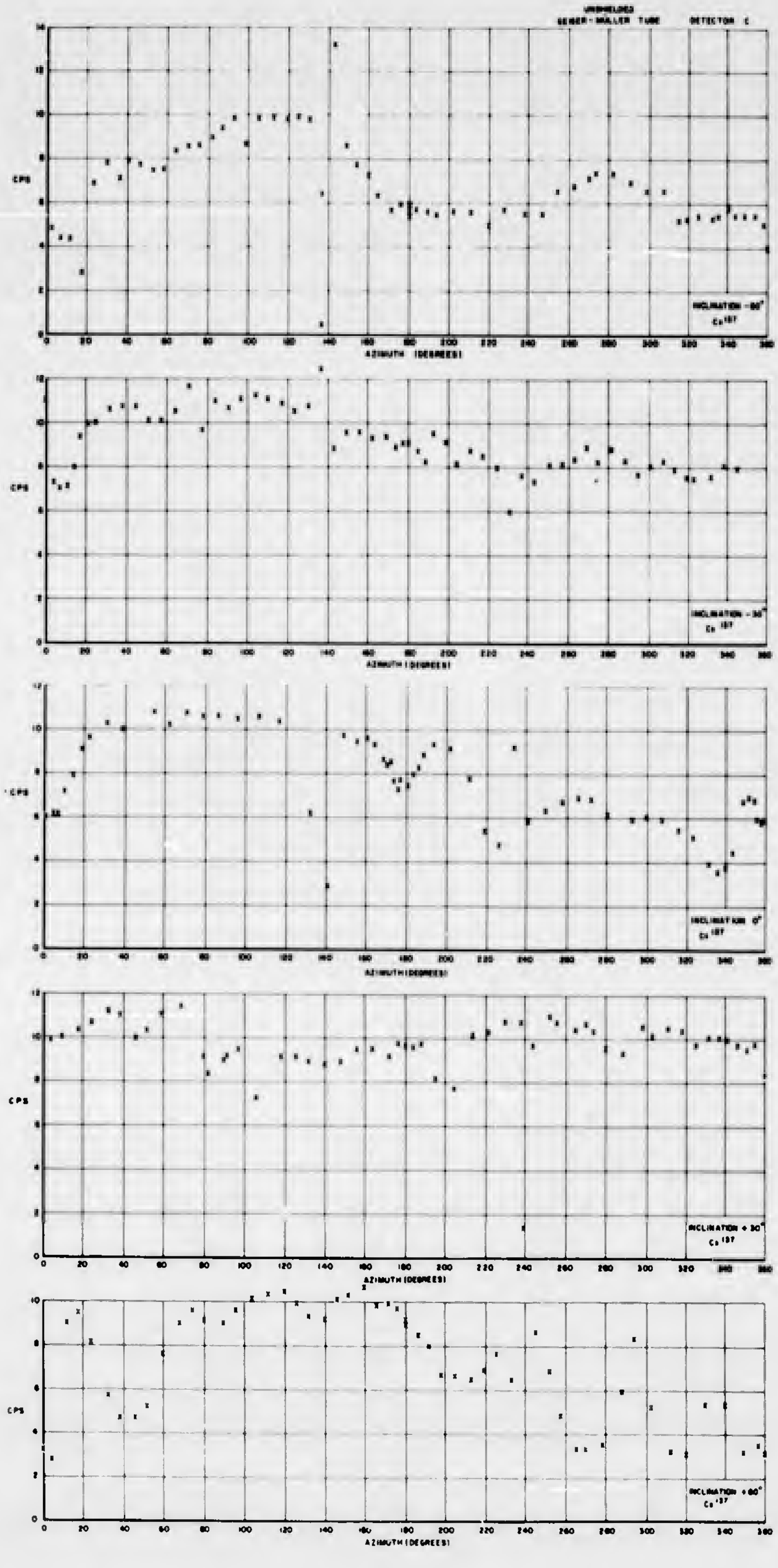

Figure 4.2 Response, Detector C, 0.66-Mev gammas.

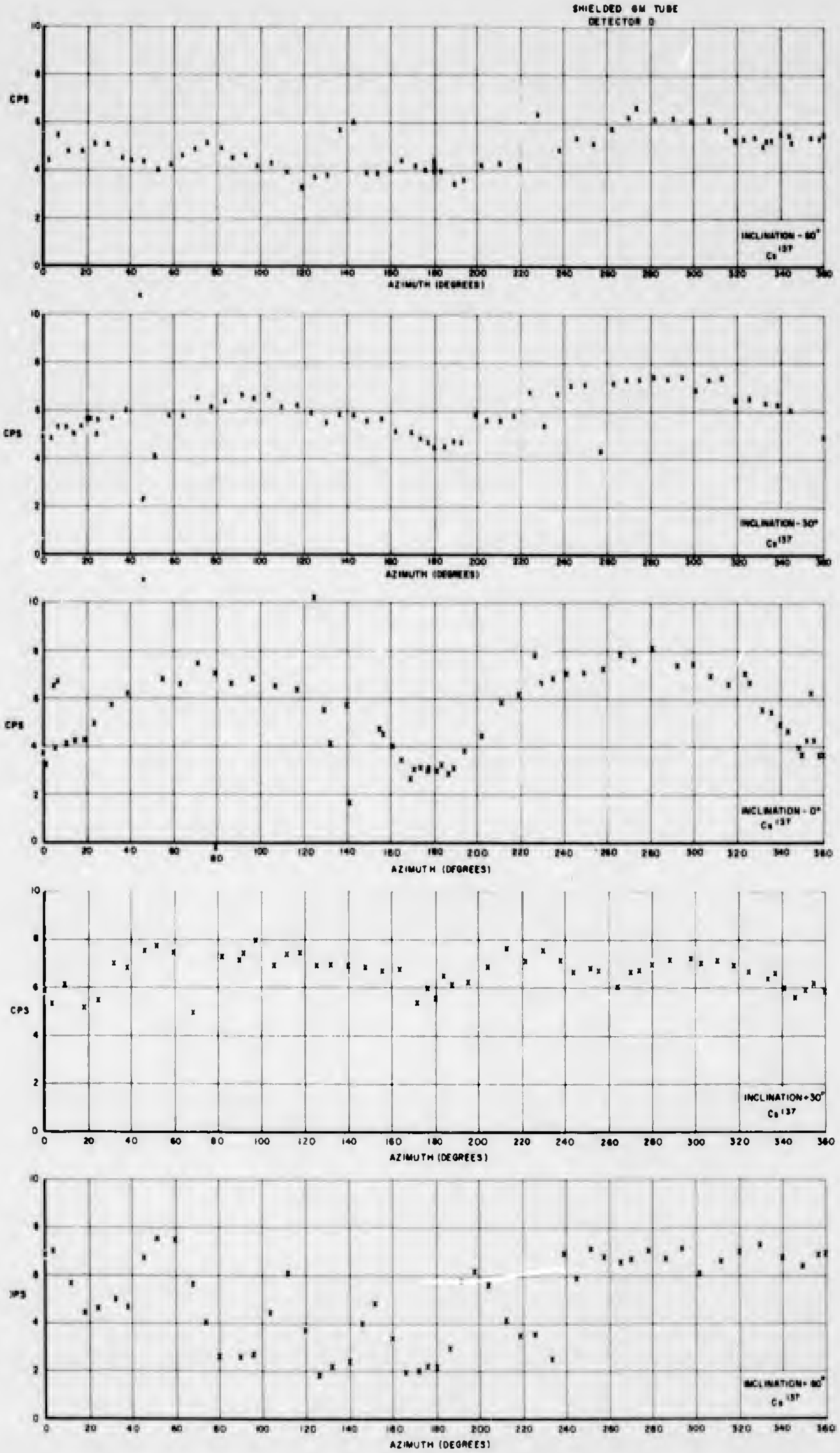

Figure 4.3 Response, Detector D, 0.66-Mev gammas.

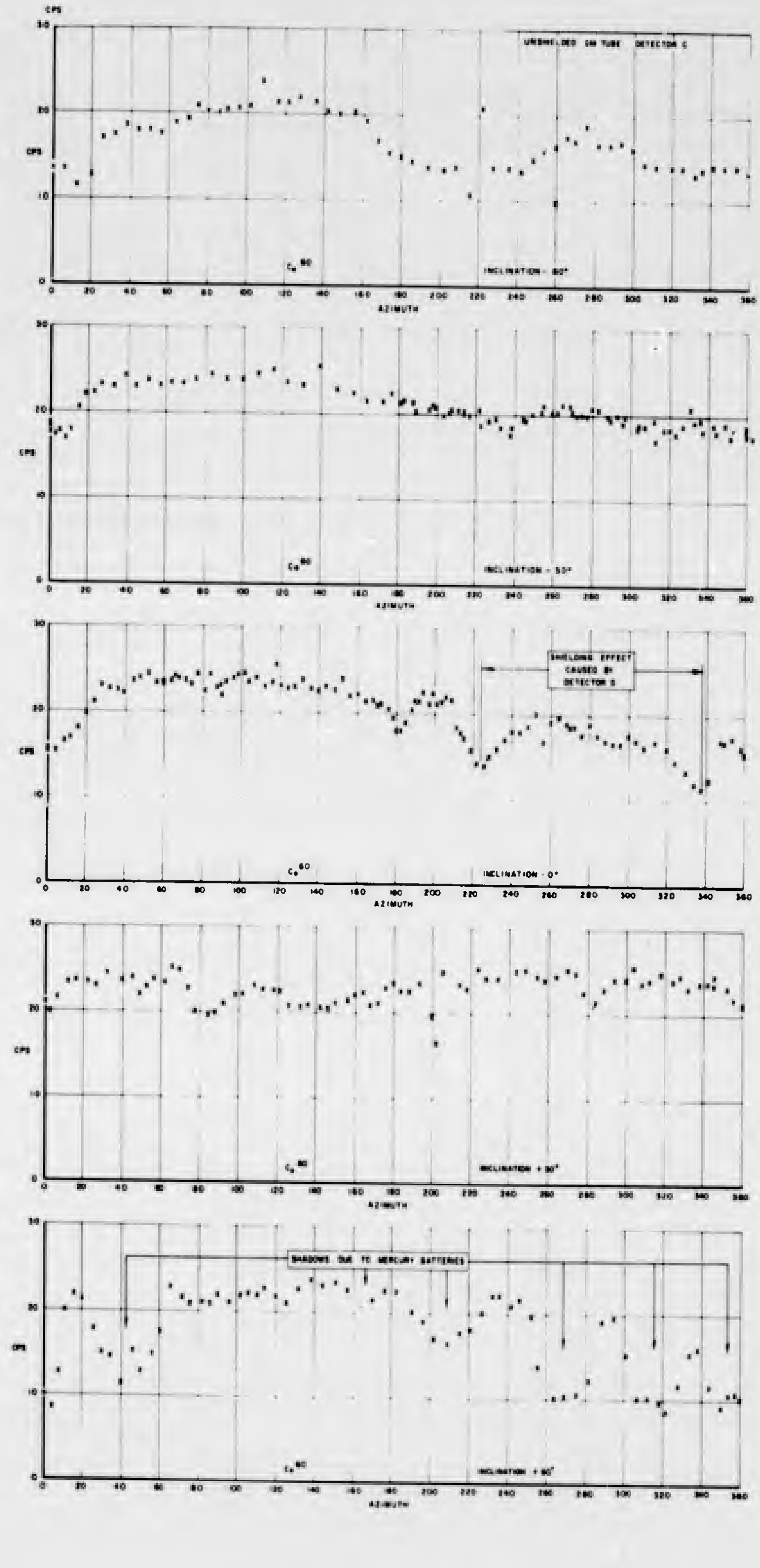

Figure 4.4 Response, Detector C, 1.17- and 1.33-Mev gammas.

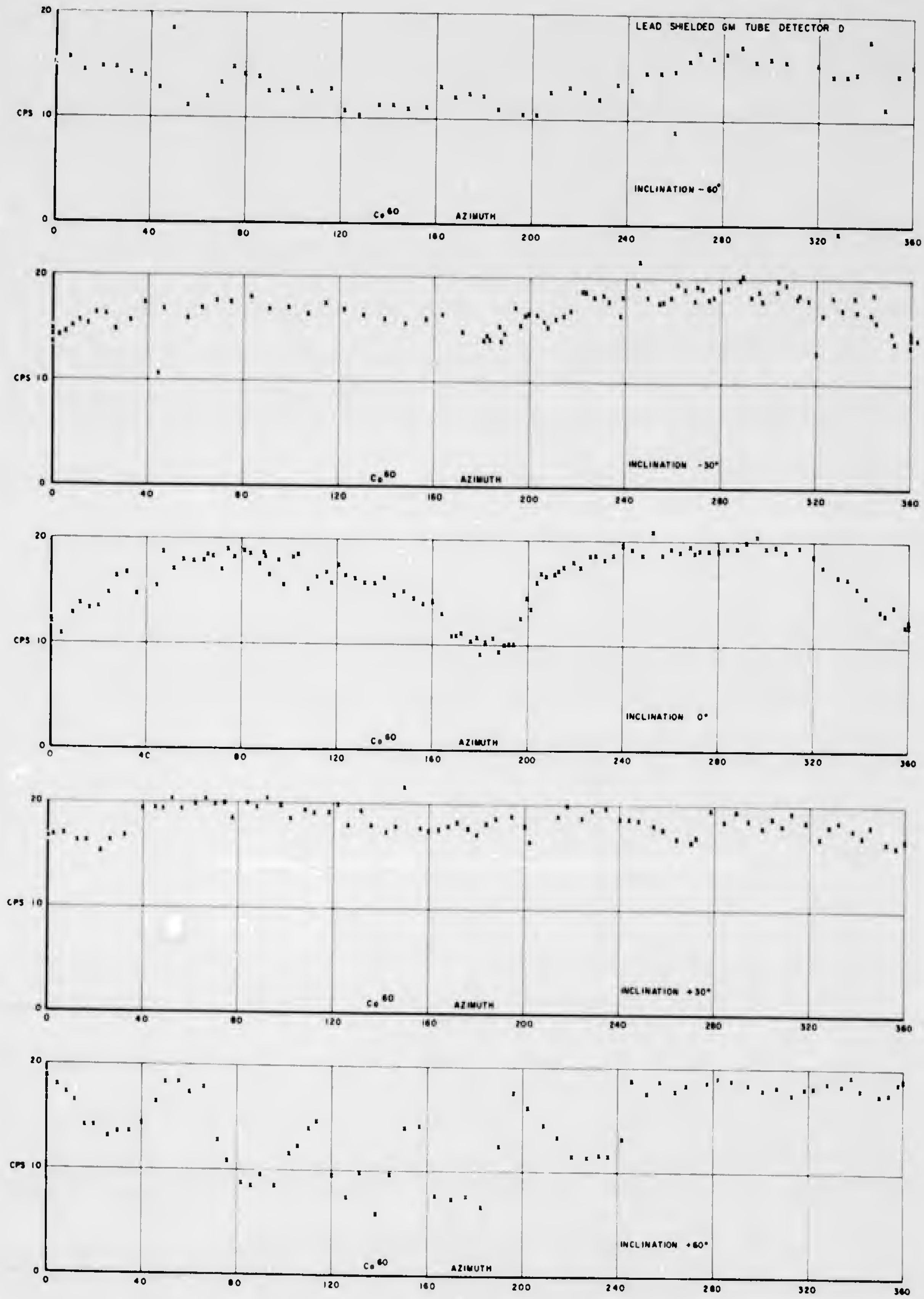

Figure 4.5 Response, Detector D, 1.17- and 1.33-Mev gammas.

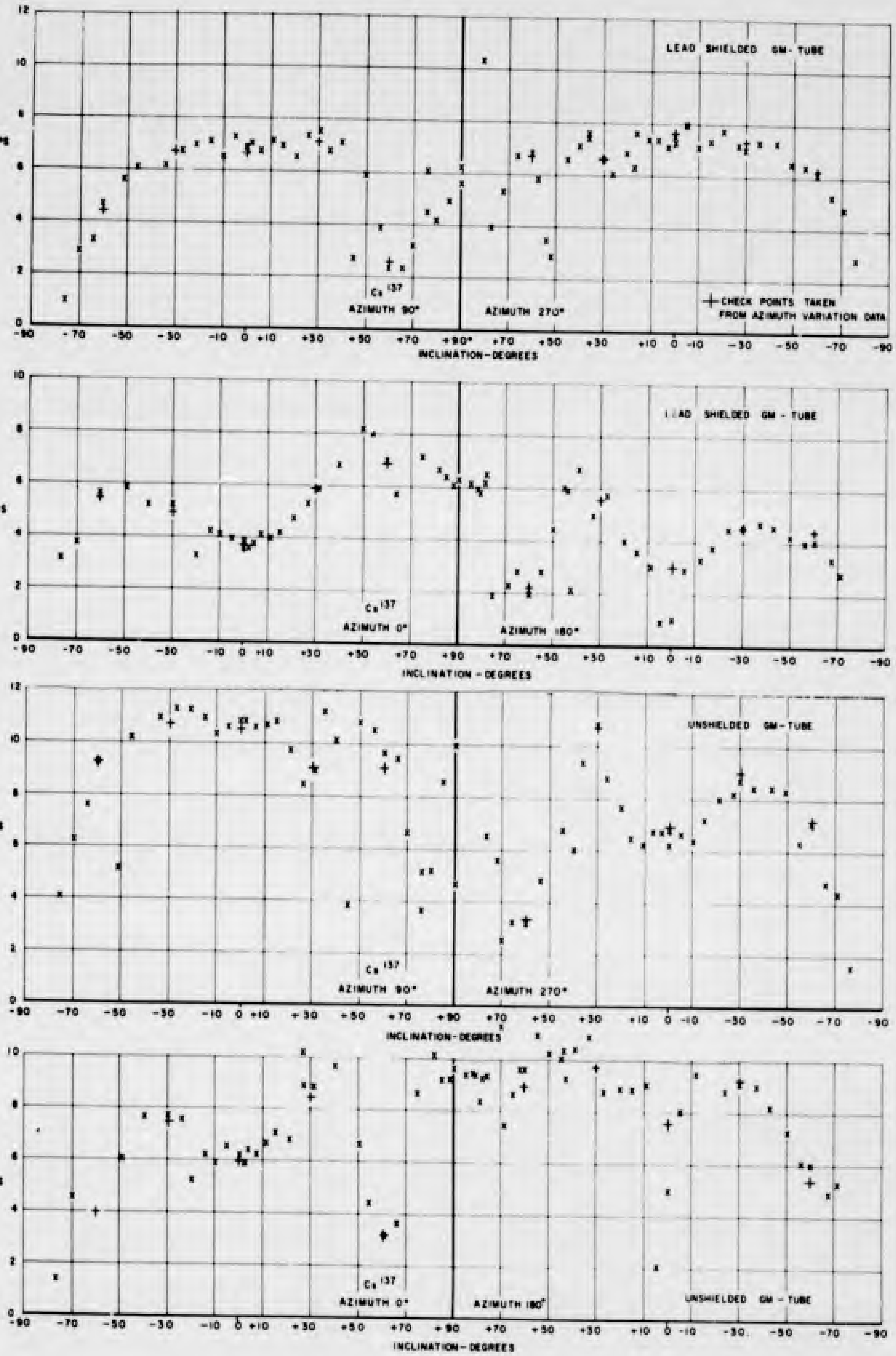

Figure 4.6 Response, Detectors C and D, 0.66-Mev gammas.

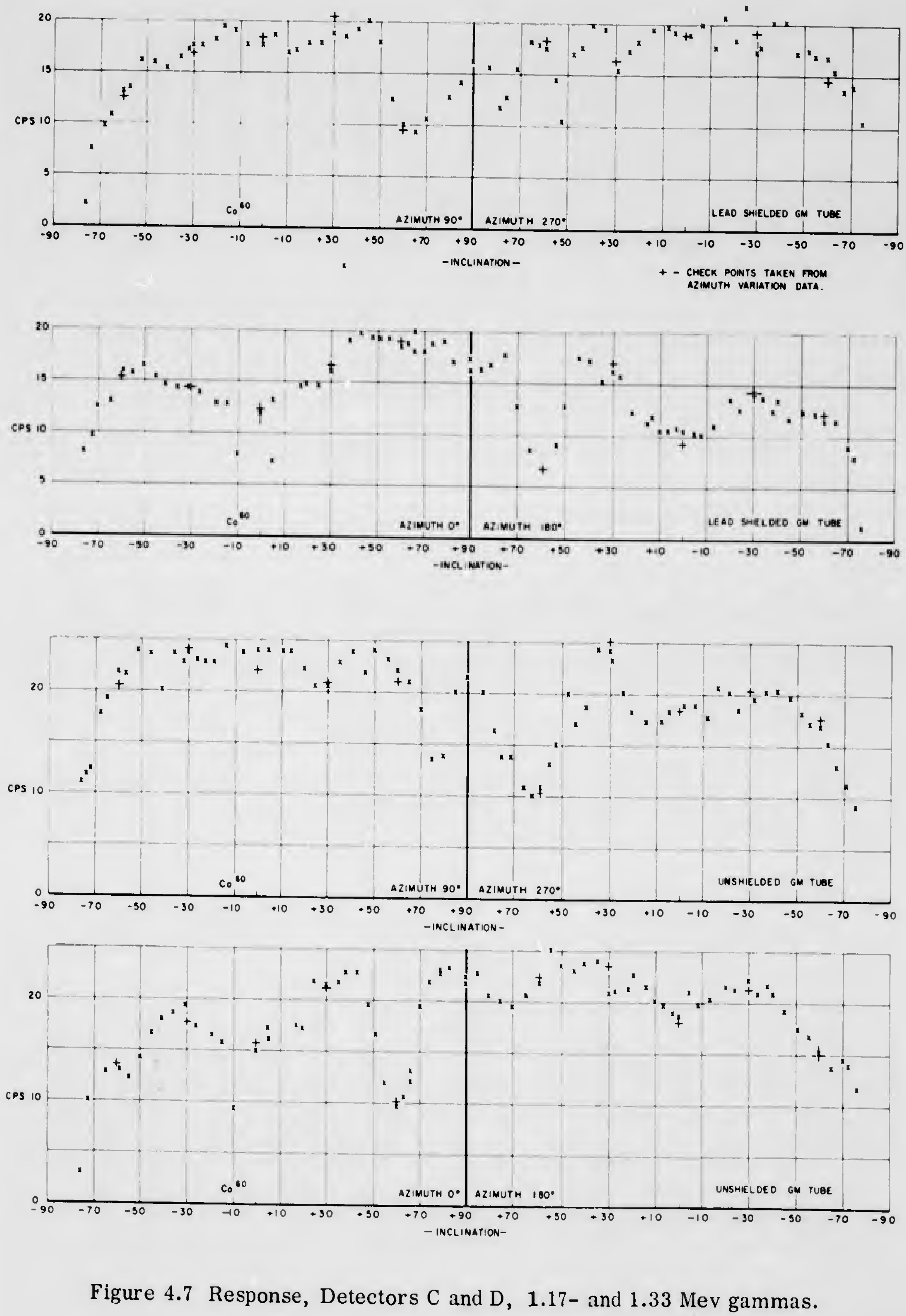

Figure 4.7 Response, Detectors C and D, 1.17- and 1.33 Mev gammas.

CHAPTER 5

X-RAY CALIBRATIONS

Because it was of particular interest to determine the window characteristic of Detector A for softer photonic radiation, the orientation device and satellite were set up in the X-ray building as shown in Figure 5.1 for further calibration.

5.1 SOURCE CHARACTERISTICS

Both the 250-kev and 1-Mev X-ray machines were available for calibration of the satellite. Spectra of these machines at various voltages were recorded prior to the test. The 1-Mev machine was used only to determine the discriminator threshold of Detector A, which was found to be between 0.66 and 1.33 Mev from the gamma ray calibration. The output of the 250-kev machine could be varied from 60 to 250 kev; therefore, this machine was used to obtain the angular response curves for the detectors. Spectra were measured by an anthracene crystal and a 256-channel analyzer. Dose rates at the position of the satellite were also measured at various voltage settings as a function of machine current. The photon flux per roentgen is given in Figure 5.2.

5.2 GEOMETRY OF X-RADIATION FIELD

The X-ray field was adjusted in the same manner as the previously described gamma ray field, except that the distance of the satellite axis from the X-ray tube reference marker was 4.92 meters. The cross section of the beam at the satellite axis was still maintained at 1 ft^2, and wall and floor scattering were determined to be negligible.

5.3 RESPONSE OF DETECTOR A TO X-RAYS

The 1-Mev machine was used first to determine the energy threshold set by the discriminator of Detector A. Detector A did not respond until the full 1-Mev voltage was applied to the machine. Thus, the photonic threshold for Detector A was found to be 1 Mev. Because the photonic radiation above threshold for Detector A was too penetrating to show up the effect of the window facing Detector A, the discriminator was bypassed, and the scintillator pulses were fed directly into an external amplifier which was adjusted to discriminate against noise. In this condition, linear responses were obtained at very high count rates, attesting to the fact that the dead time of Detector A was set by the scaler (Figure 5.3).

The 250-kev machine was used to determine the window characteristic of Detector A. Because even at the lowest voltage setting of 60 kev an appreciable amount of shell-penetrating radiation was registered, a differential method was used to study the effect of the open window hole. Each variation of orientation was run twice under exactly the same conditions, with the exception that in one case the window opening was covered by a stainless steel lid and later by a lead stopper. The difference in the response is obviously the amount of radiation entering the open window. Window response curves for Detector A at 60 and 100 kev are shown in Figures 5.4 through 5.6.

The differential method demonstrates that the window-type detector recordings consist of a directional plus a shell-penetrating omnidirectional component. That is, $N = N_{direct}(\varphi, \theta) + N_{omni}$. With increasing energies, the omnidirectional component obscures the directional component as was demonstrated by the gamma calibration. Even for the soft X-rays, there was no apparent scattering into the detectors when they were completely out of the beam; thus, multiple scattering can be neglected.

5.4 RESPONSE OF GM TUBES TO X-RAYS

Since the relationship between current of the X-ray machine and radiation flux density is practically linear (see Figure 5.7), the count rates have been plotted as a function of current density as in Figure 3.2. The maximum count rate was found at 2000 cps where the GM tube saturated. A further increase of radiation flux produced a monotonic decrease of count rate—a well-known characteristic of GM tubes. It should be mentioned that the usual dead-time correction based on the assumption of an exponential saturation curve is of limited value in this case. The count rate curves as a function of orientation were similar to those for the gammas.

5.5 RESULTS

The primary result for Detector A was the establishment of the 1-Mev threshold for the detector. Although, in the flight package, this detector would not measure any photonic radiation below the 1-Mev threshold, it was desirable to determine the window characteristics of the detector at lower energies for later use in checking consistency of data for other types of radiation and for checking extrapolation formulas.

Because the X-rays were not monoenergetic but consisted of a bremsstrahlung spectrum a considerable amount of data processing was necessary to produce useful results. Figure 5.8 shows the count rate plotted as a function of voltage for a 2-ma current setting. Figure 3.2 shows count rate as a function of current when the voltage is held constant. Cross checks between the two figures gave additional information for error compensation in order to produce consistent count rate functions such as:

$$N = N(V, i) = N'(E, I) \tag{5.1}$$

Where: V = machine voltage
i = machine current
E = energy
I = radiation intensity

Detector C count rate appears as a linear function. The nonlinearity of Detector D response is due to the lead shielding. The exact threshold energy of Detector D can be determined by extrapolation of the count rate ratio of Detectors D and C as in Figure 5.9.

$$\lim_{V \to 50\text{ kev}} \frac{N_D(V)}{N_C(V)} = 0 \tag{5.2}$$

With a continuous bremsstrahlung spectrum, the pertinent energy interval is

$$V_{threshold} = E_{threshold} < E < E_{end} = V \tag{5.3}$$

whereby both the end point energy E_{end} and threshold energy $E_{threshold}$ are given by the machine voltage V.

The count rate N(V) as a function of the machine voltage V can be expressed as,

$$N(V) = \int_{E_{threshold}}^{E_{end}} A_{eff}(E) \cdot J(E) \cdot dE \tag{5.4}$$

where J(E) is the differential intensity of the bremsstrahlung spectrum and $A_{eff}(E)$ is the effective area as a function of energy. The integral intensity I is given by

$$I = \int_{E_{threshold}}^{E_{end}} J(E)\, dE \tag{5.5}$$

Because the count rate ratio of the monochromatic radiation equals the ratio of the corresponding effective areas, the following relation can be derived as

$$\frac{N_D(V)}{N_C(V)} \leq \frac{N_D(E)}{N_C(E)} = \frac{A_{eff}\, D(E)}{A_{eff}\, C(E)} \tag{5.6}$$

therefore, equality exists only for

$$N_D(V) = N_D(E) = 0 \tag{5.7}$$

showing that the threshold energy extrapolation is correct.

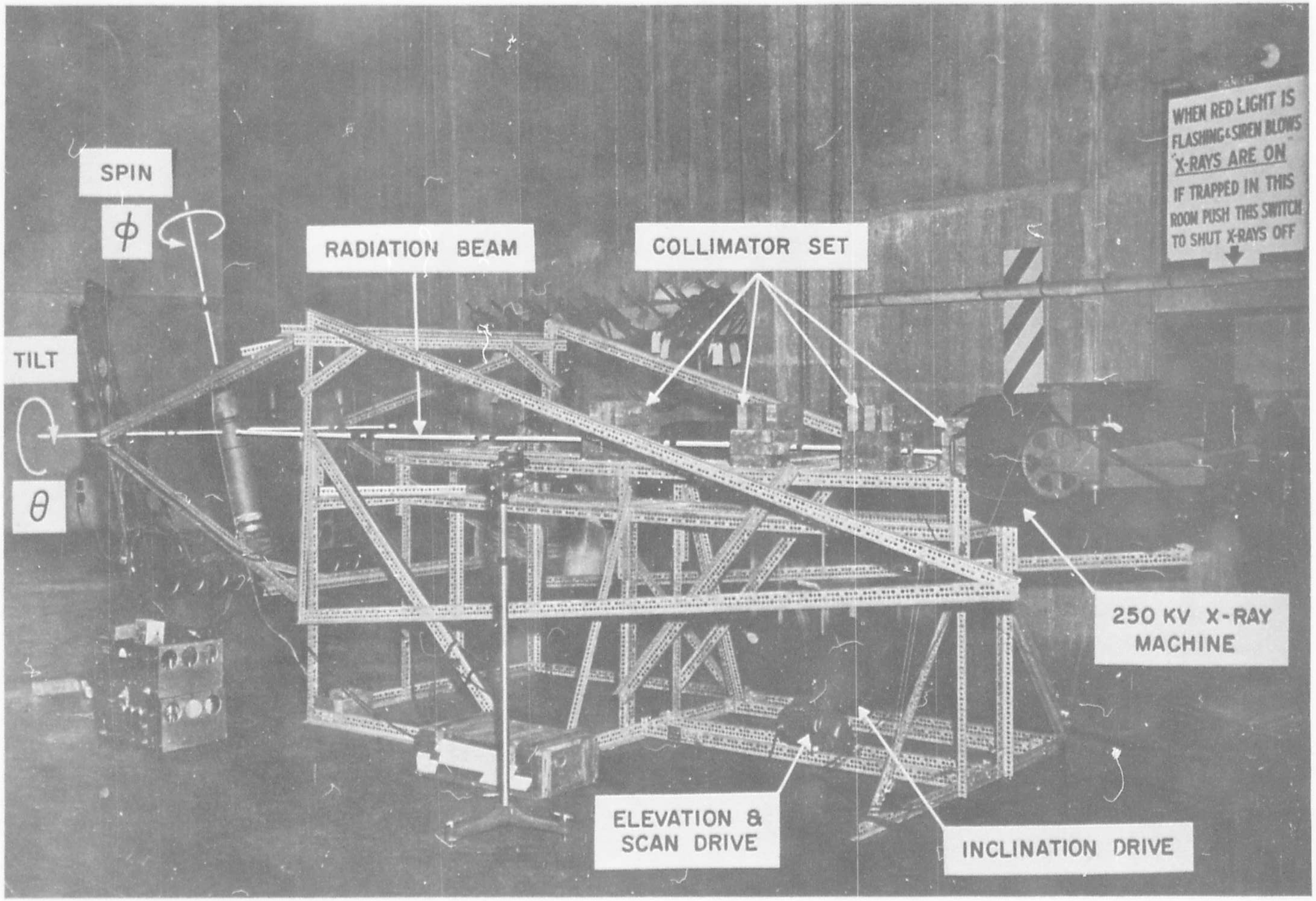

Figure 5.1 X-ray laboratory setup. (BRL photo)

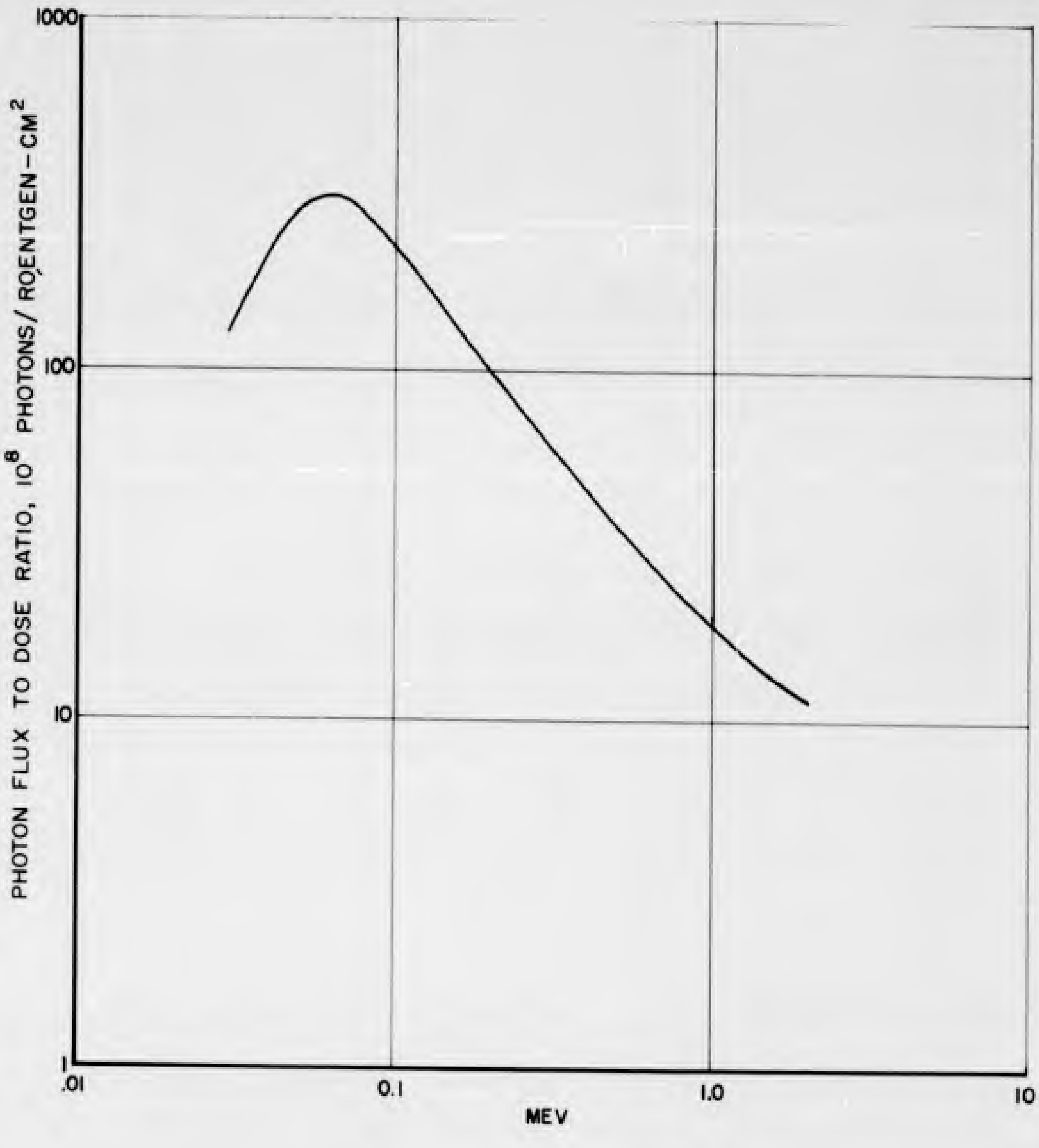

Figure 5.2 Photon flux per dose as a function of energy.

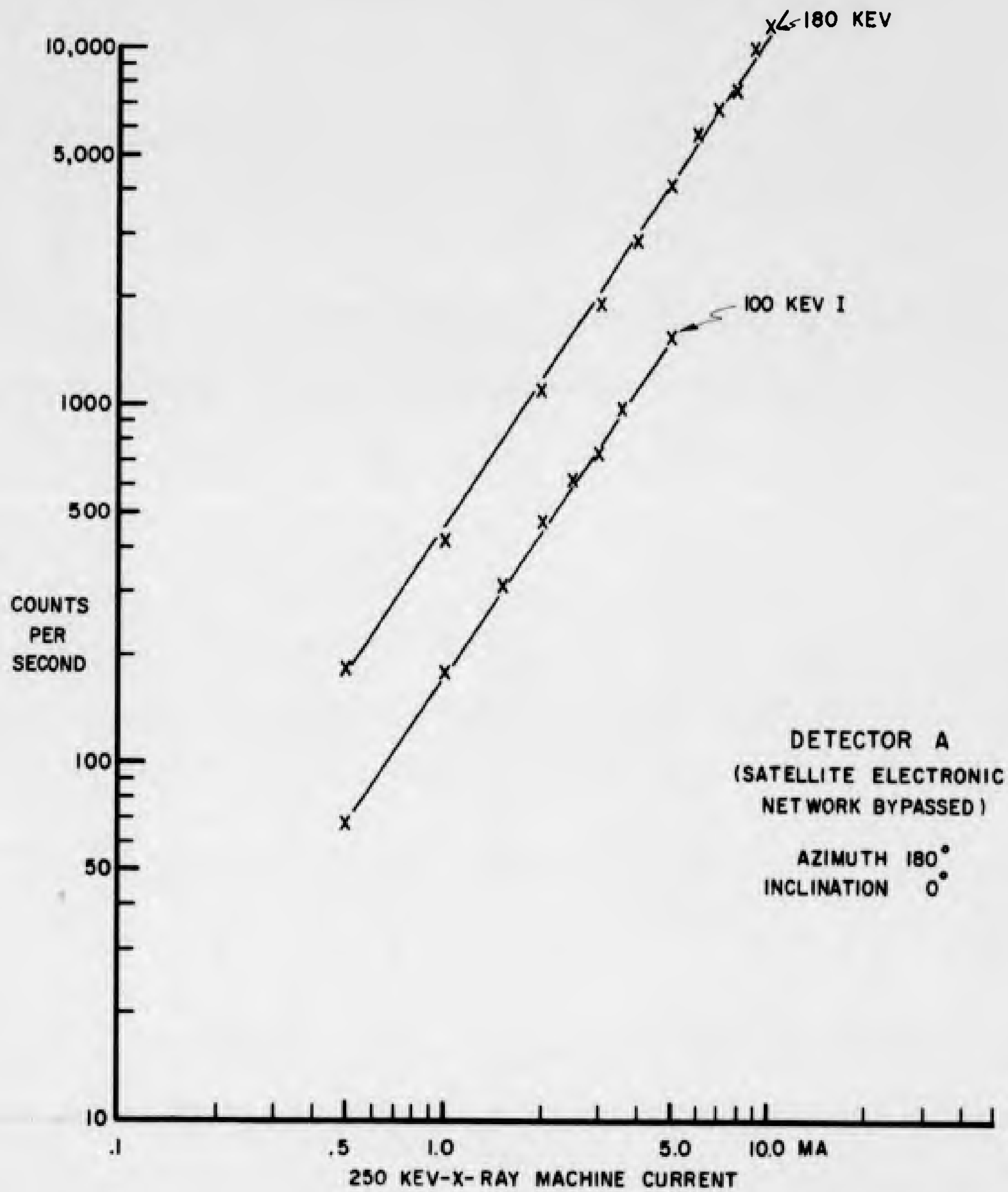

Figure 5.3 Response of Detector A to current variation.

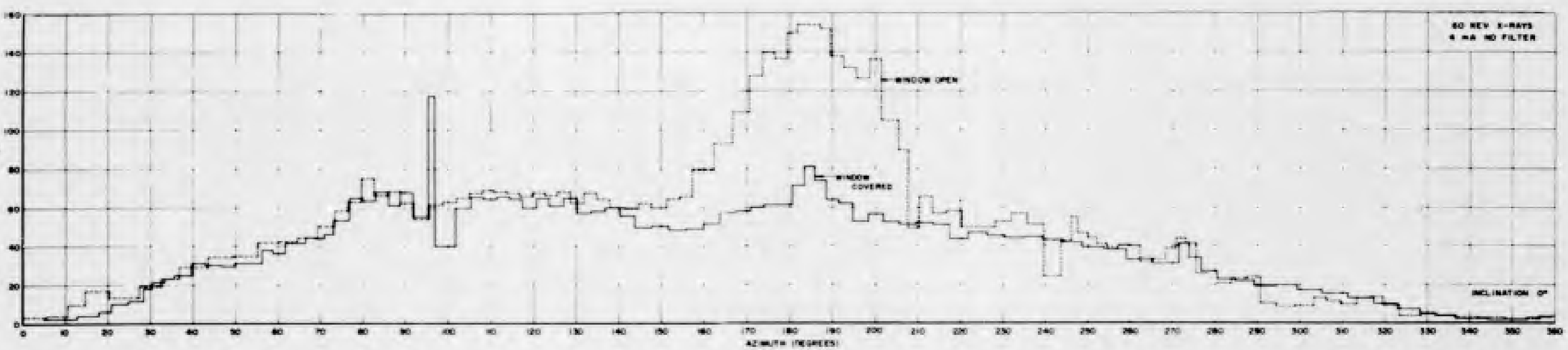

Figure 5.4 Angular response, Detector A, X-rays at 60 kev (4 ma).

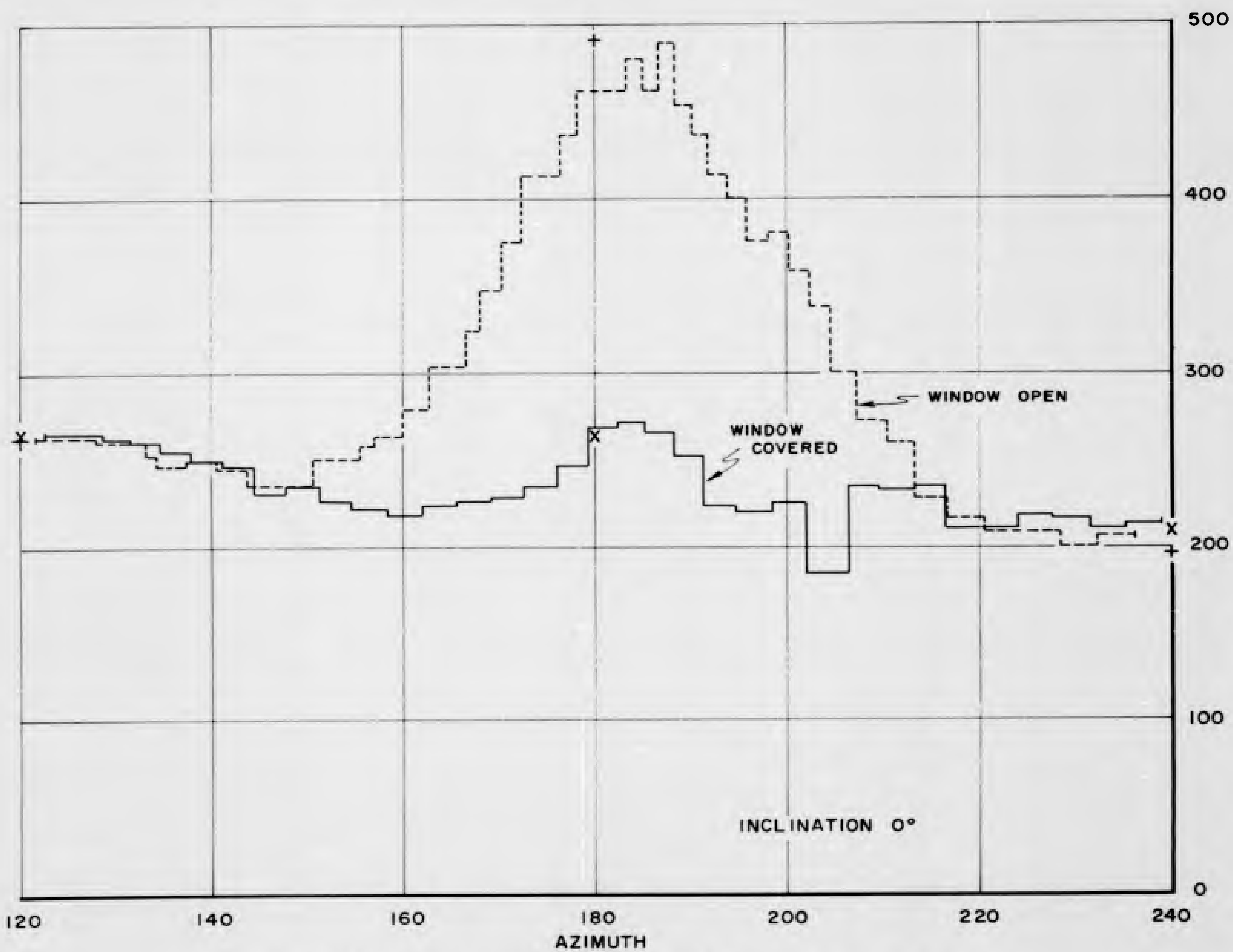

Figure 5.5 Angular response, Detector A, X-rays at 100 kev (2 ma), 0° inclination.

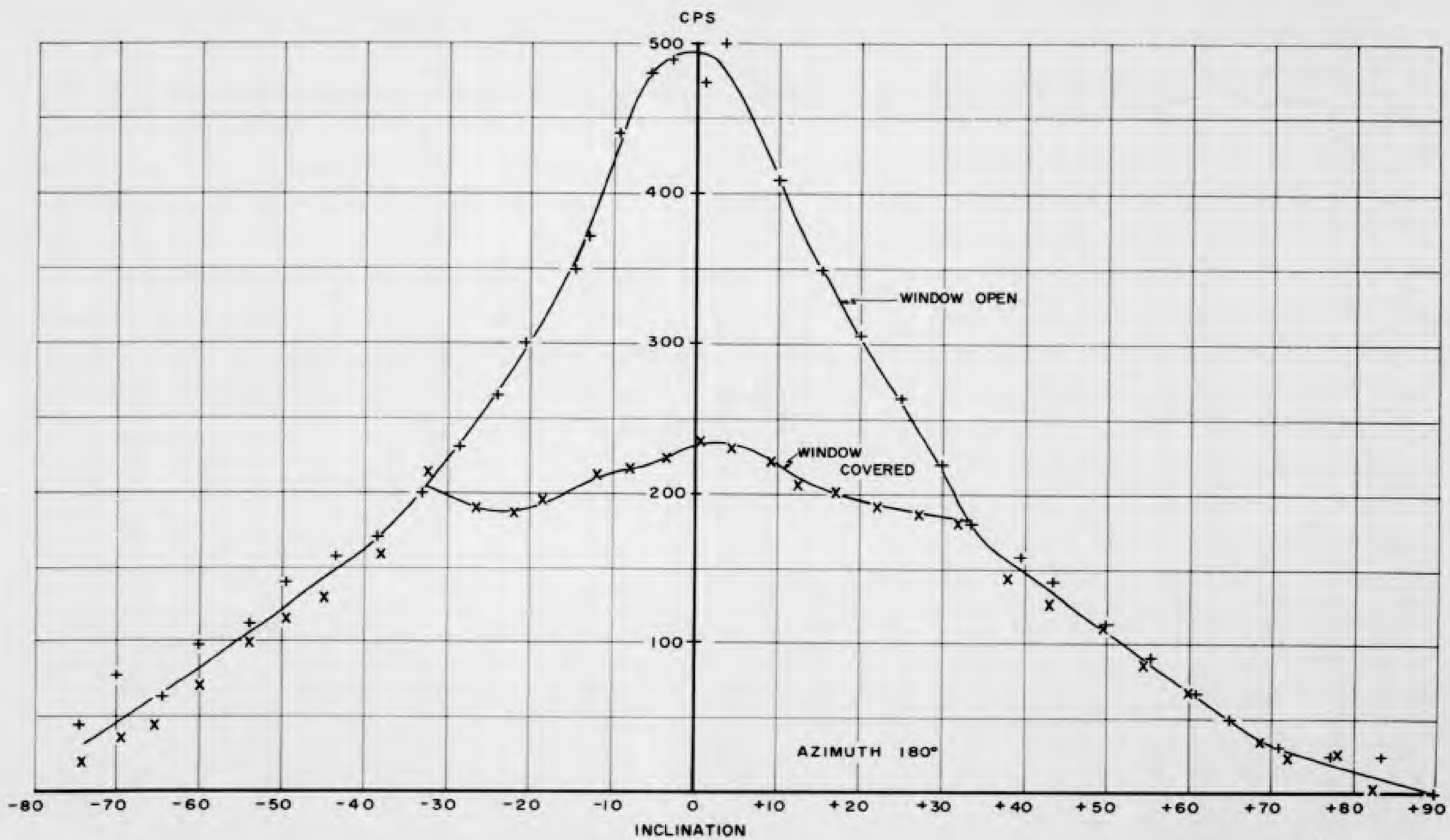

Figure 5.6 Angular response, Detector A, X-rays at 100 kev (2 ma), 180° azimuth.

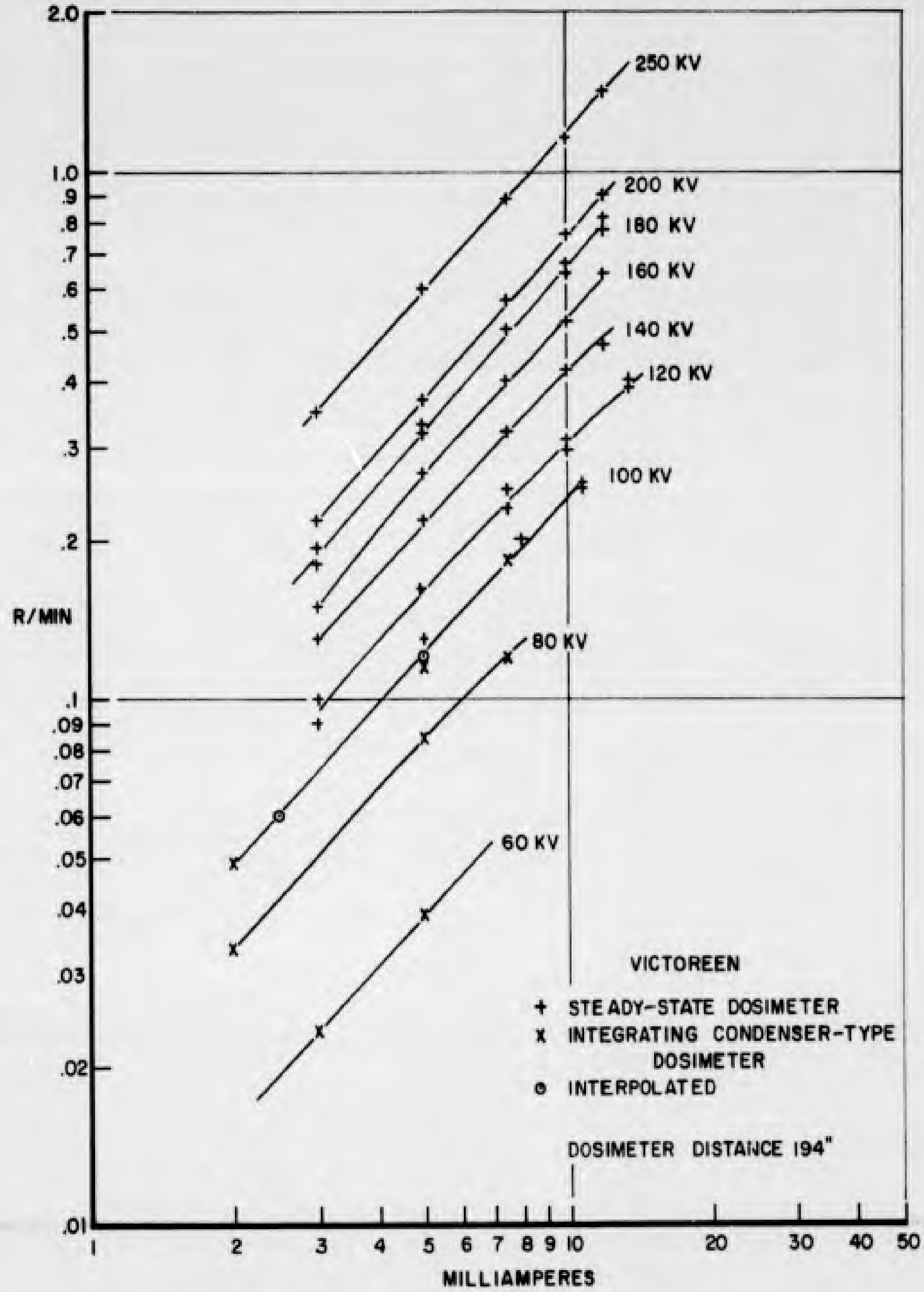

Figure 5.7 Dosimetric calibration of X-ray machine, 27 Nov 61.

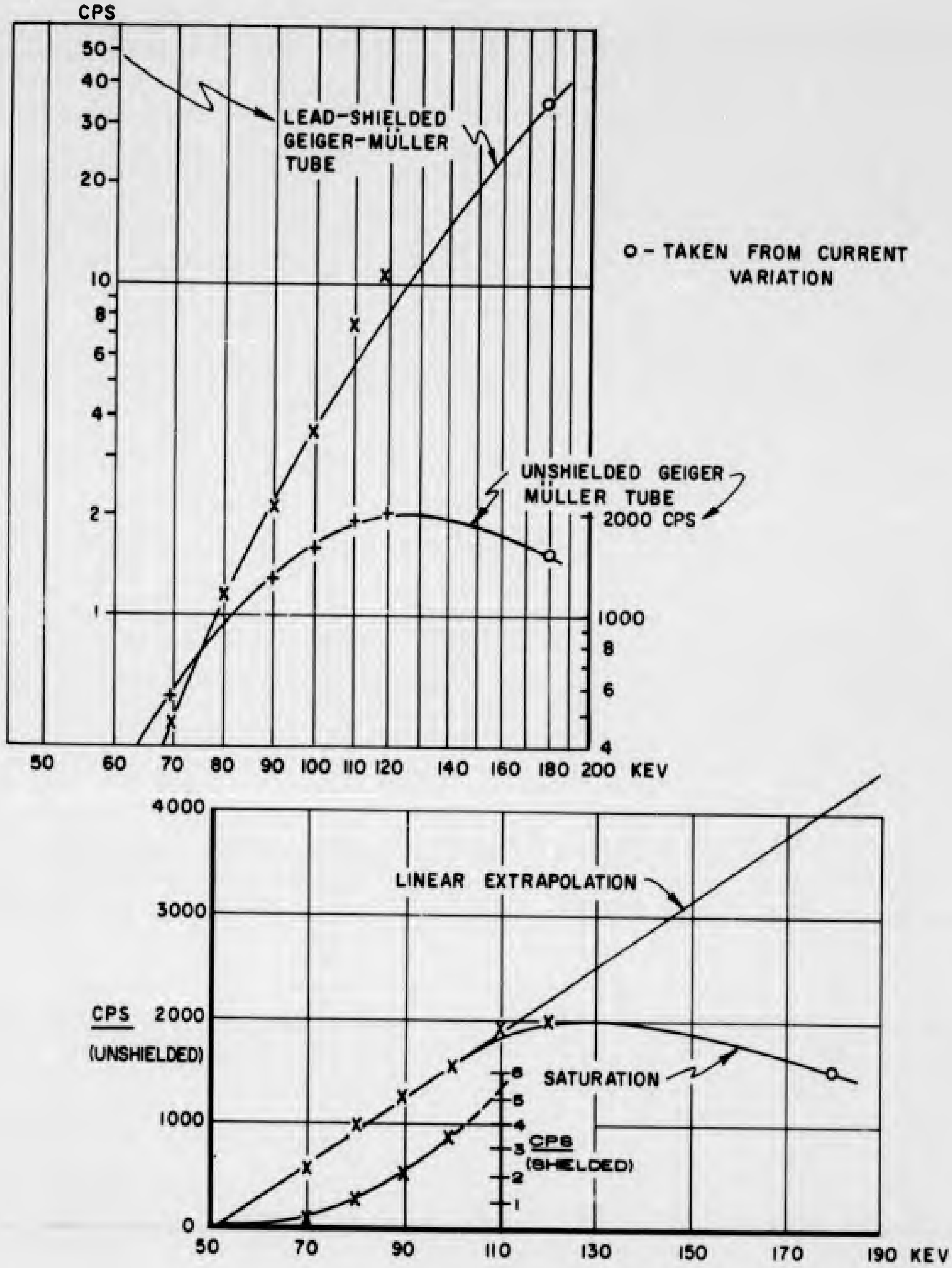

Figure 5.8 Response of GM counters to voltage variation.

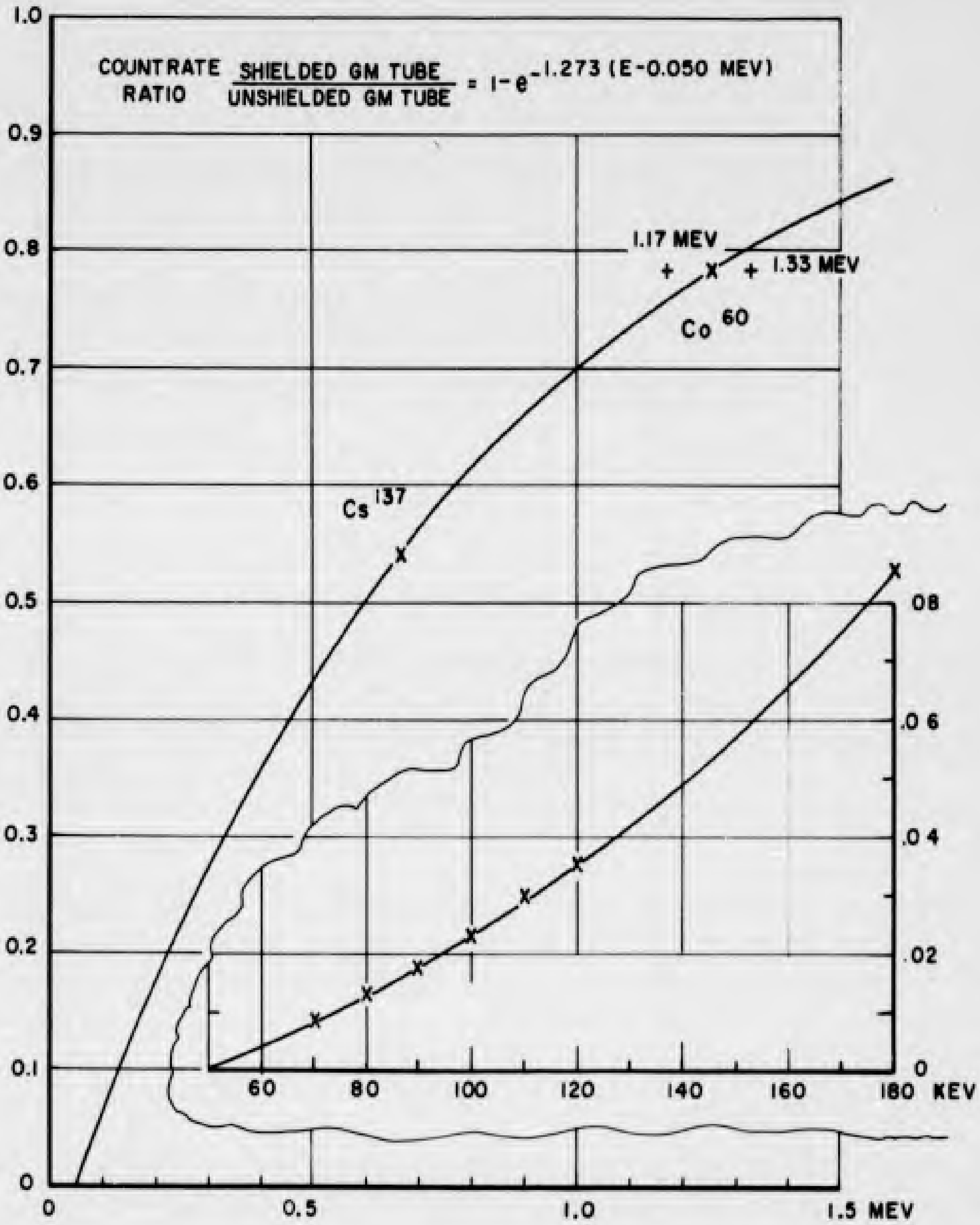

Figure 5.9 Count-rate ratio.

CHAPTER 6

BETA RAY CALIBRATION

For the beta ray calibration it was necessary to move the orientation device into the 30-foot high-altitude chamber on Spesutie Island (Aberdeen Proving Ground). The calibration procedure was the same as for the gammas and X-rays with a few exceptions, which will be noted. The setup for the sphere is shown in Figure 6.1.

6.1 BETA SOURCE CHARACTERISTICS

For this calibration it was necessary to design and build a special 90° beta spectrometer shown in Figure 6.1. The electromagnet was designed in such a manner that it acted as an energy selector for a 1-curie Y^{91} beta source (end point energy = 1.5 Mev), which was held in a chamber within the homogeneous field of the electromagnet. The field strength was measured as a function of magnet current by means of a Bell 120 gaussmeter; thus, a calibration chart giving particle energy in Mev versus amperes was constructed (Figure 6.2) using the appropriate $B\rho$ values (Reference 4). The energy distribution of the external electron beam at various field strengths was measured with an anthracene crystal on a RCA 6292 photomultiplier tube and a RCL 256-channel analyzer.

The intensities at various field strengths were measured by a gold-surface-barrier solid-state detector (Figure 6.3). The intensity peaks were recorded on a 256-channel analyzer. The spectrum was measured in vacuum with an A58-64B-Ortec solid-state detector at a distance of 860 mm from the analyzer magnet. After comparison with the 630-kev beta-peak of Cs^{137}, it was found that the peak energies checked with the magnet calibration chart (Figure 6.4). With the magnet, it is possible to select beta energies between peak energies of 200 kev and 1.1 Mev of useful intensity.

6.2 RADIATION FIELD GEOMETRY

No external collimator was used except for the data taken at 4.335 meters (Figures 6.5 and 6.6). In this case, the collimation is the same as previously described for the gamma and X-ray calibration. Most of the measurements were taken at a distance of 2.685 meters. To obtain higher intensities at this short distance, a small parallax angle correction was necessary, because the window displacement at various orientations could not be neglected, compared with the relatively short radial distance from the source. Because all measurements were made at a pressure of 30 mm of mercury, it was necessary to make a small correction for air scattering. It was not possible to operate at pressures lower than 30 mm, because discharges occurred in the high-voltage systems of the satellite. Several experiments were performed to determine the influence of air scattering on the results. The count rate, recorded by a monitor, was plotted versus absolute pressure as $N = N(P)$ to find the discharge point (Figure 6.7). Angular window response characteristics, $N = N(\varphi, \theta, P)$, were recorded at pressures of 30 and 50 mm of mercury, absolute. These were compared at various distances of 2.685 and 4.335 meters. Furthermore, a circular-aperture collimator was mounted in front of the

Detector A window in such a way that there was transmission only when the collimator was pointing directly toward the electron source. As a result of air scattering, a nearly triangular response curve was obtained over the variation of azimuth and inclination, which is called the scatter characteristic (Figures 6.8 through 6.10).

To eliminate the error produced by scattering, the experimentally measured curve

$$f(x) = N(\varphi, 0°, 30 \text{ mm Hg}) \text{ resp. } N(0°, \theta, 30 \text{ mm Hg}) \tag{6.1}$$

was considered as the folding integral of the window response in vacuum

$$F(\xi) = N(\varphi, 0°, -\text{mm Hg}) \text{ resp. } N(0°, \theta, 0 \text{ mm Hg}) \tag{6.2}$$

and the scatter characteristic

$$\Psi(\xi - x) = N^*(\varphi, 0°, 30 \text{ mm Hg}) \text{ resp. } N^*(0°, \theta, 30 \text{ mm Hg}) \tag{6.3}$$

in the form of

$$f(x) = \int_{-\infty}^{+\infty} F(\xi) \cdot \Psi(\xi - x)\, d\xi \tag{6.4}$$

The folding process was performed on an analog computer where $F(\xi)$ was iterated until the average deviation of the folding integral from f(x) was less than 1.9 percent for azimuth and 0.95 percent for inclination. This procedure was used to correct the data for the 0.63- and 1.06-Mev electrons. Because of the low intensity, no scatter characteristic with the collimator could be observed for 0.23-Mev electrons. An example of the corrected azimuthal and inclination data for scattering is shown in Figures 6.11 and 6.12.

6.3 RESPONSE OF DETECTOR A

Window response curves were measured at various energies, which were indicated by the selector magnet currents such as:

0.8 ampere, 0.23-Mev peak energy (Figures 6.13 and 6.14)
1.6 amperes, 0.63-Mev peak energy (Figures 6.11 and 6.12)
1.8 amperes, 0.73-Mev peak energy (Figure 6.15)
2.4 amperes, 1.06-Mev peak energy (Figures 6.16 and 6.17)

The magnet current was also varied continuously while the detector was pointing at the source (azimuth 180°, inclination 0°) obtaining

$$N = N'(i) \quad i = \text{magnet current}$$

$$= N(B) \quad B = \text{magnet field strength} \tag{6.5}$$

In this manner the energy spectrum of the Y^{91} source was measured by Detector A (Figures 6.18 and 6.19). The pulse height discriminator of Detector A was made ineffective during most recordings, to obtain high count rates. The discriminator setting was at 700 kev for electrons, which was verified by recording the spectrum with and without the discriminator and plotting the ratio of count rates as,

$$r = \frac{N_{discr}(B)}{N(B)} \tag{6.6}$$

which appears as a smooth step function with the half-value at 1.75-ampere magnet current, which corresponds to an energy of 700 kev (Figures 6.20 and 6.21). The spectra of the magnet selector output, recorded using an anthracene crystal, photomultiplier, and 256-channel analyzer, at various field strengths, was planimetered, and a ratio of the integral intensity above 700 kev to the total intensity was formed as:

$$r' = \frac{\int_{700\ \text{kev}}^{\infty} H(E)dE}{\int_{0}^{\infty} H(E)\,dE} \tag{6.7}$$

which is proportional to the previous discrimination ratio (Equation 6.6) introducing a coefficient called the discriminator transmission efficiency ϵ. Then

$$r = \epsilon r' \quad \text{or} \tag{6.8}$$

$$\frac{N_{discr}(B)}{N(B)} = \epsilon \frac{\int_{700\ \text{kev}}^{\infty} H(E) \cdot dE}{\int_{0}^{\infty} H(E)\,dE} \tag{6.9}$$

ϵ has to be a constant, provided the assumption of the sharp discrimination at 700 kev is correct. It was found that ϵ = 9.3 percent, or more precisely

when $E < 700$ kev, $\epsilon = 0$

when $E \geq 700$ kev, $\epsilon = 9.3 \pm 0.3$ percent
(Figures 6.22 and 6.23) (6.10)

The beta radiation was not sufficiently penetrating to give readings on the GM tubes.

6.4 RESULTS

For Detector A response curves were measured over the energy range from 0.2 to 1.5 Mev. The half-width of the angular response curve of Detector A for photonic radiation is about 30 percent broader than that obtained for electrons. Over the measured electron energy range, the angular response curves were found to be almost independent of energy.

It was not possible to obtain any recordings from electrons up to 1.5 Mev with the GM tubes (Detectors C and D) because of the shielding. Because there were no window openings facing the GM tubes, all electrons reaching the tubes must necessarily penetrate the satellite shell, which has a stopping power of 1.2 gm/cm^2. Because of low conversion efficiency, it was not possible to record any bremsstrahlung produced by incident electrons on the shell.

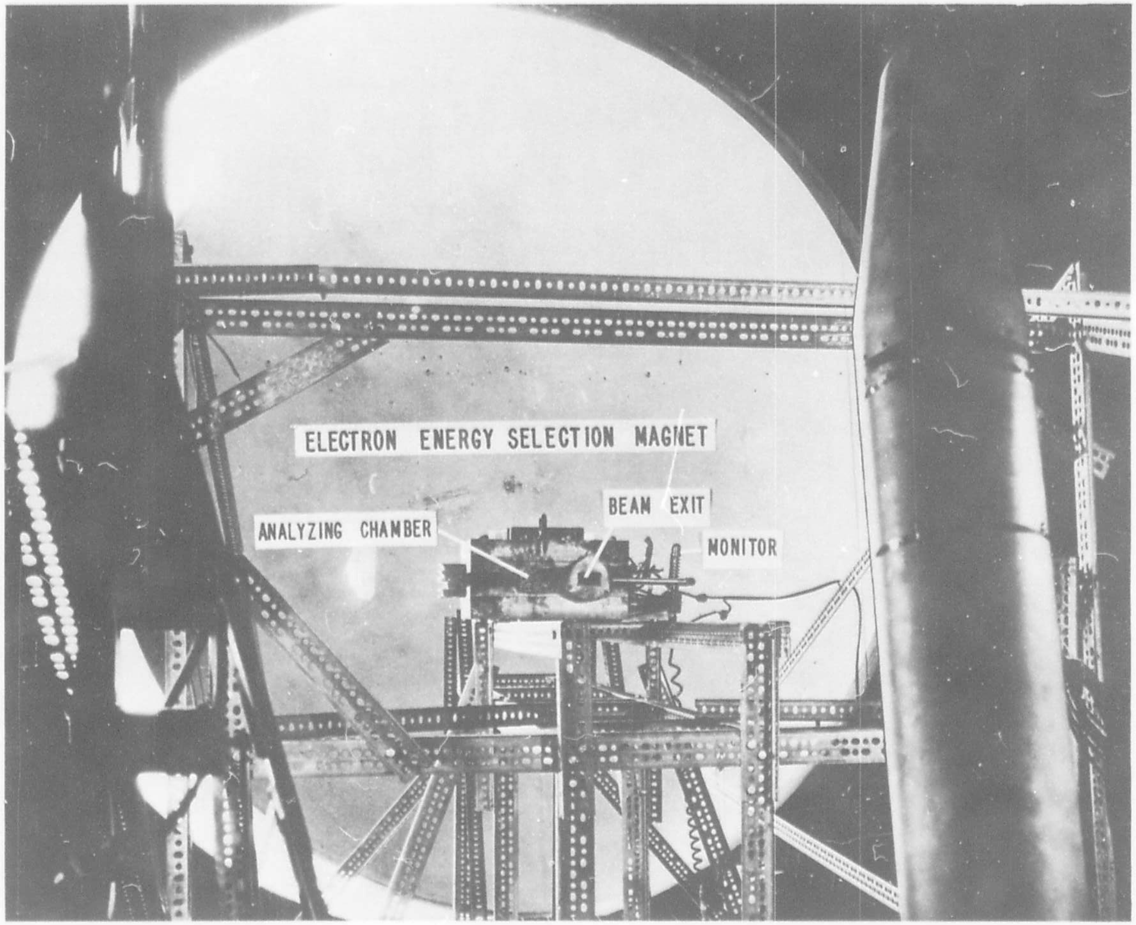

Figure 6.1 Electron energy selection magnet. (BRL photo)

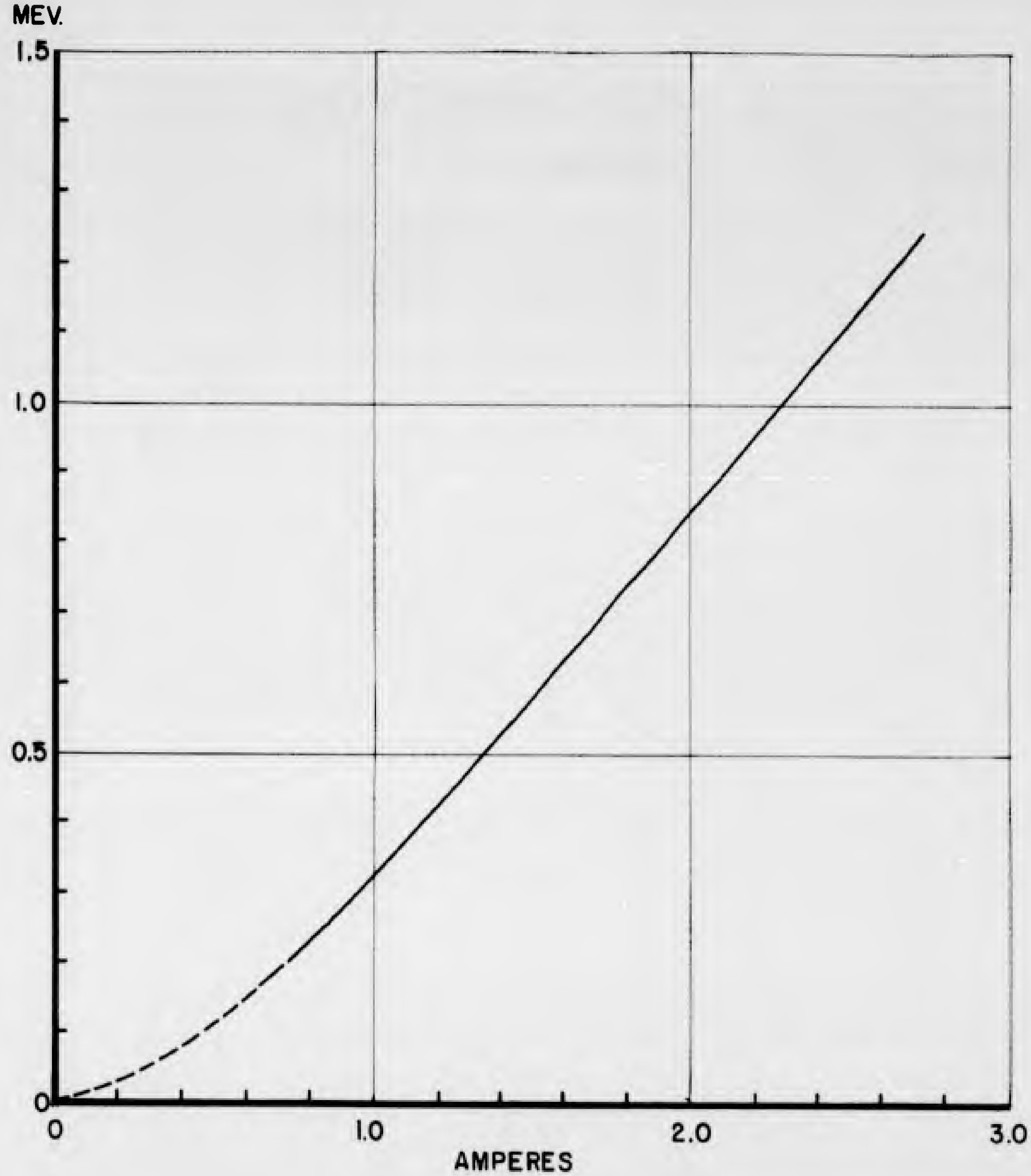

Figure 6.2 Calibration chart for electron energy selector magnet.

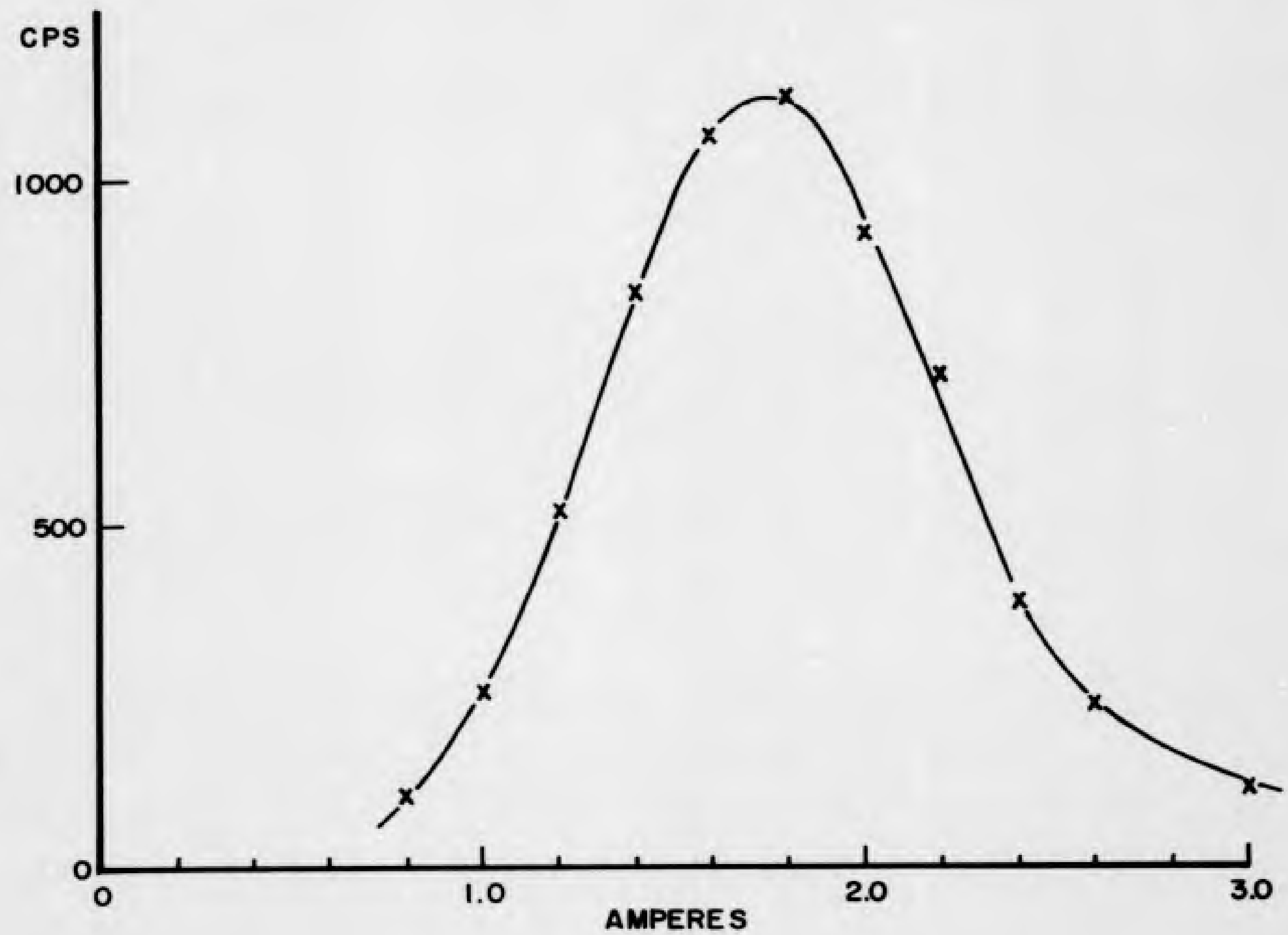

Figure 6.3 Y^{91} beta spectrum, 2 Dec 61.

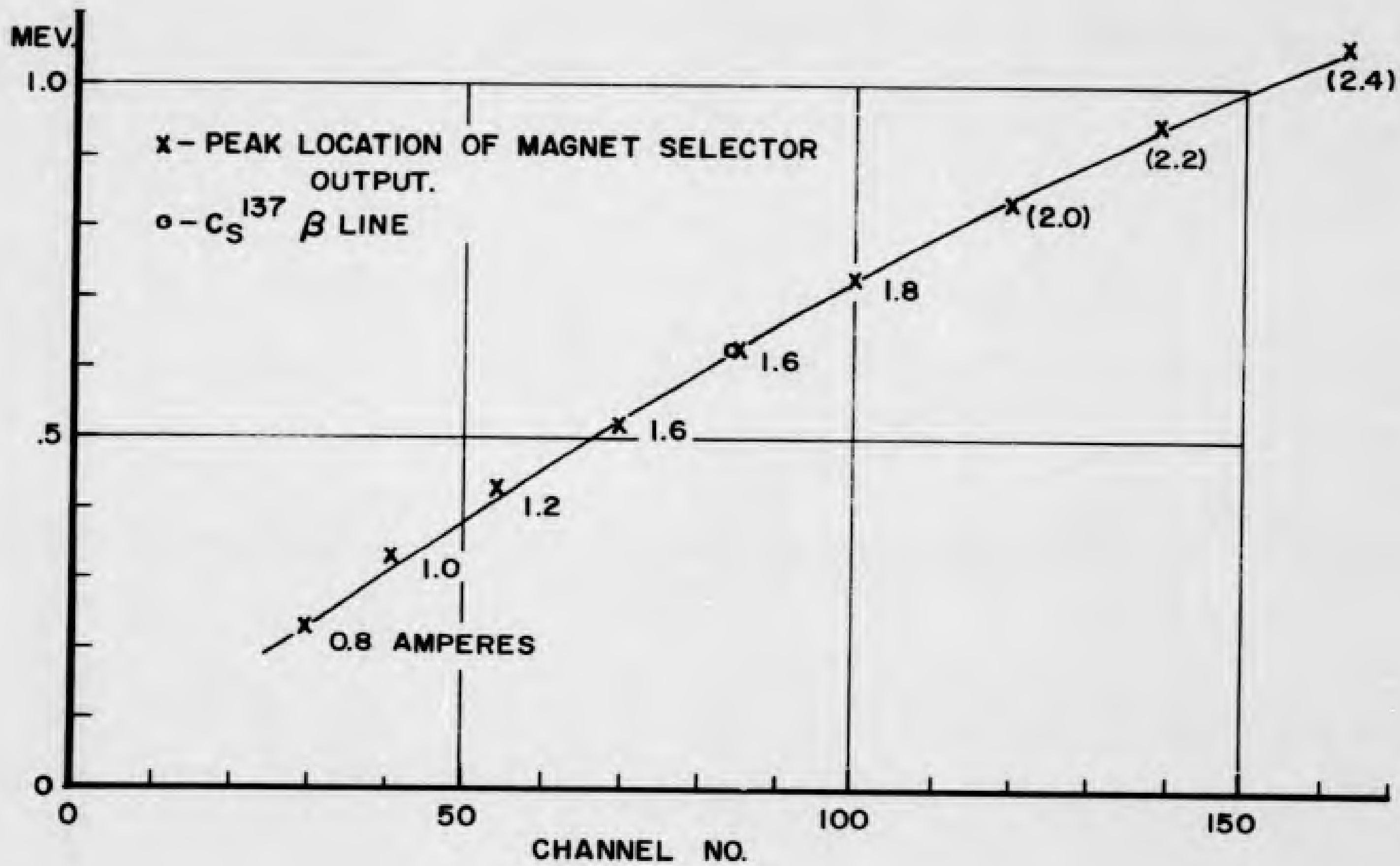

Figure 6.4 Magnet calibration using solid-state detector in combination with 256-channel analyzer.

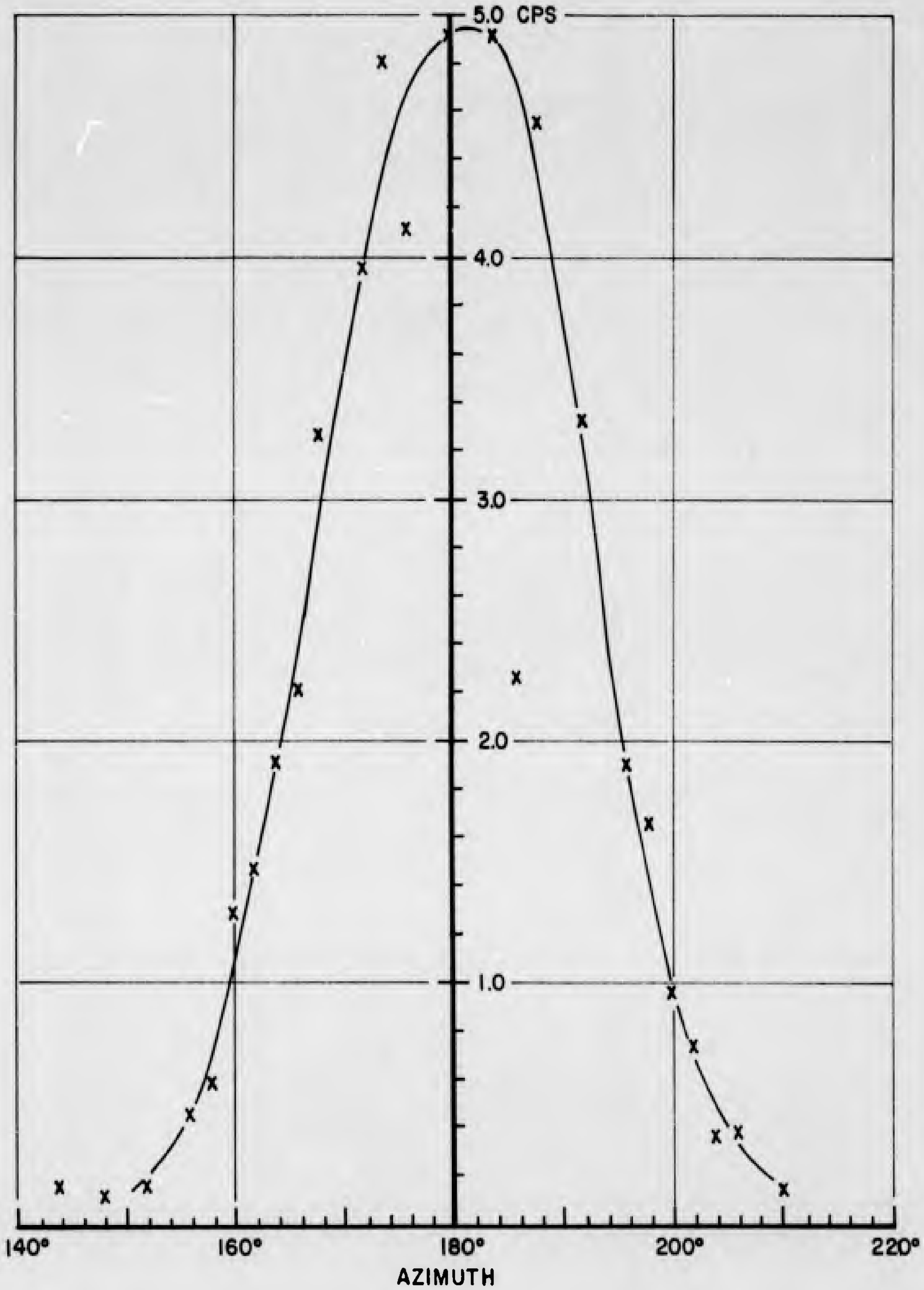

Figure 6.5 Detector A window characteristics, 0° inclination, 4.335 meters, 1.6 amperes, 25 Oct 61.

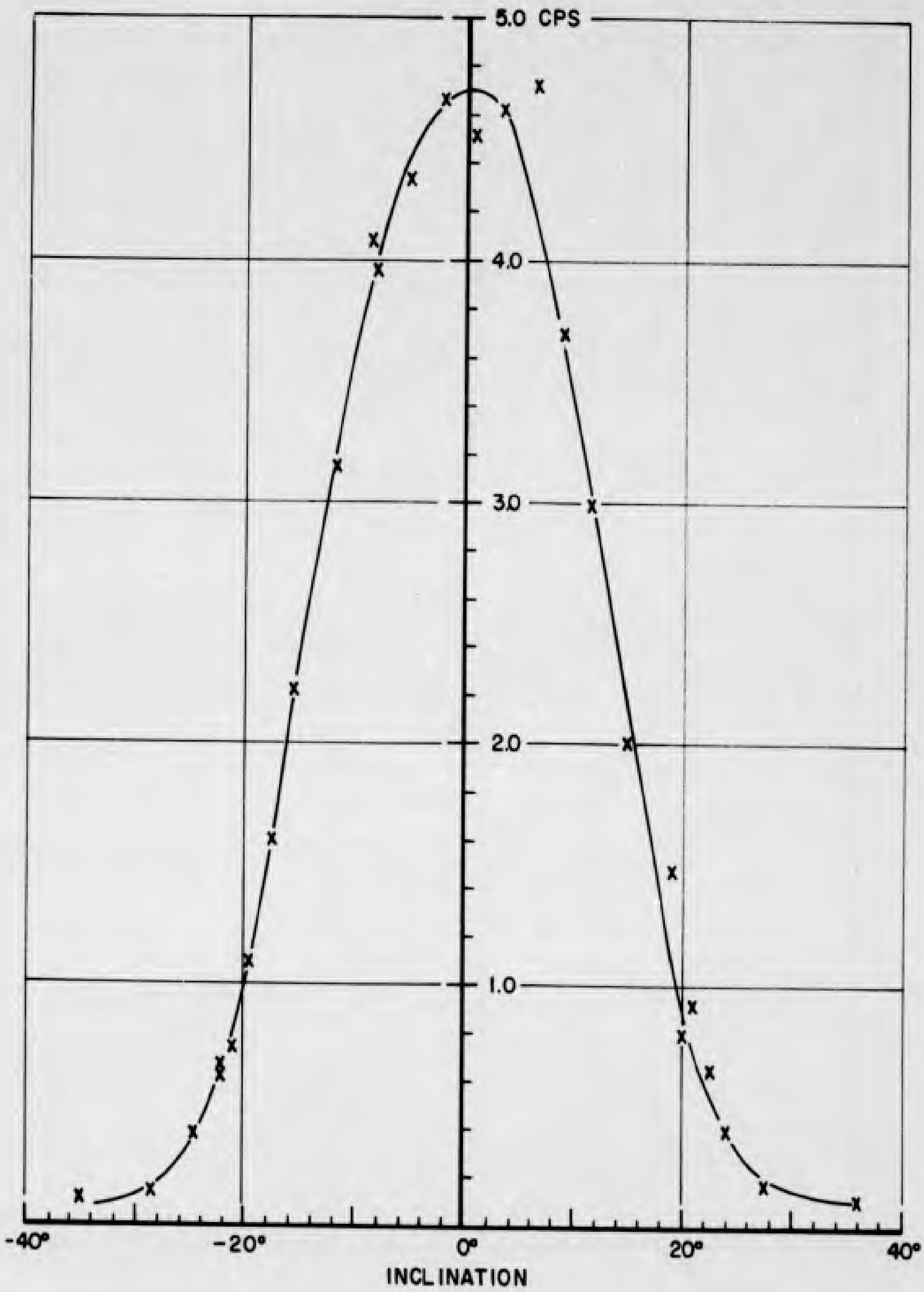

Figure 6.6 Detector A window characteristics, 180° azimuth, 4.335 meters, 1.6 amperes, 25 Oct 61.

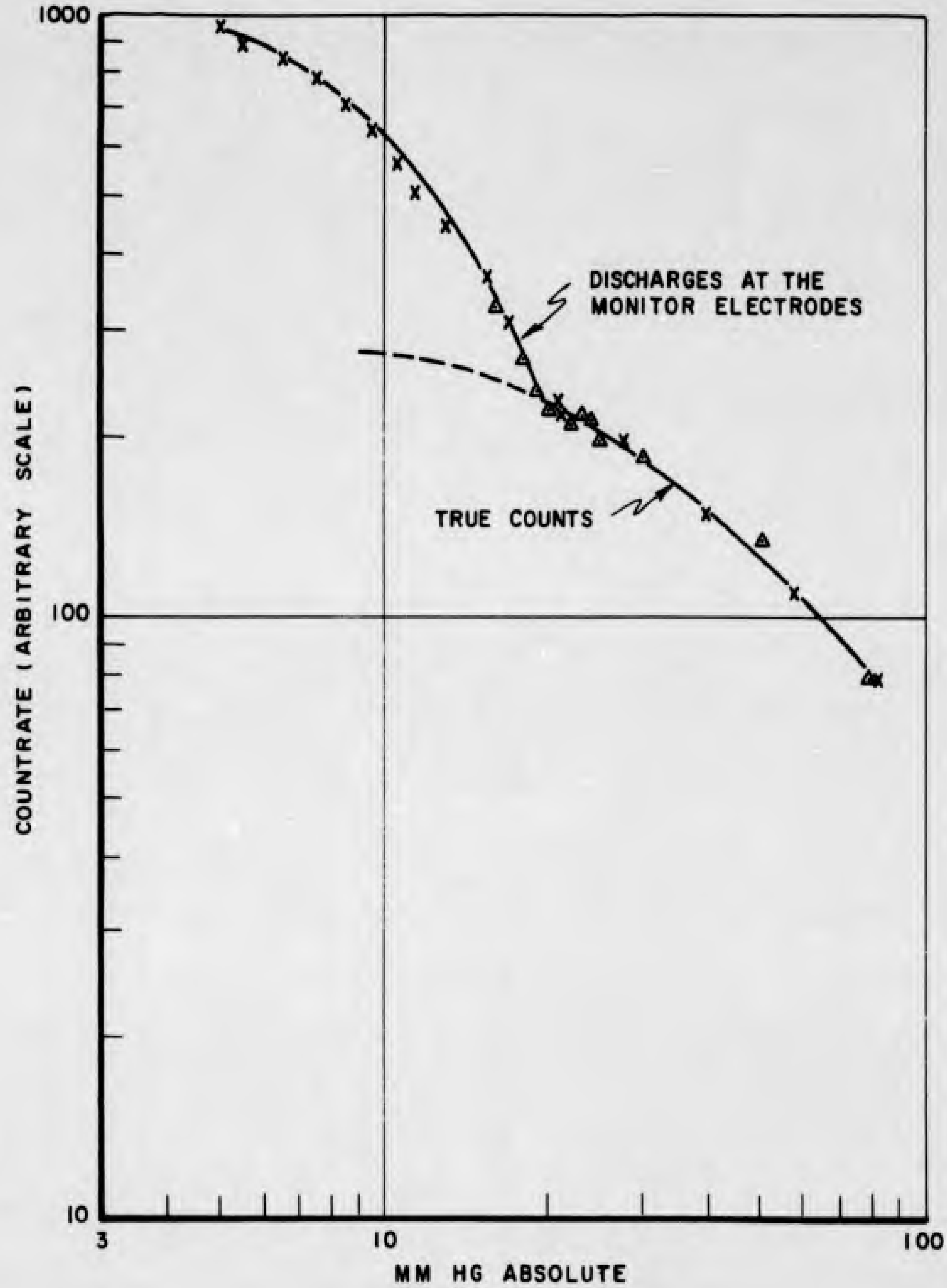

Figure 6.7 Count rate measured by monitor as a function of air pressure 2.725 meters from magnet.

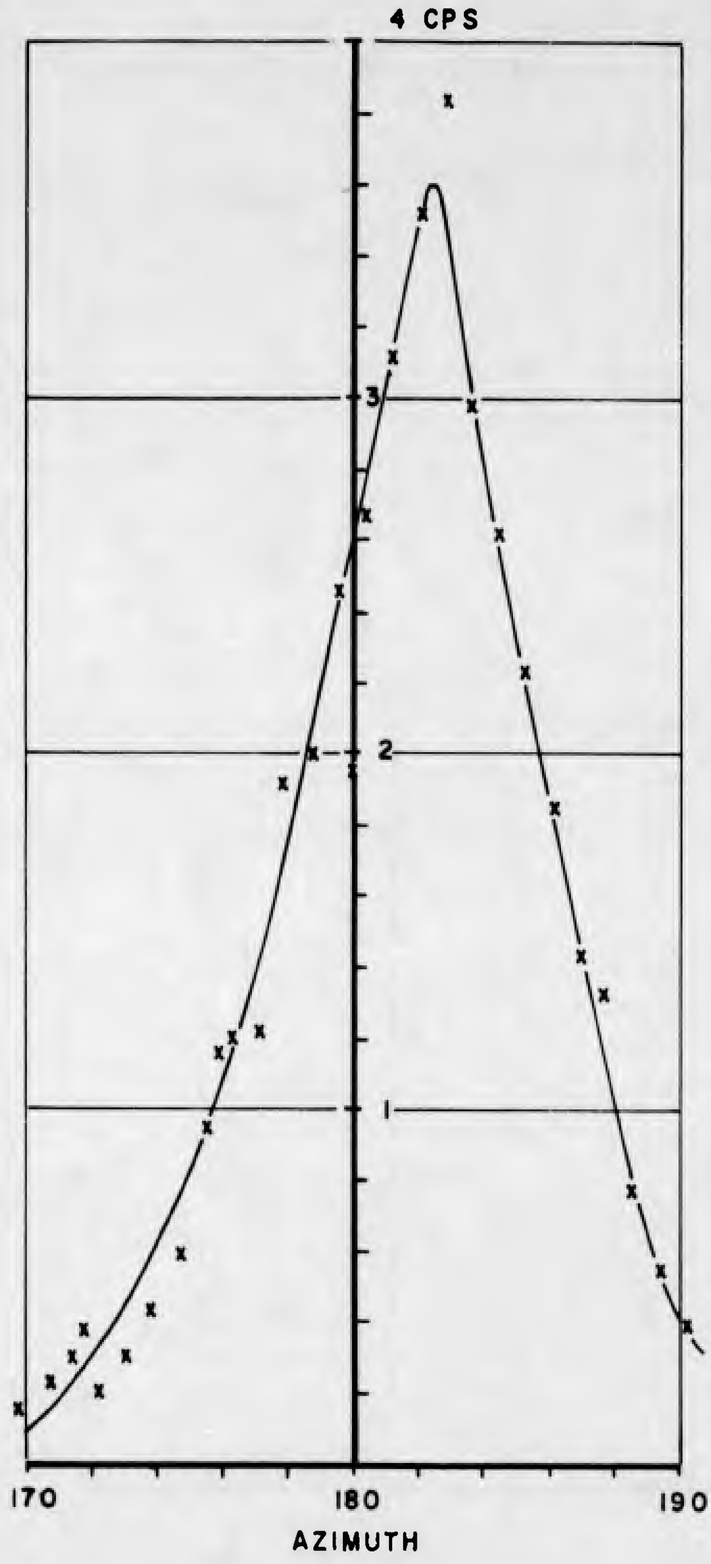

Figure 6.8 Electron scatter characteristics, Detector A with directional collimator, 0° inclination, 2.685 meters, 1.6 amperes, 30 Oct 61.

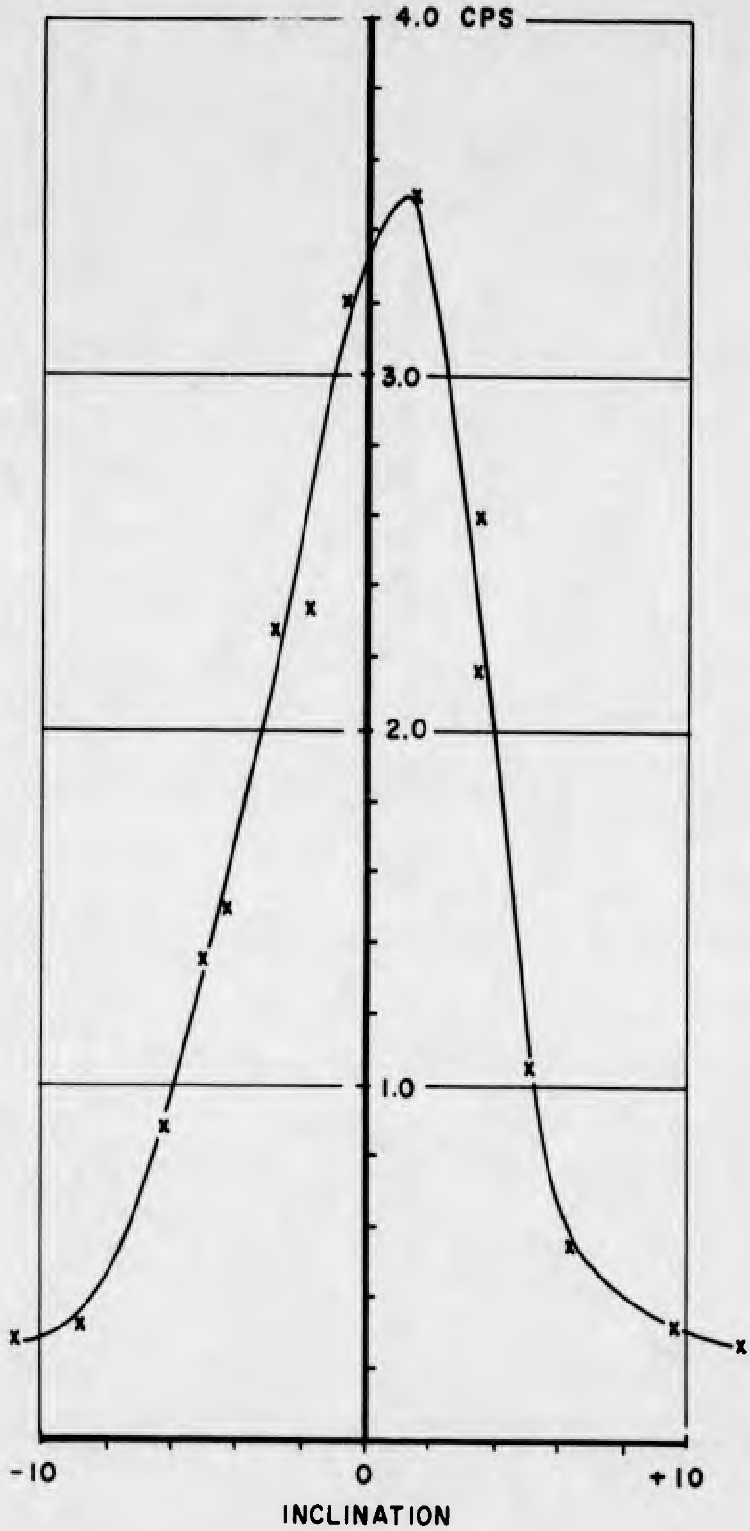

Figure 6.9 Electron scatter characteristics, Detector A with directional collimator, 180° aximuth, 2.685 meters, 1.6 amperes, 31 Oct 61.

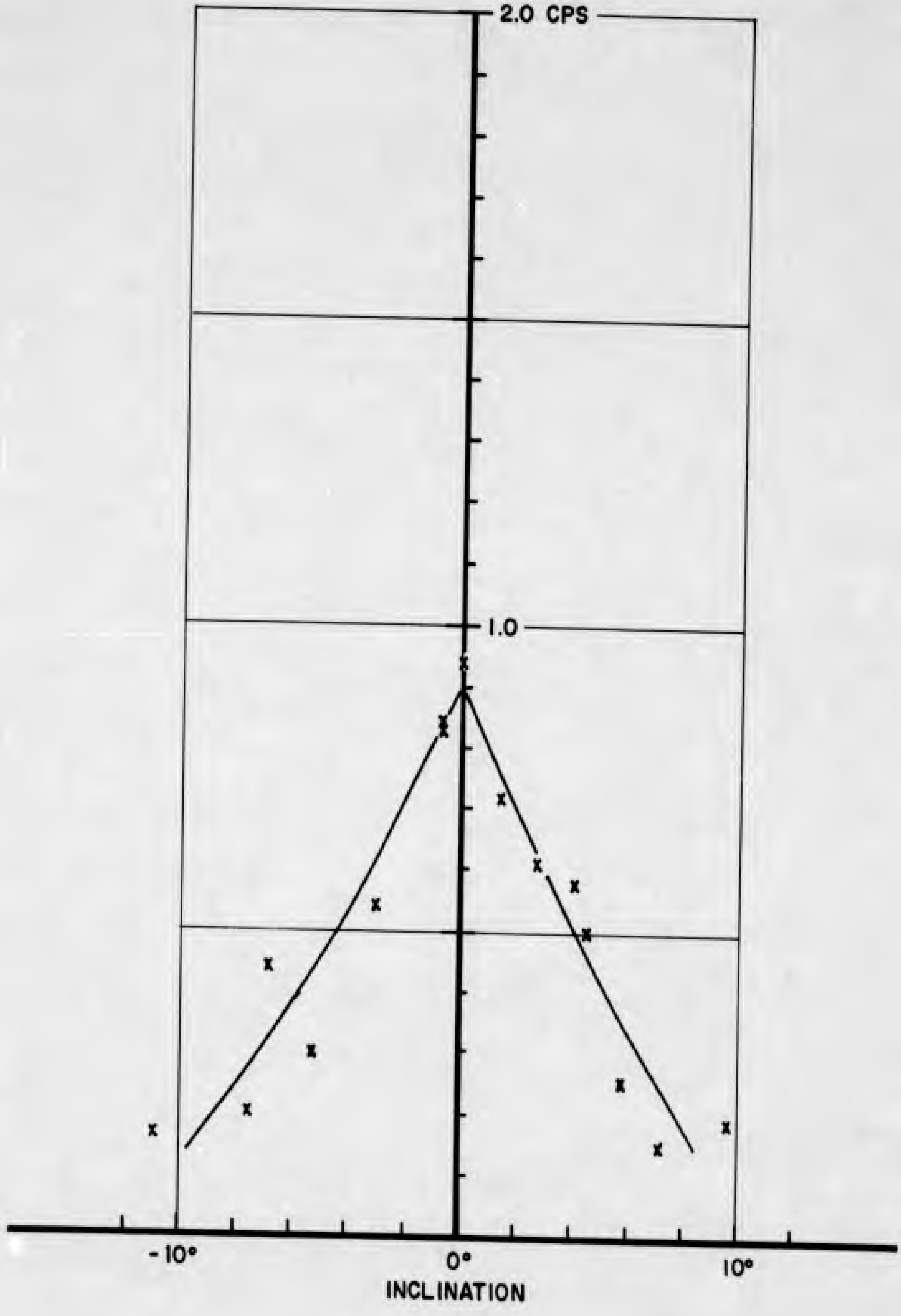

Figure 6.10 Electron scatter characteristics, Detector A with directional collimator, 180° azimuth, 2.685 meters, 2.4 amperes, 31 Oct 61.

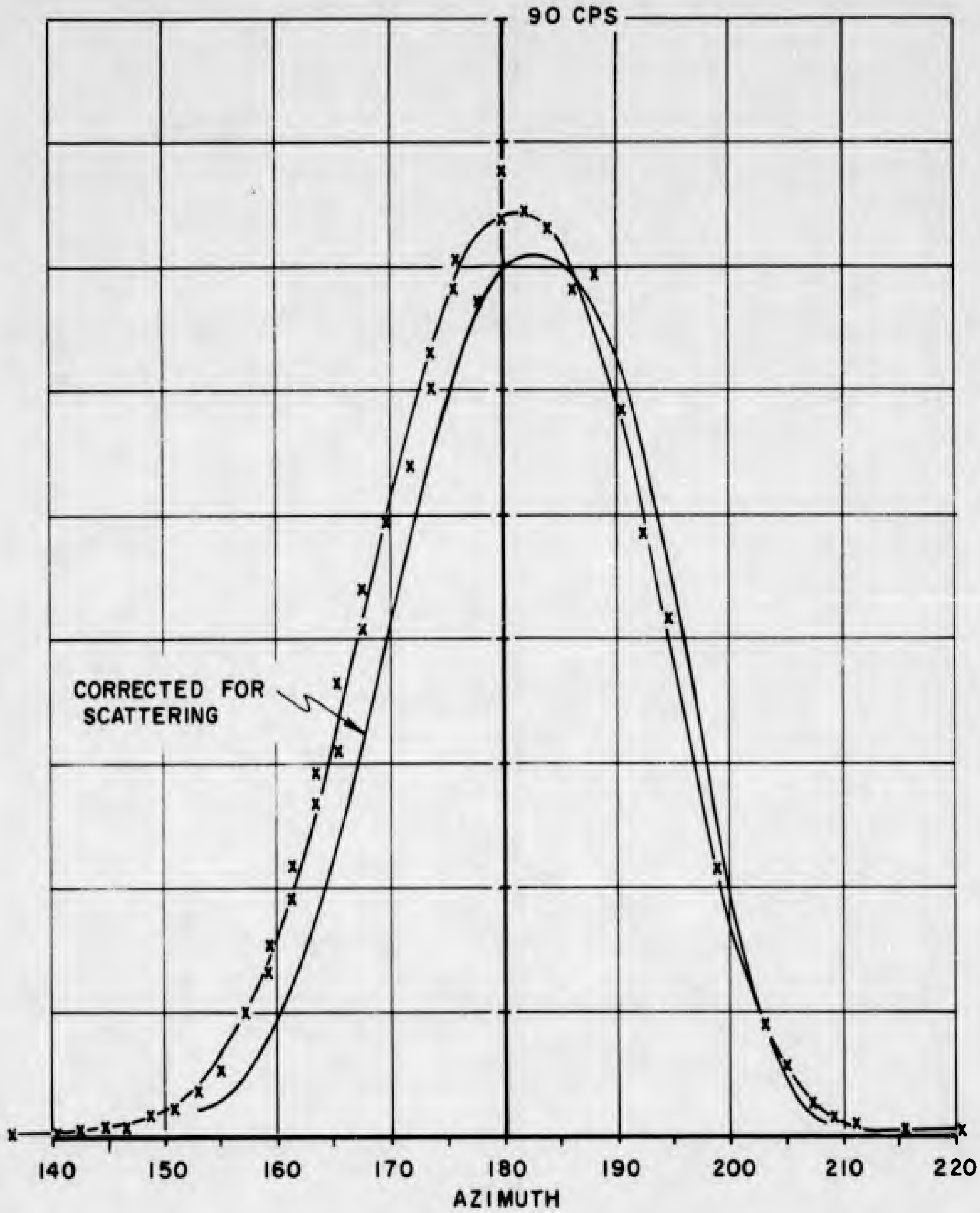

Figure 6.11 Detector A window characteristics corrected for scattering, 0° inclination, 2.685 meters, 1.6 amperes, 23 Oct 61.

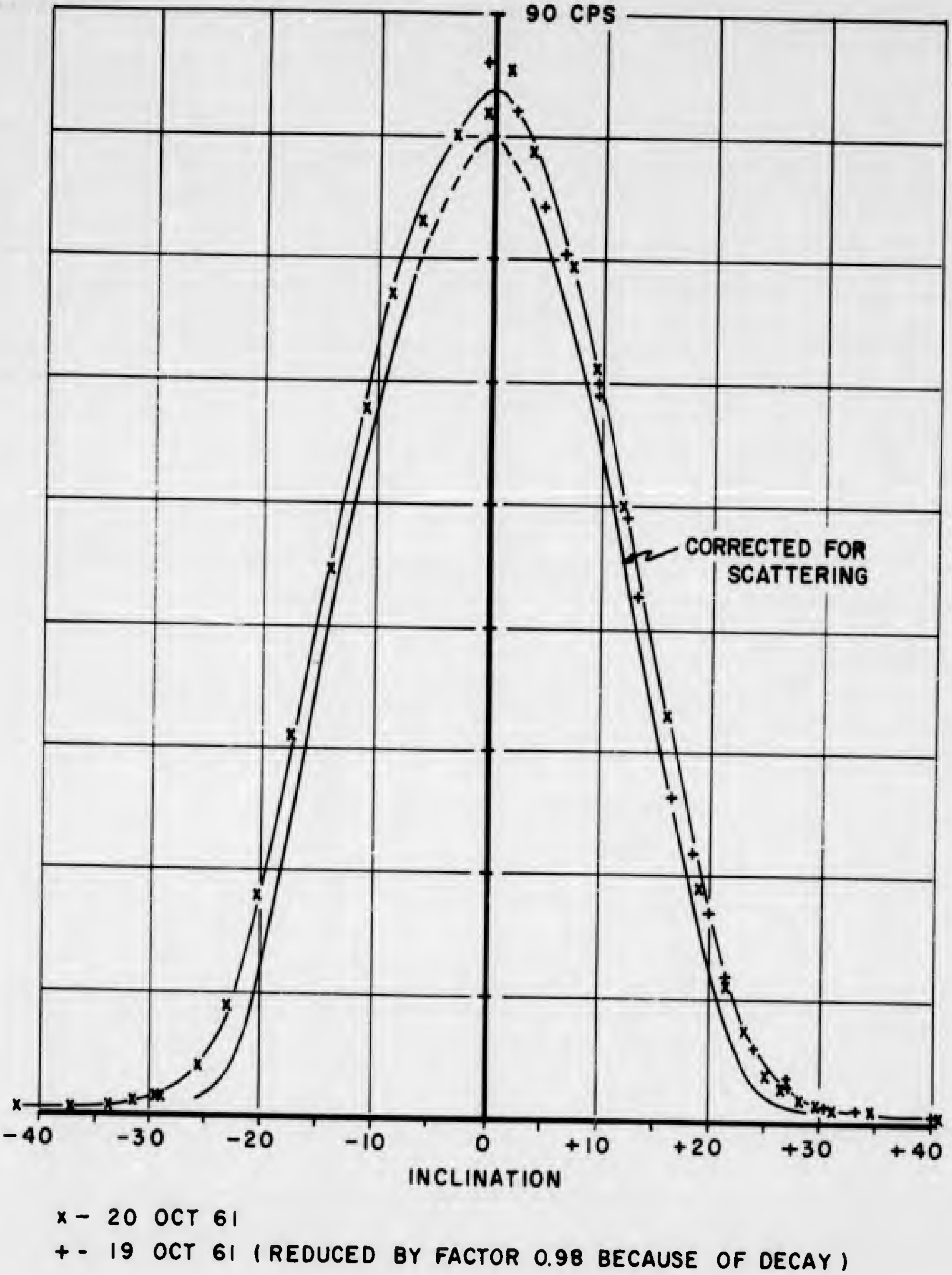

Figure 6.12 Detector A window characteristics corrected for scattering, 180° azimuth, 2.685 meters, 1.6 amperes.

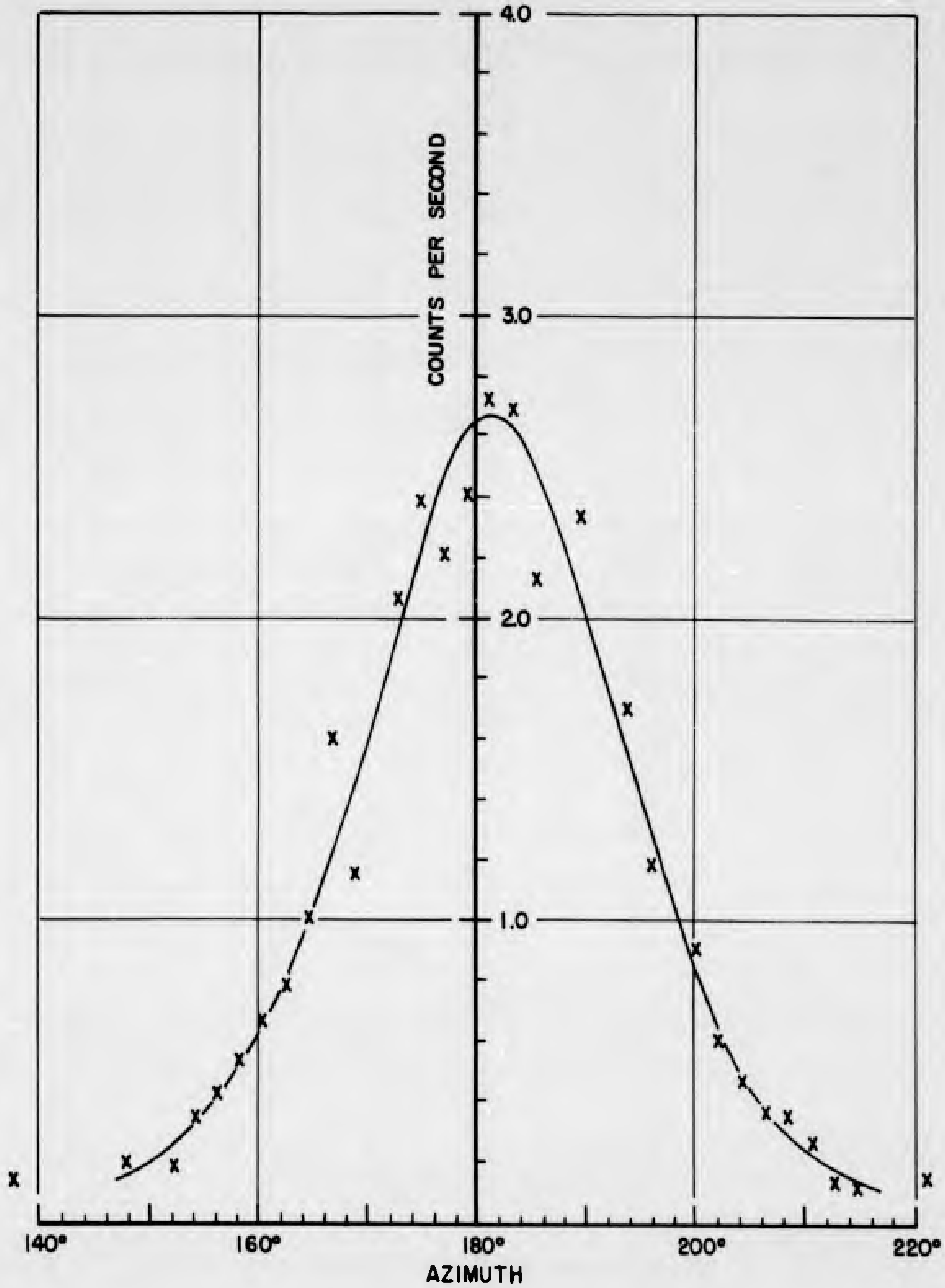

Figure 6.13 Detector A window characteristics, 0° inclination, 2.685 meters, 0.8 ampere, 23 Oct 61.

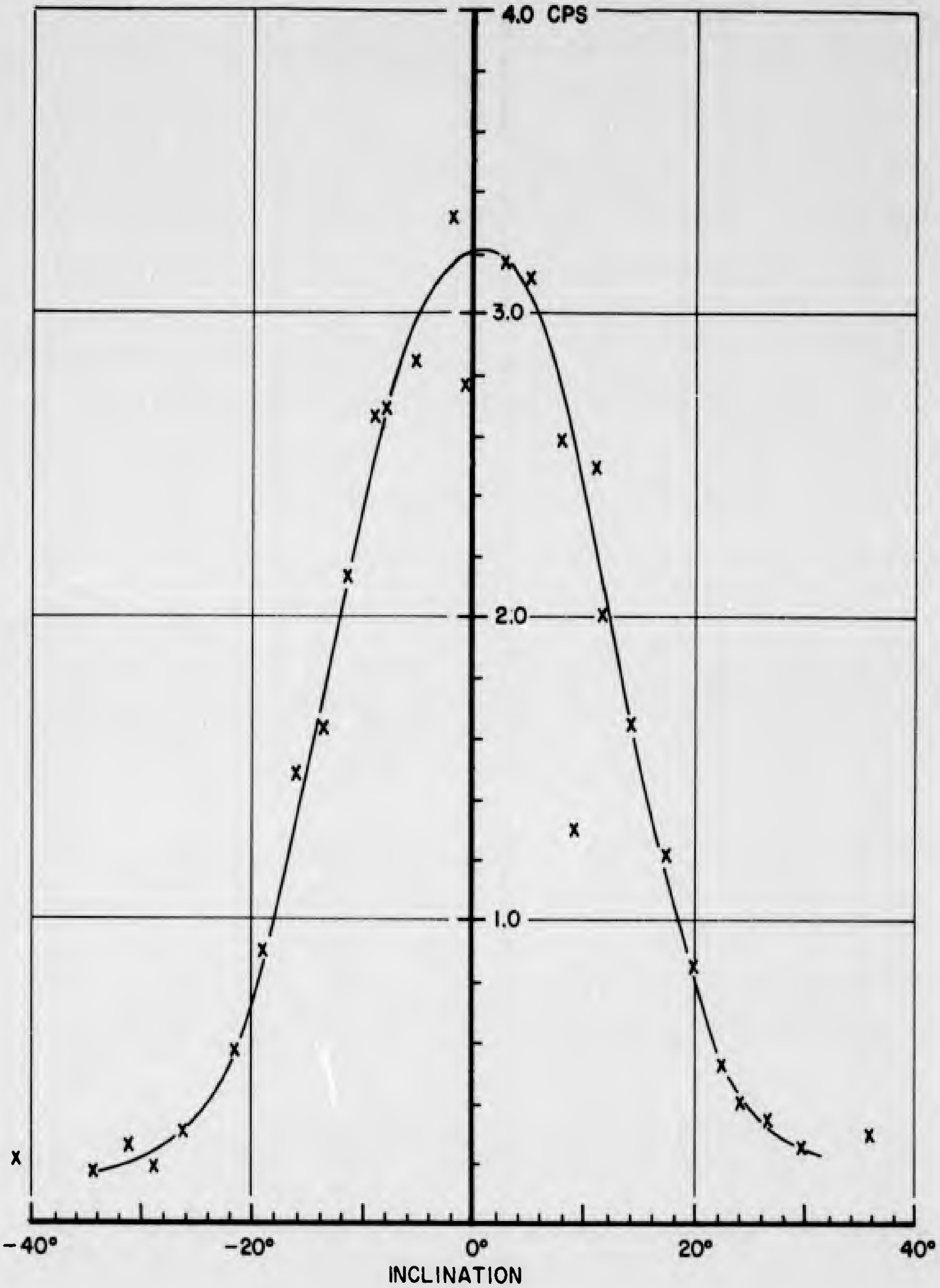

Figure 6.14 Detector A window characteristics, 180° azimuth, 2.685 meters, 0.8 ampere, 20 Oct 61.

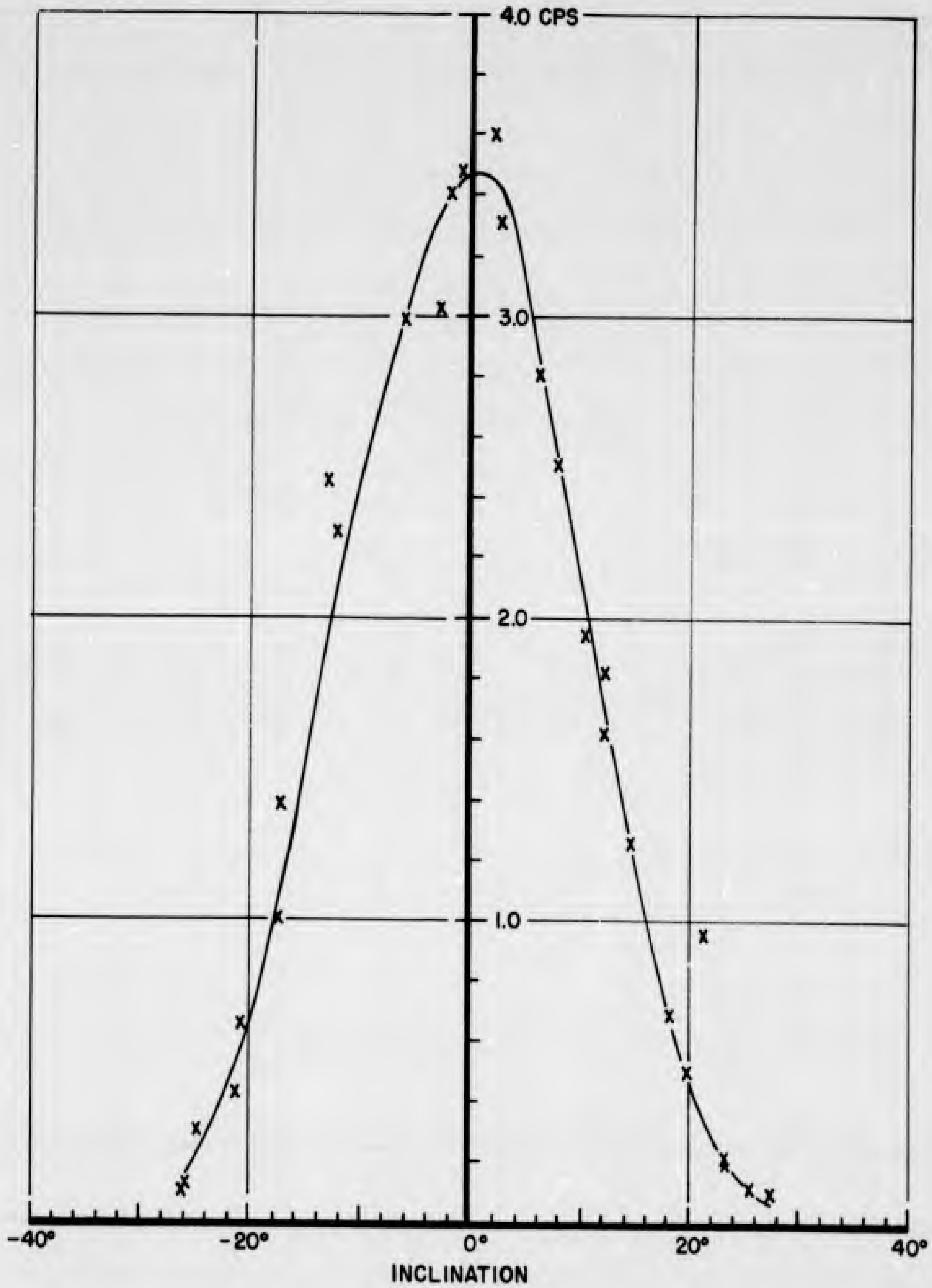

Figure 6.15 Detector A window characteristics with discriminator effective, 180° azimuth, 2.685 meters, 1.8 amperes, 25 Oct 61.

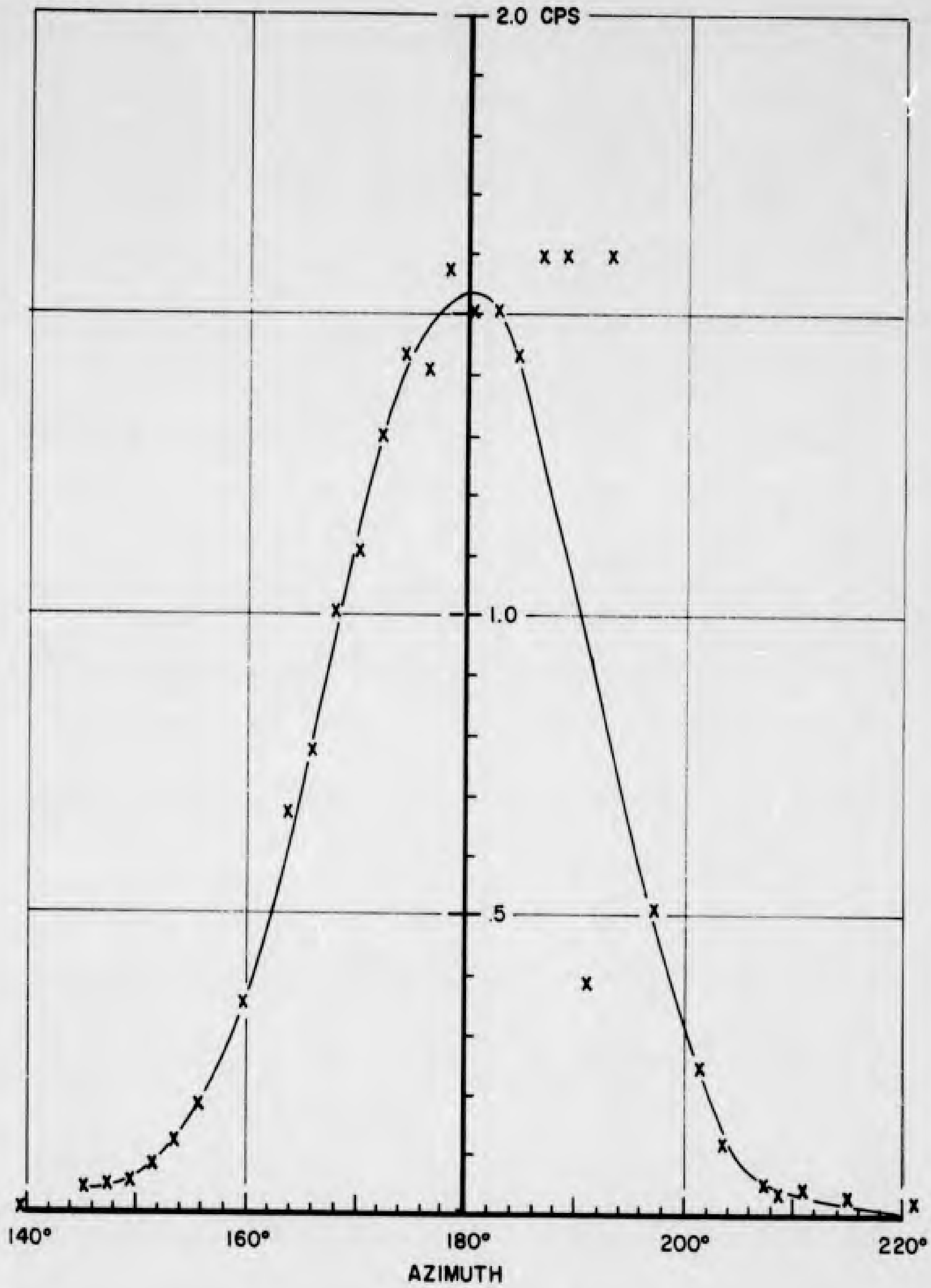

Figure 6.16 Detector A window characteristics, 0° inclination, 2.685 meters, 2.4 amperes, 24 Oct 61.

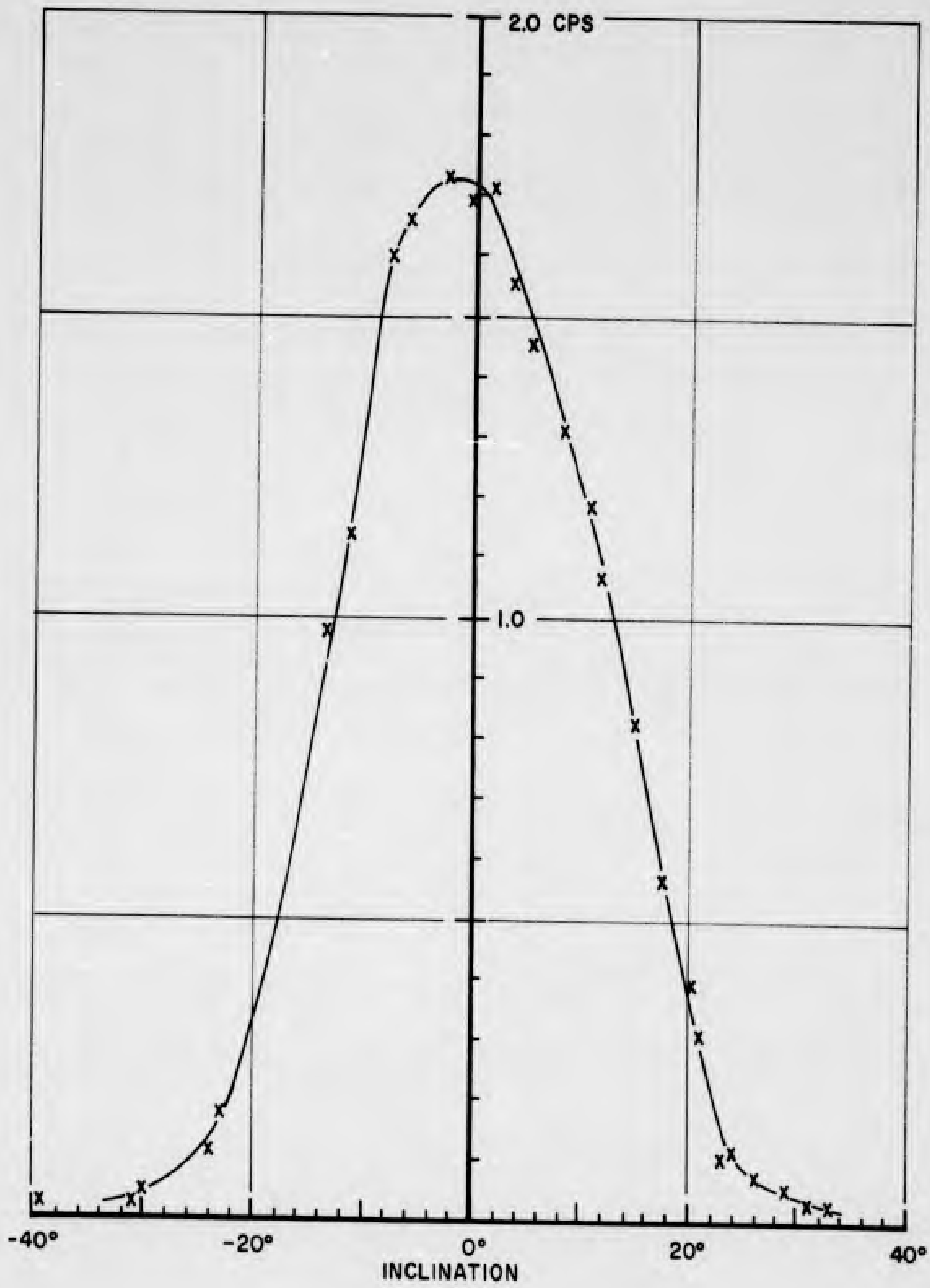

Figure 6.17 Detector A window characteristics, 180° azimuth, 2.685 meters, 2.4 amperes, 20 Oct 61.

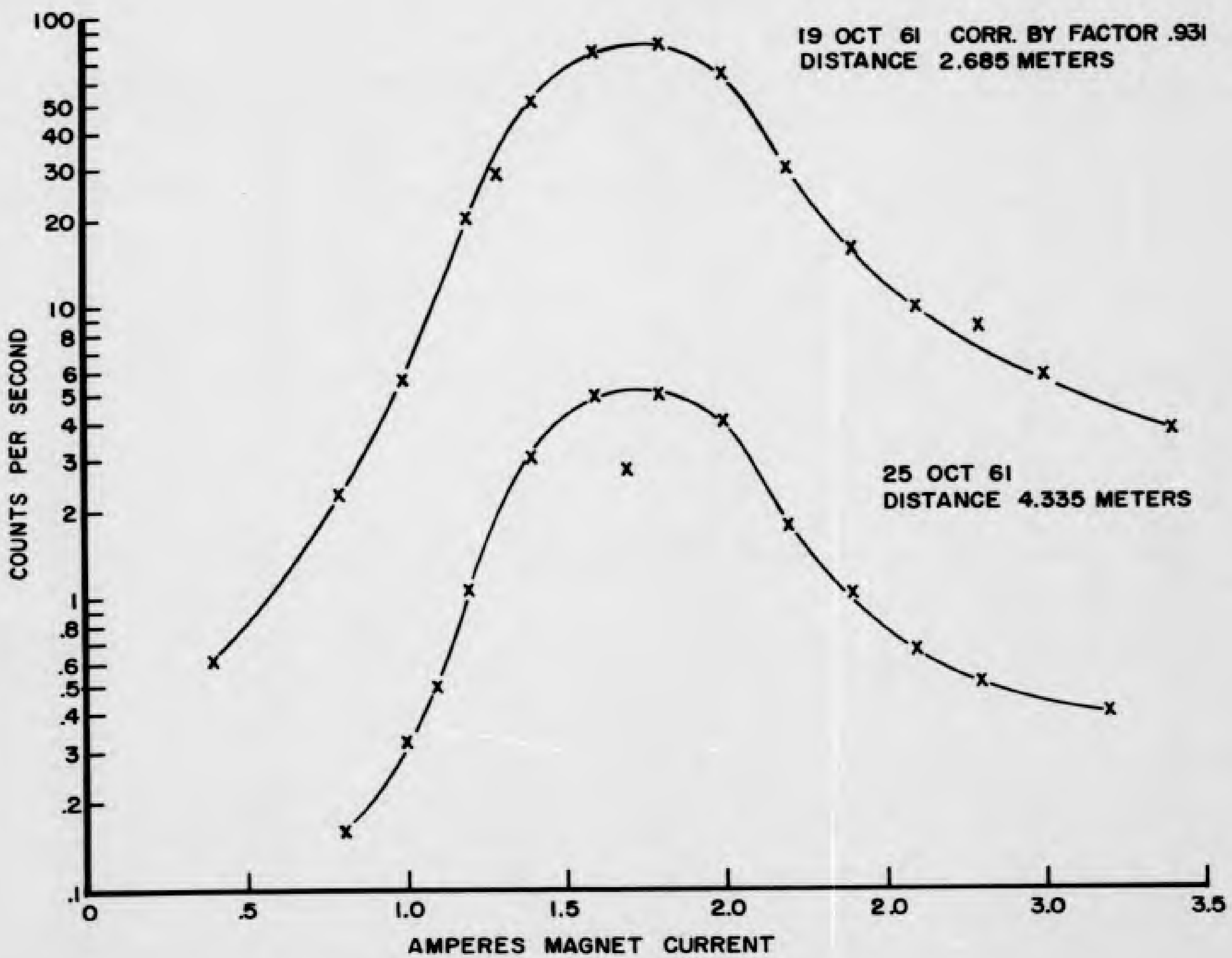

Figure 6.18 Y^{91} spectrum taken by Detector A at various distances from magnet.

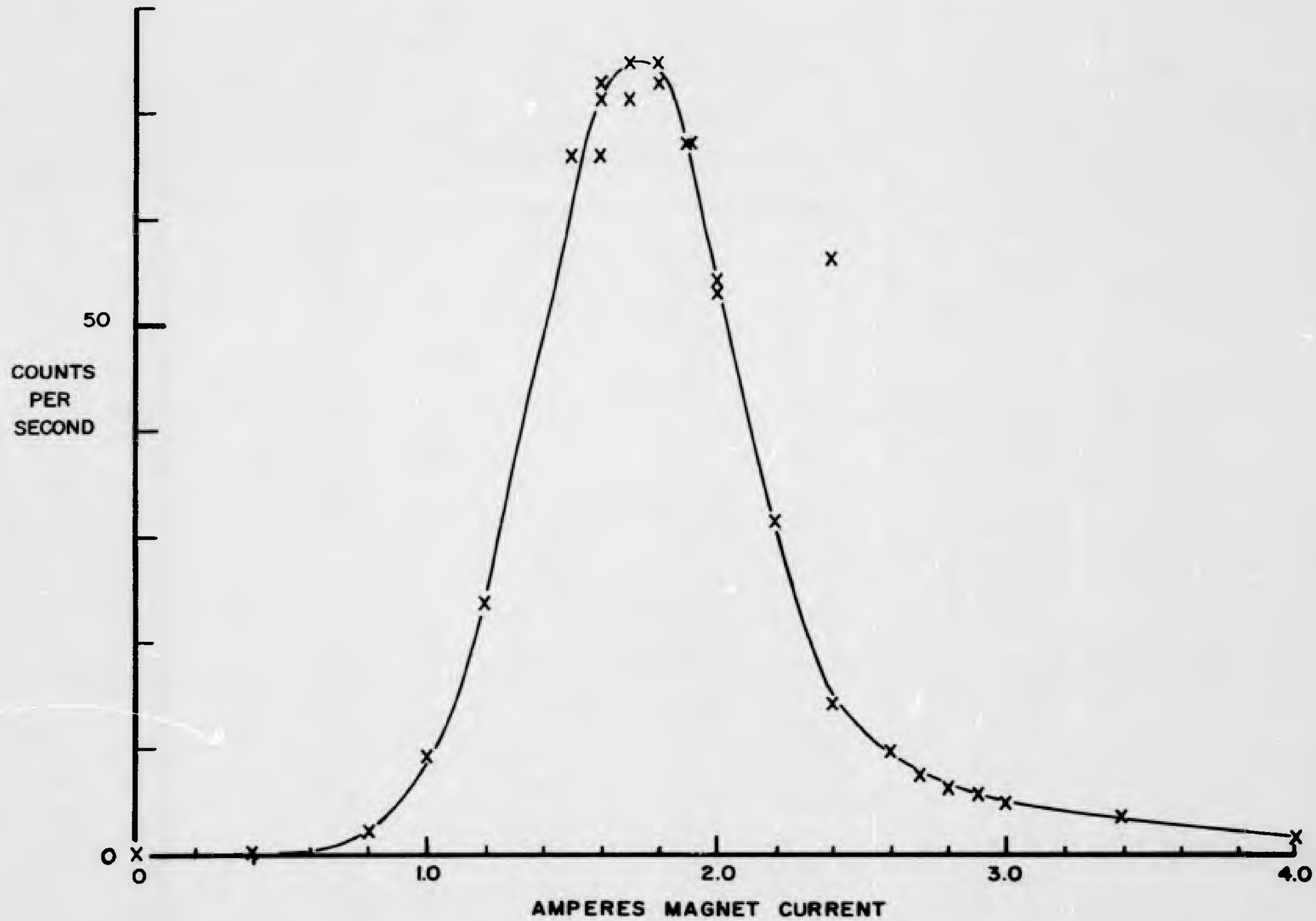

Figure 6.19 Y^{91} electron spectrum as analyzed by 90° deflection magnet (monitored by Detector A), 2.685 meters, 24 Oct 61.

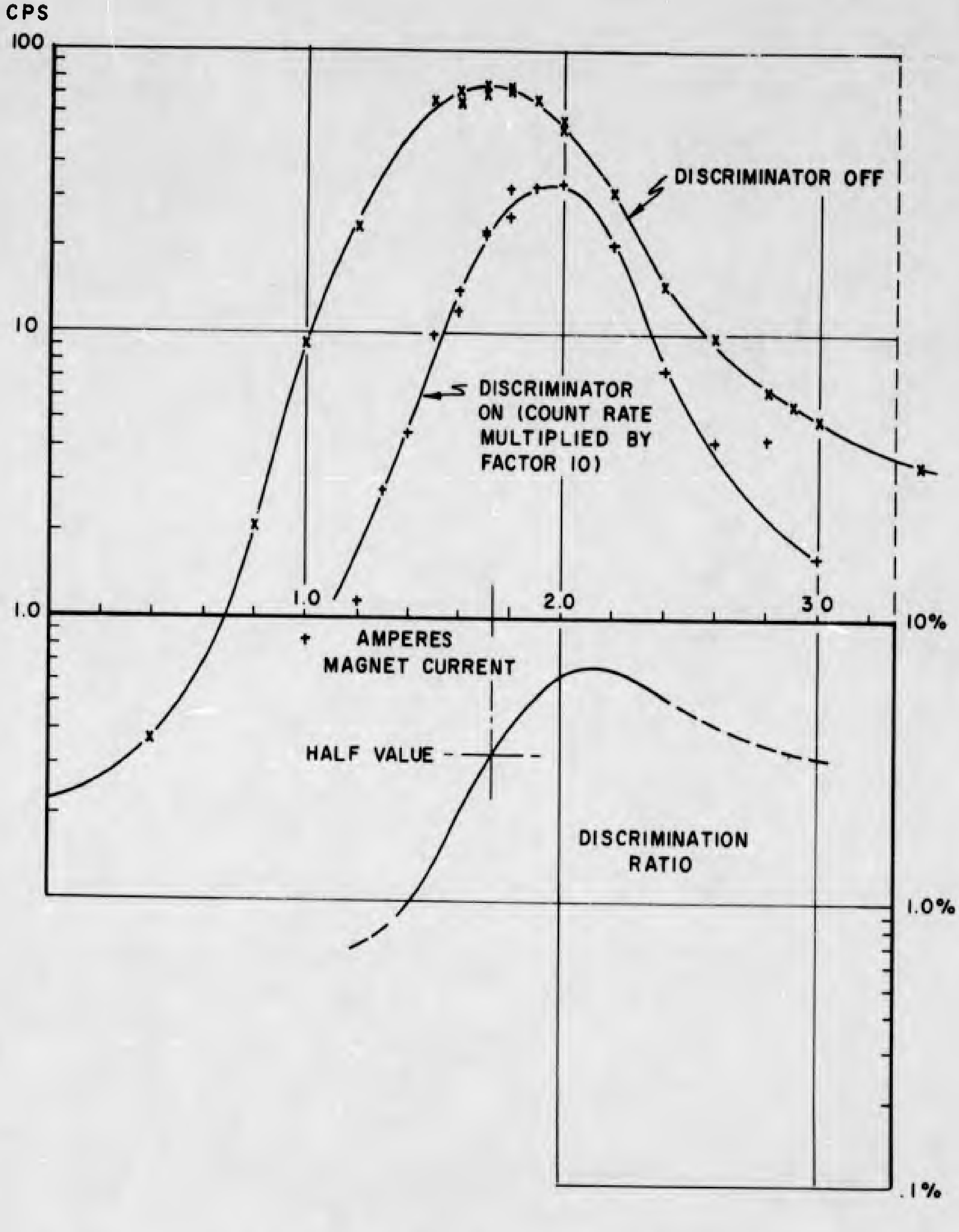

Figure 6.20 Response of Detector A to analyzed Y^{91} spectrum, 2.685 meters.

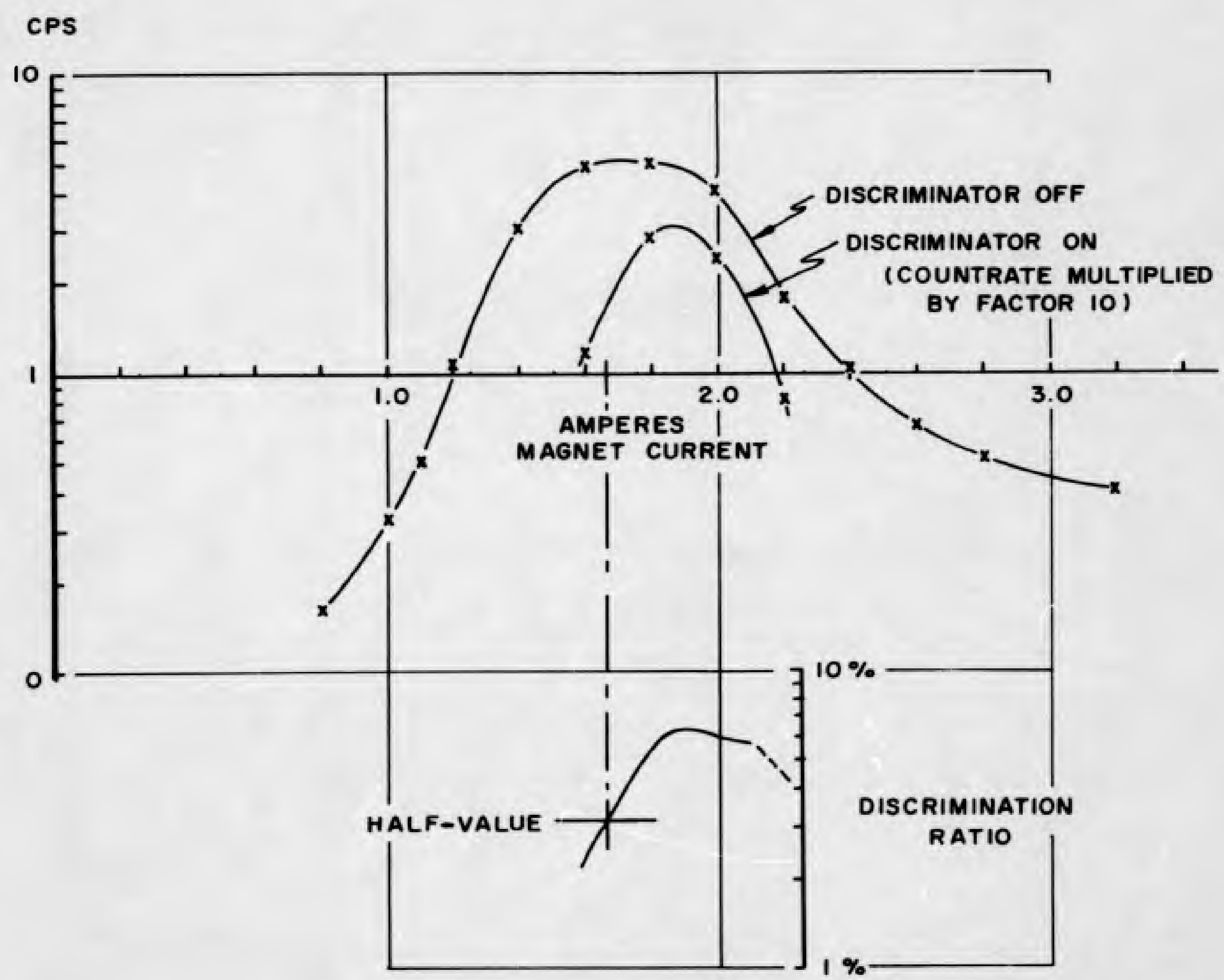

Figure 6.21 Response of Detector A to analyzed Y^{91} spectrum, 4.335 meters, 25 and 26 Oct 61.

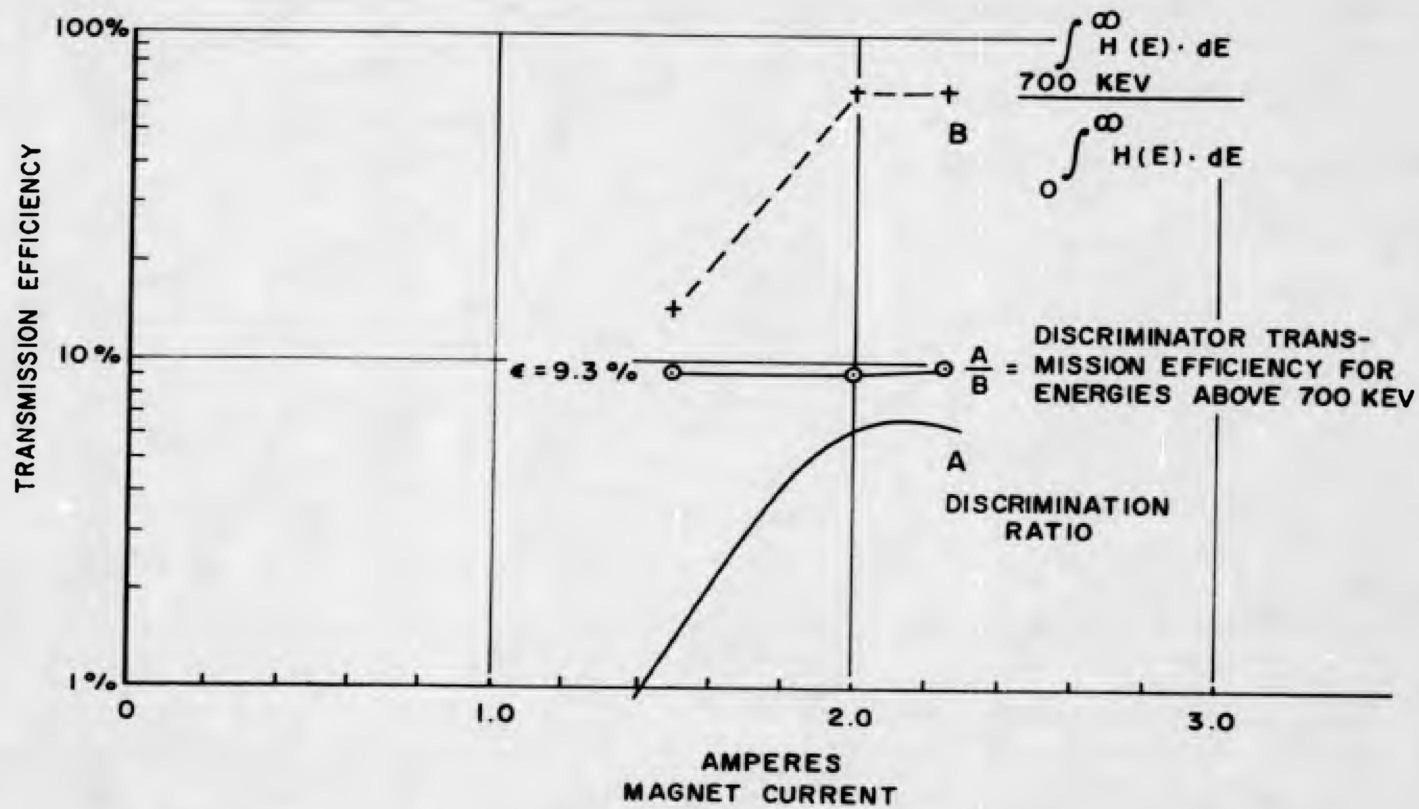

Figure 6.22 Comparison of integral spectrum ratio with discrimination ratio from Figure 6.20.

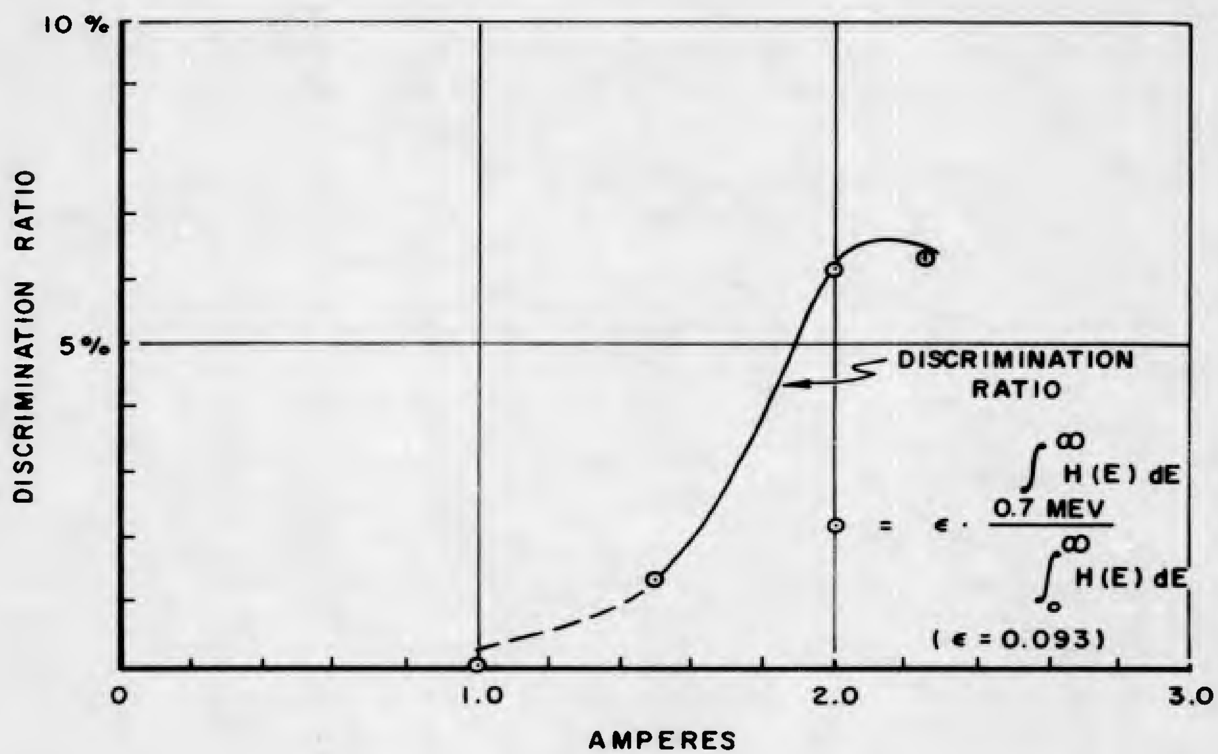

Figure 6.23 Comparison of measured discrimination ratio and normalized integral spectrum ratio.

CHAPTER 7

DERIVED DATA

The calibration data presented can be used in a variety of ways to obtain derived data necessary for interpretation of the count rate data from the Explorer IV flight package. For absolute measurements, one of the useful parameters that can be derived is the effective area, A_{eff}. Other derived useful parameters are the energy thresholds for the GM detectors, the omnidirectional effective area for Detector C, and the count ratios of the shielded and unshielded GM detectors averaged over direction as a function of energy for photons.

7.1 EFFECTIVE AREAS

For absolute measurements, A_{eff} has to be known. The effective area is the effective acceptance area of any detector, assuming that the detector efficiency is 100 percent. Thus,

$$A_{eff} = A_{eff}(E, I, \varphi, \theta)$$

E = energy
I = intensity
φ = azimuth
θ = inclination

for each type of radiation. This is valid for a parallel homogeneous radiation beam. For isotropic radiation,

$$A_{eff} = A_{eff}(E, I) = \int_{0^\circ}^{360^\circ} \int_{-90^\circ}^{+90^\circ} A_{eff}(E, I, \varphi, \theta)\, d\theta \cdot d\varphi \qquad (7.1)$$

Because there is a linear relationship between intensity I and recorded count rates, A_{eff} is dependent only on I until saturation is reached. Thus, for lower count rates,

$$N = I \cdot A_{eff}(E, \varphi, \theta) \text{ where } N = \text{count rate} \qquad (7.2)$$

introducing a dead-time correction for higher count rates. The latter equation can be used for determination of the effective area from the calibration measurements on photons, in the form

$$A_{eff}(E, \varphi, \theta) = \frac{N}{I} \qquad (7.3)$$

since N is recorded and I is known. For the saturation experiments,

$$A_{eff}(E, \varphi, \theta) = \frac{N}{\xi I}$$

where ζ is the dead-time correction function. In the case of electron calibration for Detector A, Equation 7.2 can be split into two components so that

$$A_{eff}(E, \varphi, \theta) = A_{eff}(E) \cdot \alpha(\varphi, \theta) \tag{7.4}$$

where $A_{eff}(E)$ is the effective area pointing at azimuth 180° and inclination 0°, where the detector window has the highest response. Thus, $\alpha(\varphi, \theta)$ is a dimensionless angular response function obtained by normalizing the experimental data as

$$\alpha(\varphi, \theta) = \frac{N(\varphi, \theta)}{N(180°, 0°)} \tag{7.5}$$

7.2 EFFECTIVE AREAS OF DETECTOR A

The effective area of Detector A (plastic scintillator) for betas was measured by comparing the Detector A recording with the absolute electron flux measurement made with a gold-surface-barrier solid-state detector under identical geometrical conditions (Figure 7.1). Thus,

$$A_{eff} = \frac{N_{satellite}(B)}{N_{solid\ state}(B)} \cdot A_S \text{ (area of solid-state detector = 64 mm}^2\text{)} \tag{7.6}$$

Since the discriminator was bypassed during the measurement, the measured effective area A'_{eff} must be multiplied by the discriminator transmission efficiency ϵ (Equation 6.10) to obtain true values of effective area as:

$$A_{eff} = \epsilon A'_{eff} \tag{7.7}$$

$$A_{eff} = (0.088 \pm 0.001) \cdot (0.093 \pm 0.003) \cdot A_S (= 64 \text{ mm}^2)$$

$$A_{eff} = 0 \text{ for } E < 700 \text{ kev}$$

$$A_{eff} = 0.52 \pm 0.02 \text{ mm}^2 \text{ for } E > 700 \text{ kev} \tag{7.8}$$

The omnidirectional effective area, $\bar{\bar{A}}_{eff}$, was determined according to Equation 7.11 from Co^{60} data and expressed as

$$\bar{A}_{eff} = \frac{\bar{\bar{N}}}{I} \tag{7.9}$$

where $\bar{\bar{N}}$ is the count rate averaged over the entire sphere, I is the photon flux density as derived from data on the GM tubes (Detectors C and D) in Section 7.3. Thus, for the average photon energy of 1.25 Mev,

$$A_{eff} = \frac{1.230}{1955} = (6.29) \times 10^{-4} \text{ cm}^2 = (6.29)\, 10^{-2} \text{ mm}^2 \tag{7.10}$$

7.3 EFFECTIVE AREAS FOR GAMMAS, DETECTORS C AND D

The effective area of the GM tubes at various energies has been obtained by averaging the count rates of Figures 4.2 through 4.5 over azimuthal intervals from 0 to 360°. For this purpose the entire sphere was cut into five latitudinal zones of 30° each, corresponding to fixed inclination settings, plus two polar caps of 15° radius. The overall count rate was found by a summation expressed as

$$\bar{\bar{N}} = \sum_i \xi_i \cdot \bar{N}_i \tag{7.11}$$

where

$$\xi_i = \frac{A_i}{4\pi} \tag{7.12}$$

$\bar{N}_i$ = count rate averaged over 360° azimuth for each latitudinal zone

A_i = area of each zone on the unit sphere

The count rates at the south polar cap were estimated by extrapolation, but since the contribution from this portion of the spherical area was very small (ξ_i = 1.7 percent), the probable error should be less than 1 percent.

According to Equation 7.9 the photon flux or intensity I has to be known. For the Cs^{137} the dose measured at 20-cm distance was 16.61 mr/min. The dose at the shell distance (distance = 443.5 cm) therefore was 56.25×10^{-8} r/sec. (7.13)
Using the photon flux per roentgen at the energy of 0.66 Mev, the authors obtain

$$\frac{I}{r} = 27.10 \times 10^8 \text{ photons/roentgen cm}^2 \tag{7.14}$$

and

$$I = 1525 \text{ photons/sec cm}^2 \tag{7.15}$$

Using the averaged count rate $\bar{\bar{N}}$, the authors obtain the effective areas for 0.66 Mev as follows:

Energy	Detector Type	Count Rate $\bar{\bar{N}}$	A_{eff}
		cps	mm^2
0.662 Mev	Detector C (Unshielded)	10.7	0.702
	Detector D (Shielded)	5.79	0.379

The effective area for the average energy of Co^{60} of 1.25 Mev (1.17 + 1.33 Mev) was obtained in the same manner. The Co^{60} source produced a dose of 36.53 mr/min at 20-cm distance. The conversion from roentgens at 1.25 Mev to photons is 15.81×10^8 photons/roentgen cm^2. Thus, the photon flux at the shell was 1955 photons/cm^2 sec. Using this information, the authors obtained the following:

Energy	Detector Type	Count Rate $\bar{\bar{N}}$	Effective Area A_{eff}
		cps	mm^2
1.17 + 1.33 Mev	Detector C (Unshielded)	19.75	1.010
	Detector D (Shielded)	15.47	0.791

7.4 EFFECTIVE AREAS FOR X-RAYS, DETECTORS C AND D

Calculation of effective area as a function of energy for X-rays is not as direct as that for gamma rays, because the former are not monochromatic. The count rates were averaged over the end point energy range from 70 to 120 kev. The photon flux intensity was referred to 60 kev, because it is evident from Figure 5.2 that a maximum photonic flux is produced per roentgen at this energy, which is

$$\frac{I}{r} = (300)\ 10^8 \text{ photons/r}\cdot\text{cm}^2 \tag{7.16}$$

This maximum flux point lies within the bremsstrahlung spectra for each energy over the range from 70 to 120 kev.

The dose rates referred to the end point energies or voltage settings of the X-ray machine are listed in the following table.

Energy, kev	70	80	90	100	110	120
mr/min	22.8	31.6	40.0	48.8	57.6	65.6
mr/sec	0.380	0.527	0.667	0.813	0.960	1.092
10^6 photons/ sec cm^2	11.4	15.8	20.0	24.4	28.8	32.8

Listing the measured count rates of Detector C and forming the ratio of count rate to intensity, the authors obtained the effective areas:

Energy, kev	70	80	90	100	110	120
Counts/sec	568	978	1262	1550	1920	2200*
A_{eff}, 10^{-4} mm^2	50	62.0	63.0	63.5	66.7	67.0

* Obtained by linear extrapolation.

The above-listed effective areas refer to position $\varphi = 180°$, $\theta = 0°$

i.e., $$A_{eff} = A_{eff}(180°, 0°) \tag{7.17}$$

The omnidirectional effective area has been found by a count rate transformation by the establishment of the following matrix as a function of energy.

$$S_{14} = \frac{N(180°\,;0°)}{\overline{\overline{N}}} \quad ; \quad S_{24} = \frac{\overline{N}(180° - 360°)}{\overline{\overline{N}}} \quad ; \quad S_{34} = \frac{\overline{N}}{\overline{\overline{N}}}$$

$$S_{13} = \frac{N(180°;\ 0°)}{\overline{N}} \quad ; \quad S_{23} = \frac{N(180° - 360°)}{\overline{N}}$$

$$S_{12} = \frac{N(180°;\ 0°)}{N(180° - 360°)} \tag{7.18}$$

Where: $N(180°; 0°)$ = count rate at $\varphi = 180°$, and $\theta = 0°$

$\bar{N}(180° - 360°)$ = count rate averaged from $\varphi = 180°$ to $\varphi = 360°$ at $\theta = 0°$

$\bar{N}$ = count rate averaged over the entire azimuthal angle at $\theta = 0°$

$\bar{\bar{N}}$ = count rate averaged over the entire unit sphere

The above ratios characterize the effects of shielding and presented areas as a function of energy. The energies considered were 1.25 Mev, 0.66 Mev, and 60 kev. The ratios S_{14}, S_{24}, and S_{34} are not measured for 60 kev; however, by proper extrapolations, a self-consistent matrix system can be constructed as in Figure 7.2 with properties:

$$S_{ij} = 1 \tag{7.19}$$

$$S_{ij} = S_{ji}^{-1} \tag{7.20}$$

$$S_{ij} = S_{ik} \cdot S_{kj} \tag{7.21}$$

Thus, values obtained for S_{14} in the energy range 70 to 120 kev can be used to transform the given unidirectional count rates $N(180°;\ 0°)$ into omnidirectional count rates

$$\bar{\bar{A}}_{eff} = \frac{N(180°;\ 0°)}{I \cdot S_{14}} = \frac{N(180°;\ 0°)}{I} \cdot \frac{\bar{\bar{N}}}{N(180°;\ 0°)} \tag{7.22}$$

as listed below:

End point Energy, kev	70	80	90	100	110	120
S_{14}	0.285	0.300	0.320	0.330	0.343	0.353
$\bar{\bar{A}}_{eff}$, 10^{-2} mm^2	1.75	2.07	1.97	1.92	1.95	1.90

The averaged omnidirectional effective areas and the corresponding averaged peak energy is:

$A_{eff} = 1.9 \times 10^{-2}$ mm^2 for an average photon energy of

$$\bar{E} = 60 \text{ kev} \tag{7.23}$$

7.5 ENERGY DEPENDENCE OF EFFECTIVE AREAS, DETECTORS C AND D

The count rate ratio of the lead-shielded GM tube (Detector D) and the unshielded tube (Detector C) can be used to determine the energy corresponding to peak intensity of a given radiation in the form of dimensionless expression:

$$\frac{N_D(E)}{N_C(E)} = f(E) \tag{7.24}$$

This function $f(E)$ should be zero at the threshold energy of Detector D and should approach 1 for increasingly high energies. Therefore, it is reasonable to assume the exponential function,

$$f(E) = 1 - \exp -\{\mu(E - E_{thresh})\} \tag{7.25}$$

By the introduction of the known count rate ratios from the gamma calibration at the energies of 0.662 and 1.25 Mev, the following expression is obtained,

$$f(E) = 1 - \exp -1.273\,(E - 0.050 \text{ Mev}) \tag{7.26}$$

as a function that describes at least the interval from 0.66 to 1.25 Mev with sufficient accuracy. Because the derived threshold energy matches exactly the extrapolated value of Equation 5.2, it is possible to assume that f(E) is a good approximation at lower energies.

The comparison of the count rate ratios as obtained by the X-ray experiments verifies Equation 5.6. Consequently, it is possible to write the derivatives of Equation 5.6 in the vicinity of the threshold energy as

$$\frac{\partial}{\partial E} f(E) \equiv \frac{\partial}{\partial E}\left(\frac{N_D(E)}{N_C(E)}\right) > \frac{\partial}{\partial V}\left(\frac{N_D(V)}{N_C(V)}\right) \tag{7.27}$$

which is correct, because

$$\frac{\partial}{\partial E} f(E) = 1.273\ (\text{Mev})^{-1} \tag{7.28}$$

$$\frac{\partial}{\partial V}\left(\frac{N_D(V)}{N_C(V)}\right) = 0.45\ (\text{Mev})^{-1} \tag{7.29}$$

The linear exptrapolation of the count rate of Detector C versus end point energy in Figure 5.8 leads to the same threshold as for Detector D, namely, 50 kev. This leads to the conclusion that 50 kev is the absolute threshold for the Anton 302 GM tubes in the given environment, since Detector D is modified only by the additional attenuation function (Equation 7.25).

The effective area as a function of energy can be described by an exponential function similar to that in Equation 7.25

$$A_{eff} = A_0\left[1 - \exp - 1.37\ (E - 0.050 \text{ Mev})\right] \qquad \text{(Figure 7.3)} \tag{7.30}$$

where $$A_0 = 1.26 \text{ mm}^2 \tag{7.31}$$

A_0 is fictional and can be interpreted as the upper limit of the effective area for photons of extremely high energies.

By combination of Equation 7.24 and Equation 7.30, it is possible to derive the effective area of Detector D:

$$A_{eff_{(D)}} = A_{eff_{(C)}}\left[1 - \exp. - 1.273\ (E - 0.050 \text{ Mev})\right] \tag{7.32}$$

or in the vicinity of the threshold

$$\frac{A_{eff_D}}{A_0} = \text{const. } (E - 0.050 \text{ Mev})^2 \tag{7.33}$$

A parabolic increase of the count rates has indeed been measured at end point energies from 70 to 100 kev as shown in Figure 5.8.

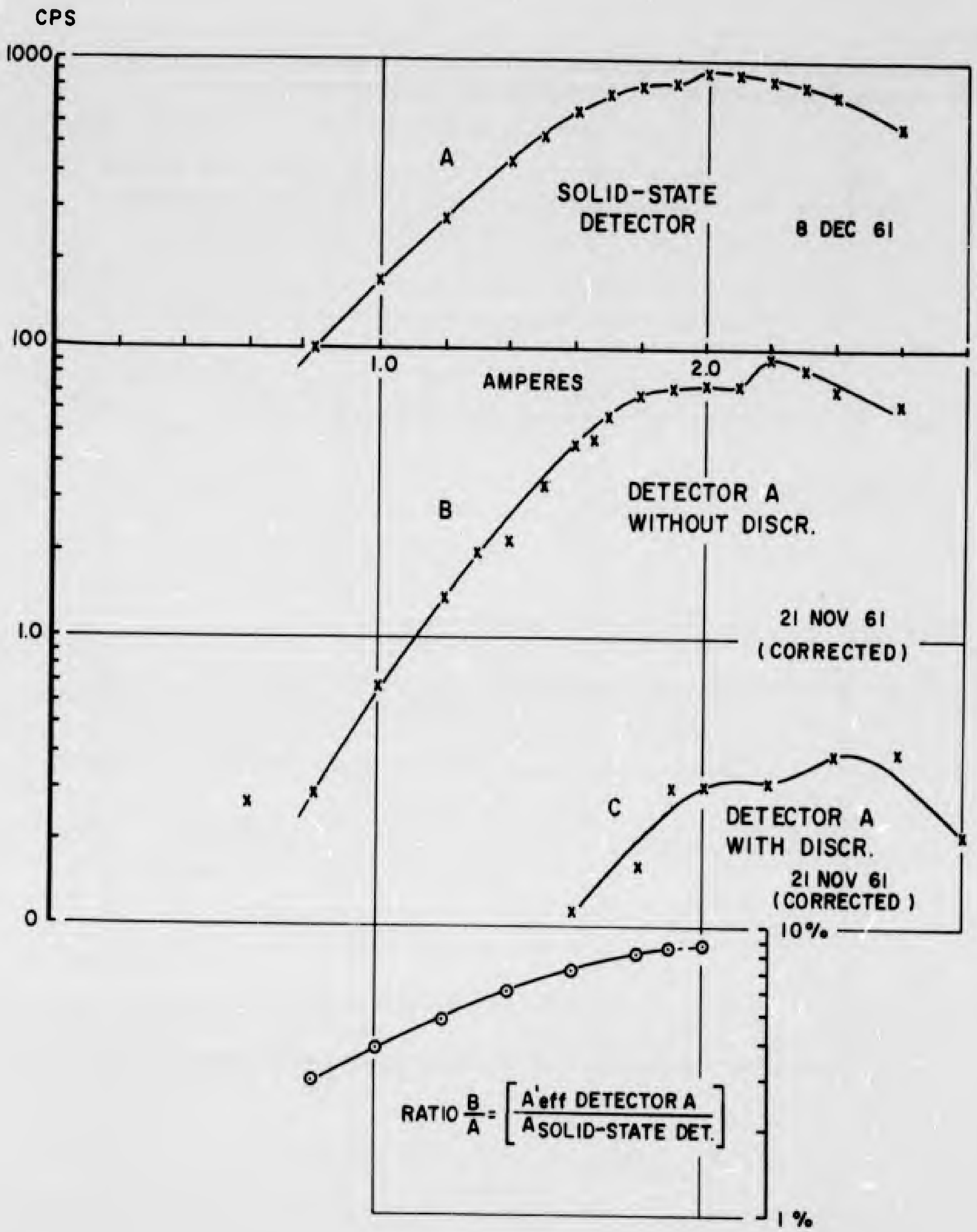

Figure 7.1 Determination of effective area of Detector A by comparison with the count rate of a highly sufficient solid-state detector with defined area.

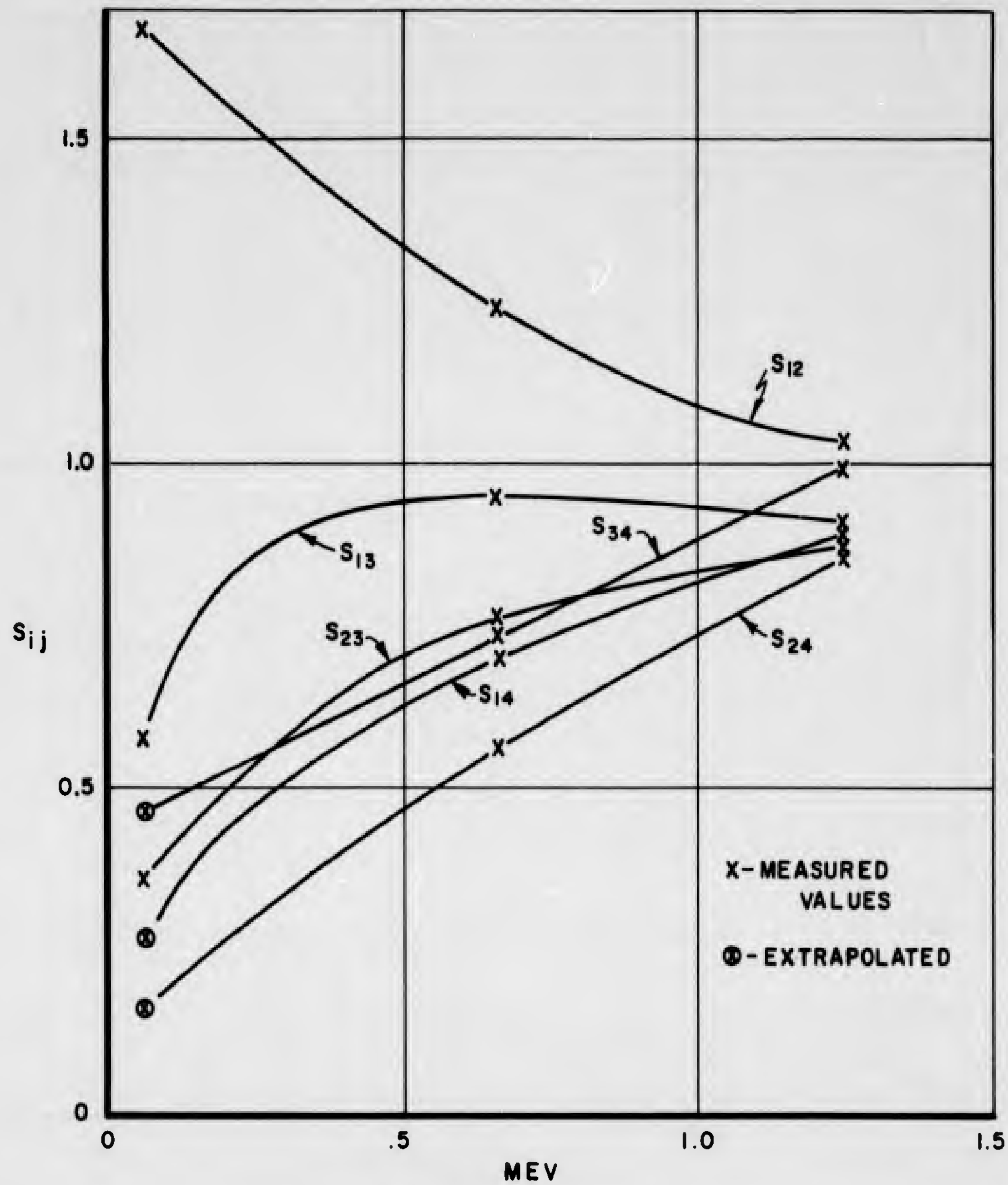

$S_{ij} = S_{ji}^{-1} = S_{ik} S_{kj} \quad S_{ij} = \frac{N_i(E)}{N_j(E)}$

Figure 7.2 Selected count-rate ratios on Detector C as elements of the matrix S_{ij} as a function of photon energy.

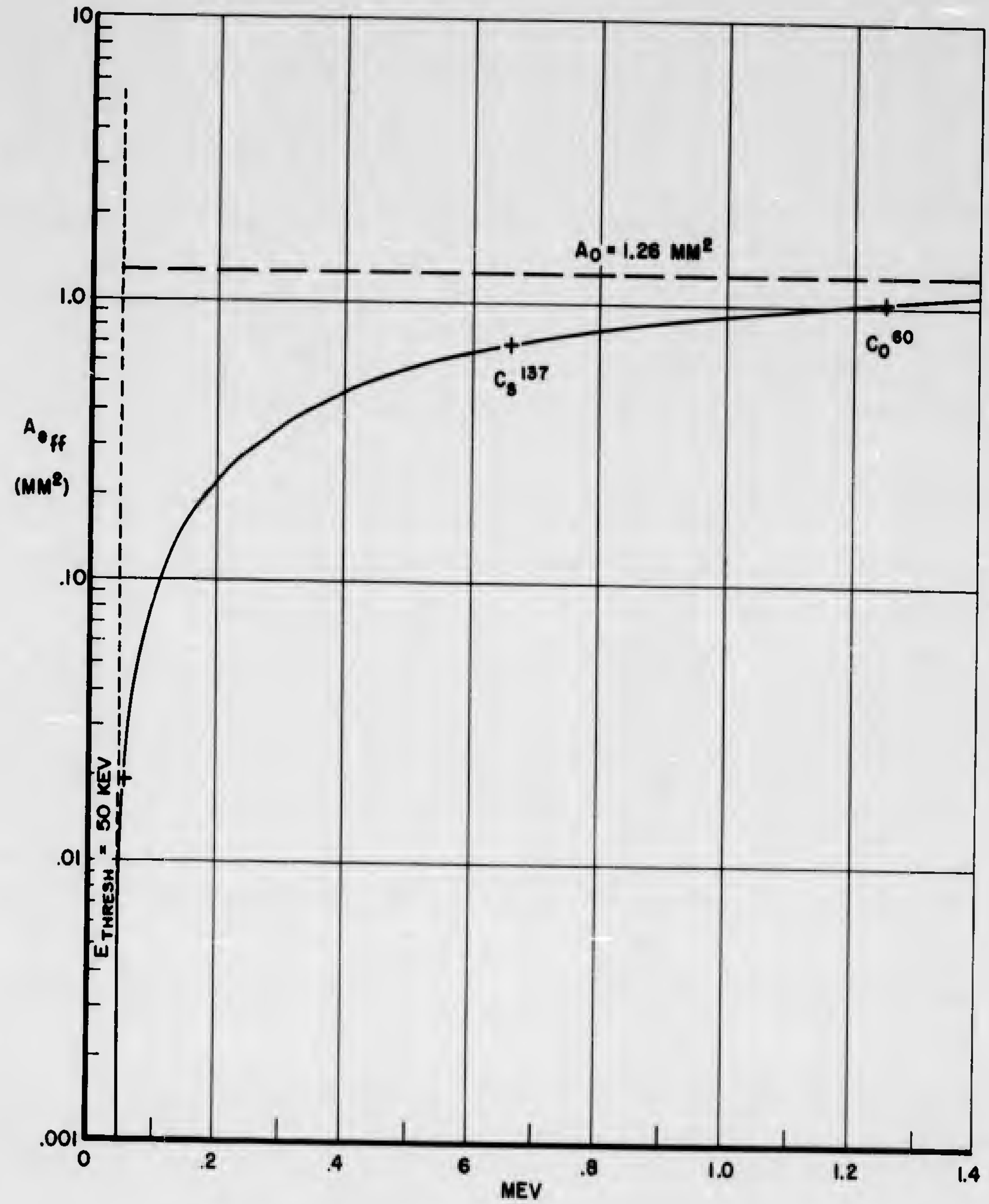

Figure 7.3 Effective area of Detector C (unshielded GM tube) as a function of photon energy.

CHAPTER 8

CONCLUSION

The detailed calibration curves presented in this report will be of varying importance to different groups analyzing the Explorer IV count rate data by various methods and for different purposes. However, for the purpose of determining the optimum procedure for systematic data analysis to extract the maximum amount of information from the Explorer IV count rate data, it has been anticipated that all of the inclosed calibration data will be necessary.

Much more derived information can be obtained from the calibration curves than has been indicated in Section 7.5. However, the decision as to which derived information is necessary and sufficient for a given purpose is best left to the judgment of the individual investigator.

REFERENCES

1. C. Lundquist; "Progress in Design and Implementation of Scientific Spacecraft"; Army Ballistic Missile Agency, Redstone Arsenal, Alabama.

2. R. J. Naumann; "Directional Dependence of Counting Rates from Explorer IV"; George C. Marshall Space Flight Center, Huntsville, Alabama.

3. K. Epstein; "An Examination of Various Procedures for Determination of Angular and Energy Distributions of Radiation From Explorer IV Count Rate Data"; Ballistic Research Laboratories, Aberdeen Proving Ground, Maryland.

4. Gersholm, Siegbahn; "Beta and Gamma Ray Spectroscopy"; 1955 Interscience Publ., Inc., New York

DISTRIBUTION

Military Distribution Categories 62

ARMY ACTIVITIES

1 CHIEF OF R & D DA
1 AC OF S INTELLIGENCE DA
1 CHIEF OF ENGINEERS DA
2 ARMY MATERIAL COMMAND
1 CHIEF SIGNAL OFFICER DA
2 U S ARMY COMBAT DEVELOPMENTS COMMAND
1 DIRECTOR OF SPECIAL WEAPONS DEVELOPMENT OFFICE
1 U S ARMY ARTILLERY BOARD
1 U S ARMY AIR DEFENSE BOARD
1 U S ARMY AVIATION BOARD
1 U S ARMY COMMAND AND GENERAL STAFF COLLEGE
1 U S ARMY AIR DEFENSE SCHOOL
1 U S ARMY ARMORED SCHOOL
1 U S ARMY ARTILLERY & MISSILE SCHOOL
1 U S ARMY AVIATION SCHOOL
1 U S ARMY INFANTRY SCHOOL
1 CHEMICAL CORPS TRAINING COMD
1 U S ARMY SIGNAL SCHOOL
1 ARMY MEDICAL RESEARCH LAB
1 DIAMOND ORDNANCE FUZE LABORATORY
1 BALLISTIC RESEARCH LABORATORY
3 U S ARMY MISSILE COMMAND
1 WHITE SANDS MISSILE RANGE
1 ORDNANCE AMMUNITION COMMAND
1 COMMUNICATIONS & ELECTRONICS COMMAND
1 U S ARMY ELECTRONIC PROVING GROUND
1 U S ARMY COMBAT SURVEILLANCE AGENCY
1 U S ARMY SIGNAL R&D LABORATORY
1 THE RESEARCH & ANALYSIS CORP
1 WHITE SANDS SIGNAL SUPPORT AGENCY
1 NUCLEAR DEFENSE LABORATORY
1 U S ARMY AIR DEFENSE COMBAT DEV AGENCY

NAVY ACTIVITIES

2 CHIEF OF NAVAL OPERATIONS OP03EG
1 CHIEF OF NAVAL OPERATIONS OP-09B5
1 CHIEF OF NAVAL OPERATIONS OP-75
1 CHIEF OF NAVAL OPERATIONS OP-922G1
2 CHIEF OF NAVAL RESEARCH
3 BUREAU OF NAVAL WEAPONS DLI-3
1 BUREAU OF SHIPS CODE 423
1 U S NAVAL RESEARCH LABORATORY
2 U S NAVAL ORDNANCE LABORATORY
1 NAVY ELECTRONICS LABORATORY
1 U S NAVAL MINE DEFENSE LAB
1 U S NAVAL RADIOLOGICAL DEFENSE LAB
1 U S NAVAL CIVIL ENGINEERING LAB
1 U S NAVAL SCHOOLS COMMAND TREASURE ISLAND
1 U S NAVAL POSTGRADUATE SCHOOL
1 AIR DEVELOPMENT SQUADRON 5 VX-5
1 US NAVAL AIR SP WPNS FACILITY
4 U S MARINE CORPS CODE A03H

AIR FORCE ACTIVITIES

1 HQ USAF AFTAC-TD
1 HQ USAF AFRDC-AE
1 HQ USAF AFRDR-NU
1 HQ USAF AFOAC
1 HQ USAF OPERATIONS ANALYSIS OFFICE
5 HQ USAF AFCIN-3D1
1 DC OF S RESEARCH & TECHNOLOGY
1 TACTICAL AIR COMMAND
1 AIR DEFENSE COMMAND
1 AIR FORCE SYSTEMS COMMAND
1 AIR FORCE BALLISTIC SYSTEMS DIVISION
1 RADC-RAALD,GRIFFISS AFB
1 SECOND AIR FORCE
2 AF CAMBRIDGE RESEARCH CENTER
3 AFSWC KIRTLAND AFB NMEX
1 SCHOOL OF AVIATION MEDICINE
3 AERONAUTICAL SYSTEMS DIVISION
2 USAF PROJECT RAND
1 ELECTRONIC SYSTEMS DIV ESAT
1 BALLISTIC MISSILE EARLY WARNING PROJECT OFFICE
1 AIR TECHNICAL INTELLIGENCE CENTER
1 OFFICE OF AEROSPACE RESEARCH
1 HQ USAF AFORQ

OTHER DEPARTMENT OF DEFENSE ACTIVITIES

1 DIRECTOR OF DEFENSE RESEARCH AND ENGINEERING
1 ASST TO THE SECRETARY OF DEFENSE ATOMIC ENERGY
2 ADVANCE RESEARCH PROJECT AGENCY
1 WEAPONS SYSTEM EVALUATION GROUP
4 DEFENSE ATOMIC SUPPORT AGENCY
1 FIELD COMMAND DASA
1 FIELD COMMAND DASA FCTG
2 FIELD COMMAND DASA FCWT
2 DEFENSE INTELLIGENCE AGENCY
1 DEFENSE COMMUNICATIONS AGENCY
1 JOINT TASK FORCE-8
1 COMMANDER-IN-CHIEF EUCOM
1 COMMANDER-IN-CHIEF PACIFIC
1 COMMANDER-IN-CHIEF ATLANTIC FLEET
1 STRATEGIC AIR COMMAND
1 CINCONAD

ATOMIC ENERGY COMMISSION ACTIVITIES

3 AEC WASHINGTON TECH LIBRARY
2 LOS ALAMOS SCIENTIFIC LAB
5 SANDIA CORPORATION
10 LAWRENCE RADIATION LAB LIVERMORE
4 NEVADA OPERATIONS OFFICE,LAS VEGAS
1 DTIE OAK RIDGE,MASTER
30 DTIE OAK RIDGE SURPLUS

SPECIAL DISTRIBUTION

1 Military Liaison Committee
ATTN: Executive Secretary

1 Commander, Field Command, DASA

2 Commander, Field Command, DASA
ATTN: FCWT

1 JCS
ATTN: Executive Secretary

20 National Security Agency
ATTN: REMP

10 Chief, Defense Atomic Support Agency

Hq. U.S. Army Security Agency
1 Chief of Staff, G-4
1 Chief of Staff, G-3

1 U.S. Army Security Agency Technical Consultants

1 U.S. Army Security Agency Board
ATTN: Lt. Colonel Philip Finney

1 U.S. Army Security Agency Board
ATTN: Mr. William Moran

5 Army Security Agency Training Center

20 Chief of Research and Development U.S. Army
ATTN: Atomic Division

2 Hq. US Army Communications Agency
ATTN: SIGCA, Maj. K. W. Thomas

Chief of Naval Operations, D/N
1 ATTN: OP-03EG
1 ATTN: OP-30
1 ATTN: OP-36
1 ATTN: OP-91
1 ATTN: OP-922G2

1 Chief of Naval Research, D/N
ATTN: Code 811

1 Chief, Bureau of Naval Weapons

1 Chief of Naval Operations, D/N
ATTN: OP-922G1

1 Commander, U.S. Naval Ordnance Laboratory

1 Commanding Officer and Director
Naval Electronics Laboratory

1 U.S. Naval Radiological Defense Laboratory
ATTN: Technical Information Division

1 Commander
U.S. Naval Ordnance Test Station

1 Commandant
U.S. Coast Guard
ATTN: (OIN)

1 Chief, Bureau of Ships
ATTN: Code 810a

1 U.S. Naval Research Laboratory
Madison, Wisc., ATTN: J. O. Hirschfelder

1 Commander
U.S. Naval Ordnance Test Station
ATTN: Elmer T. Canavin

1 U.S. Naval Missile Test Center
ATTN: Harold Berman

U.S. Air Force Security Service
1 ATTN: ODC
1 ATTN: EDC
1 ATTN: 6900th Security Wing
1 ATTN: 6920th Security Wing
1 ATTN: 6981st Security Wing RGM
1 ATTN: 6901st Security Wing SCG
1 ATTN: 6902nd Security Wing SCG

10 Commander
Air Research and Development Command
ATTN: RDRW

1 Air Force Cambridge Research Center
ATTN: CRQST-2

1 Assistant for Atomic Energy
Hq., USAF

1 Office for Atomic Energy, DSC/O
ATTN: AFOAT-1

1 Director of Communications-Electronics
Hq. USAF

1 Deputy Chief of Staff, Development
Hq., USAF
ATTN: AFDAP

1 Deputy Chief of Staff, Operations
Hq. USAF
ATTN: Operations Analysis

Commander, U.S. Air Force Security Service
2 ATTN: SCE
2 ATTN: SCP
2 ATTN: SCT

2 Commander, Air Force Special Weapons Center
ATTN: SWOI

6 Commander, Wright Air Development Division
ATTN: WCLF, I. H. Bowker

4 Director of Research and Development
DCS/D, Hq., USAF
ATTN: AFDRD-GW

1 Commander, Air Force Office of Scientific Research
ATTN: SRKA, Lt. Connelly

Assistant Chief of Staff, Intelligence
1 ATTN: AFCIN-1B2
1 ATTN: AFCIN-3B2
1 ATTN: AFCIN-1C, Lt. Col. Kellan

2 Director, National Aeronautics and Space Administration
ATTN: Bertram Mulcahey

1 Director, Central Intelligence Agency

1 Massachusetts Institute of Technology
Lincoln Laboratory
ATTN: James H. Pannell

1 E. O. Baicy
Ballistic Research Laboratories
Aberdeen Proving Ground

1 Timothy F. Bell
Stanford Radioscience Laboratory

1 Robert L. Bollen
Stanford Research Institute

1 Hans A. Bomke
U.S. Army Signal Research and Development Laboratory

1 H. F. Busch
ACF Industries, Inc.

1 Jack W. Carpenter
American Science & Engineering, Inc.

1 E. Chernosky
Air Force Cambridge Research Laboratories

1 Lt. Comdr. D. E. Chandler
Advanced Research Projects Agency

1 Nicholas C. Christofilos
Lawrence Radiation Laboratory

1 John B. Cladis
Lockheed Missile & Space Division

1 Cullen Crain
The RAND Corporation

1 Rolf B. Dyce
Stanford Research Institute

1 Arthur K. Harris
U.S. Army Signal Research and Development Laboratory

1 Capt. R. C. Hawlk
Army Ballistic Missile Agency

1 R. A. Helliwell
Stanford Radioscience Laboratory

1 R. Hendrick
General Electric Company
TEMPO Division

1 George L. Johnson
Stanford Research Institute

1 John P. Katsufrakis
Stanford Radioscience Laboratory

1 Richard Kaufmann
Armed Forces Special Weapons Center

1 Rolf K. M. Landshoff
Lockheed Missile & Space Division

1 Robert E. LeLevier
The RAND Corporation

1 Charles Lundquist
Marshall Space Flight Center

1 Thomas P. Markham
Air Force Cambridge Research Laboratories

1 Roland E. Meyerott
Lockheed Missile & Space Division

1 Maj. John E. Mock
Defense Atomic Support Agency

1 Wesley Mollard
ACF Industries, Inc.

1 Philip Newman
Air Force Cambridge Research Labs

1 Robert Naumann
National Aeronautics and Space Administration

1 Major F. Zengel
Air Force Technical Applications Center

1 Maj. Ralph Pennington
DDRE

1 A. M. Peterson
Stanford Research Institute

1 H. Reno
Denver Research Institute

1 Paul Tamarkin
The RAND Corporation

1 George Taylor
Lockheed Missile & Space Division

1 E. H. Vestine
The RAND Corporation

1 M. Walt
Lockheed Missile & Space Division

1 K. Watson
Princeton University

1 A. H. Weber
St. Louis University

1 Capt. J. Welch
Armed Forces Special Weapons Center

1 Dep Chief of Staff for Mil Ops
ATTN: Dir of SW&R

1 Assistant Chief of Staff,
Intelligence, DA

1 Chief of Engineers, DA
ATTN: ENGNB

1 Chief of Ordnance, DA
ATTN: ORDTN

1 Chief Signal Officer, DA,
ATTN: SIGCO-4

1 Commander-in-Chief, U.S. Army Europe,
ATTN: OPOT Div, Weapons Br.

3 U.S. Continental Army Command

1 Director of Special Weapons Development Office
Hq CONARC

1 President
U.S. Army Artillery Board

1 President
U. S. Army Air Defense Board

1 Chief of Engineers, DA
ATTN: ENGTB

1 President
U.S. Army Aviation Board
ATTN: ATBG-DG

1 U.S. Army C&GS College
ATTN: Archives

1 U.S. Army Air Defense School
ATTN: Dept of Tactics & Combined Arms

1 U.S. Army Armored School

1 U.S. Army Arty & Missile School
ATTN: Combat Dev Dept

1 U.S. Army Aviation School

1 U.S. Army Infantry School
ATTN: C.D.S.

1 Chemical Corps Training Comd

1 US Army Signal School

1 US Army Chemical Corps
Research & Development Comd

1 Chemical Warfare Lab
ATTN: Tech Library

1 Diamond Ordnance Fuze Lab
ATTN: Ch, Nuclear Vulnerability Branch (230)

1 Aberdeen Proving Ground
ATTN: Ballistic Research Lab, Dir, BRL

1 U.S. Army Ord. Missile Comd

1 Army Rocket & Guided Missile Agency
ATTN: Technical Library

1 White Sands Proving Ground
ATTN: ORDBS-OM

1 Army Ballistics Missile Agency
ATTN: ORDAB-HT

1 Ordnance Ammunition Comd

1 US Army Electronic Proving Ground
ATTN: Tech Library

1 US Army Combat Surveillance Agency

2 US Army Signal R&D Laboratory
ATTN: Tech Doc Ctr, Evans Area

1 Operations Research Office

1 Chief of Naval Operations
ATTN: OP-75

1 Chief, Bureau of Ships
ATTN: Code 423

2 U.S. Naval Research Laboratory
ATTN: Mrs. Katherine H. Cass

1 U.S. Naval Mine Defense Lab

1 U.S. Naval Schools Command

1 U.S. Naval Postgraduate School

1 U.S. Naval CIC School

5 U.S. Marine Corps
ATTN: Code AO3H

1 Assistant for Atomic Energy
Hq, USAF
ATTN: DCS/O

1 Director of Research & Development
DCS/D, Hq USAF
ATTN: Guidance & Weapons Division

1 Tactical Air Command
ATTN: Doc Security Branch

2 Air Defense Command
ATTN: Atomic Energy Division ADLAN-A

2 Air Force Ballistic Missile Division
ATTN: WDSOT

1 1009th Sp Wpns Squadron

1 Air Defense Systems Integration Division
ATTN: SIDE-S

11 Ballistic Missile Early Warning Project Office
ATTN: Colonel Leo V. Skinner, USAF

1 Air Technical Intelligence Center
ATTN: AFCIN-4Bla, Library

2 Director of Defense Research and Engineering
ATTN: Tech Library

2 Weapons Systems Evaluation Group

1 Office of the United States National Military Representative
SHAPE

2 Strategic Air Command
ATTN: OAWS

5 Advanced Research Projects Agency

1 Hans Mark
Lawrence Radiation Laboratory

UNCLASSIFIED

UNCLASSIFIED